In Search of Ferroelectricity in Antiferroelectric Lead Zirconate

PAR

Kaushik VAIDEESWARAN

EPFL

ÉCOLE POLYTECHNIQUE
FÉDÉRALE DE LAUSANNE

Suisse
2015

Acknowledgements

Firstly, I thank my thesis directors, Prof. Nava Setter and Prof. Alexander K. Tagantsev, for providing me with an opportunity to work in such a multifaceted project, and for their unending technical and pedagogical support through the entire period. Nava, that you placed your confidence in me and conferred on me this project, is something I will always cherish. Sacha, your passion for teaching, your persistence in helping me understand everything that I found complicated, and your way of converting physics into an art is something that I will carry with me for a long time. The number of things I have learnt from both of you, at work and otherwise, has made me wiser.

I would like to thank Prof. Sergey Vakhrushev, Dr. Roman Burkovsky, Dr. Anton Shaganov, Dr. Alexei Filiminov, Dr. Alfred Baron, Dr. Hiroshi Uchiyama, Dr. Dmitry Chernishov, Dr. Alexei Bosak, Prof. Chunlin Jia, Dr. Xian-kui Wei, Dr. Cosmin Sandu, Dr. Alexander Duncan, Prof. Joe Troedahl and Dr. Brahim Dkhil for their collaborative support through all stages of the project. Without your contributions, the project would not be where it currently stands.

I wish to express my gratitude to the members of my thesis examination committee, Prof. Francesco Stellacci, Prof. Krystian Roleder, Prof. Anna Fontcuberta-i-Morral and Dr. Celine Lichtensteiger for their careful scrutiny and for their invaluable feedback. I am also grateful to Prof. Dragan Damjanovic and Prof. Paul Muralt for all the discussions on science, on politics, on history and on multiple other subjects, which have given me a broader perspective of things. I thank as well Prof. B.S. Murty, who was instrumental in igniting in me the sense of scientific curiosity, who taught me to question things, and that the simplest of questions yield the most beautiful answers.

The past four years have been for me an adventure. Like all adventures, it has had its highs and lows. Through all these variations, my colleagues in the ceramics laboratory have been by my side. Nachi, thanks for always being there for me on my best and on my worst days, and for helping me without the slightest hesitation whenever I needed it. I was once told at the very beginning that I would be in the best office of the lab, and I am convinced that this was the case. Monika, Ludwig, Scott and Evgeny, thanks for sharing your space with me and for everything you have done for me. The last four years would have been extremely boring had it

Acknowledgements

सर्वस्य लोचनं शास्त्रं |

Perception is the basis of knowledge
—hitopadeśa 10

Abstract

Since the prediction of antiferroelectricity and the subsequent discovery of $PbZrO_3$, the description of antiferroelectric behaviour in materials has been constantly modified to account for the latest properties identified in antiferroelectric materials. Adding to this refinement, the current study considers Lead Zirconate ($PbZrO_3$) as a prototypical antiferroelectric and through it, aims to understand the origin of antiferroelectricity, and the possibility of localised ferroelectric behaviour inside the material. The observation and control of the occurence of such localised ferroelectricity is attempted and the mechanical behaviour of such ferroelectric structures is simulated.

Antiferroelectrics are defined as materials which undergo a phase transition from one centrosymmetric phase to another while being accompanied by a dielectric anomaly at the transition. The origin of antiferroelectricity as observed in the prototypical antiferroelectric $PbZrO_3$, involves multiple lattice instabilities with interactions that remained only partially deciphered. The current study provides for an explanation of the lattice dynamics occuring in $PbZrO_3$ through results obtained from a combination of scattering techniques such as Inelastic X-Ray, Thermal Diffused and Brillouin scattering. The primary structural instability associated with the antiparallel lead displacements is seen to be coupled with the ferroelectric order parameter, and to the order parameter related to the oxygen octahedral rotations. On the appearance of the structural order parameter, these interactions result in the formation of the antiferroelectric phase of $PbZrO_3$ as known previously. The premises for such interactions and their validations are provided, while explaining all aspects associated with the antiferroelectric phase transition occuring in $PbZrO_3$ including the dielectric anomaly.

One significance of the scenario with competing order parameters lies in the possible appearance of the subdued order parameters in regions where the primary order parameter is absent. The conditions for the disappearance of this order parameter in the case of $PbZrO_3$ is discussed, and structural domain boundaries are shown to be potential regions for the

local observation of otherwise subdued ferroelectricity. Aimed at the observation of localised ferroelectric structures in an otherwise antiferroelectric material, growth of epitaxial thin films of $PbZrO_3$ is undertaken using Pulsed Laser Deposition. The growth parameters are varied to control the crystalline orientation and the defect concentration in the films through the control of the interfacial strain. In this process, a technique for the tunable variation of the epitaxial strain using a single composition buffer layer has been documented.

The antiferroelectric films are then utilised for the observation of regions of disrupted symmetry, for the observation of localised ferroelectricity. The distribution of such regions in the thin films, as well as the anomalous interaction of different types of domain walls with crystalline defects are observed and analysed. Alongside, the response of such localised ferroelectric structures to external electric fields is simulated. The conditions necessary for sufficiently large displacements of such structures, large enough for potential observation using Scanning Probe Microscopy techniques, have been listed.

Keywords : Antiferroelectricity , PZO, $PbZrO_3$, Inelastic Scattering, PLD, epitaxial thin film, buffer layer, misfit stress control, APB, local ferroelectricity.

Résumé

Depuis la prédiction du phenomène d'antiferroélectricité, suivie par la découverte du premier antiferroélectrique $PbZrO_3$, la définition de l'antiferroélectricité évolue constamment pour y inclure les nouvelles propriétés découvertes. Contribuant à cette évolution, cette étude porte sur le matériau antiferroélectrique modèle $PbZrO_3$ afin de comprendre l'origine de l'antiferro-électricité et la possibilité de l'apparition locale de propriétés férroélectriques. L'observation et le contrôle de l'apparition de cette ferroélectricité locale sont éprouvés et les propriétés des structures simulées.

Les antiferroélectriques sont définis comme étant des matériaux ayant une transition de phase entre deux phases centrosymmétriques avec une anomalie de la constante diélectrique à la température de transition. L'origine de l'antiferroélectricité telle qu'observée dans $PbZrO_3$ consiste en des interactions entre plusieurs instabilités dans la maille qui ne sont que partiellement expliquées. Avec les observations obtenues à partir des techniques telles que la dispersion inélastique de rayons x, la dispersion thérmique des rayons x ainsi que la dispersion brillouin, cette étude met en place une explication de la dynamique de maille dans $PbZrO_3$ à la transition de phase. L'instabilité primaire est associée aux déplacements dans les directions antiparallèles des atomes de Pb et est couplée au paramètre d'ordre responsable de l'apparition de la ferroélectricité, ainsi que celui associé aux rotations des octahèdres d'oxygène. Lors de l'apparition de ce paramètre d'ordre structurel, ces interactions conduisent à la formation de la phase antiferroélectrique telle qu'elle est connue. Les conditions pour que les interactions aient lieu et leurs validations pour ce materiau sont démontrées et sont également utilisées pour expliquer les autres traits associés avec la transition de phase dans $PbZrO_3$, y compris l'apparition de l'anomalie diélectrique.

La compétition entre les différentes instabilités dans le système est liée à l'apparition de paramètres d'ordre, autrement atténués par la présence du paramètre d'ordre principal, aux endroit où le paramètre d'ordre principal est absent. Les conditions de la disparition du para-

mètre d'ordre principal sont dévélopées et la présence des parois de domaine structurelles est attribuée à la possibilité de maintenir les propriétés ferroélectriques locales. Afin d'observer la ferroélectricité locale dans un materiau autrement antiferroélectrique, des couches minces de PbZrO$_3$ sont fabriquées par ablation laser pulsé. Les paramètres de croissance ont été optimisés pour contrôler l'orientation cristalline et la concentration de défauts cristallins dans les couches en contrôlant la contrainte à l'interface.

Des couches antiferroélectriques ont été utilisées pour observer des régions ayant une symmétrie locale perturbée, afin d'étudier leur ferroélectricité locale. La distribution de ces structures ainsi que leurs interactions avec les défauts cristallins ont également été étudiées. Les réponses mécaniques des structures ferroélectriques en fonction de la présence d'un champ électrique externe ont été simulées. Les conditions nécessaires ont été déterminées pour déplacer ces structures. Elles sont suffisamment larges pour être observées par des techniques de microscopie à sonde locale.

Mots-clés : Antiferroélectricité , PZO, PbZrO$_3$, Diffusion inélastique, PLD, couche mince épitaxiée, couche tampon, contrôle du désaccord local, APB, ferroélectricité locale.

Contents

Contents

1 Introduction

The field of ferroics, though dating back to a century, continues to expand in a way such that the frontiers are regularly redefined, and new functionalities are still discovered, contributing directly to fulfilling scientific curiosity, and allowing for the continous improvement in existing technologies and for the imagination (and realisation) of newer technologies. The advances in this field were encouraged not only by work aimed directly at ferroics, but also through the increasing knowledge developed in other parallel arenas. The improvement in vacuum technology is one such example. While the effect of miniaturisation in ferroics was being studied through ferroic thin films, the quality of the thin films was initially restricted by the quality of the vacuum attainable during the deposition process, directly affecting the structure and hence, the properties of the thin films. With the improvements achieved in the vacuum technologies, it was possible to obtain a better control over the deposition conditions of the thin films, thus allowing for a better control over the structural quality and the properties of the thin films. Presently, thanks to the leaps in vacuum technology, atomic level control can be achieved in the fabrication of thin films, allowing for more detailed tailoring of the films in pursuit of the properties desired, leading to applications including nonvolatile Ferroelectric Random Access Memory (FeRAM) [1], microdevices for microactuators [2], acoustic sensors[3] and transducers[4], and high frequency electrical components[5] among many others [6].

The evolution of antiferroelectrics is similar, dating back to the 1950s, when it was first predicted by Kittel [7]. The predictions, made on a completely theoretical basis, did not reveal any method for identifying antiferroelectric materials. Subsequently, with the discovery of $PbZrO_3$ in the very same year [8], a slightly clearer idea of what entails an antiferroelectric was constructed. Thereafter, through multiple trials at understanding the structure and the dielectric responses, typical observed traits of antiferroelectrics were enumerated: the antiparallel

displacement of ions, a dielectric anomaly at the phase transition temperature, and double hysteresis in polarisation-field loops.

Using the above as guidelines for the description of antiferroelectrics, the discussion was taken beyond lead based ferroic perovskites to include some non-lead based perovskites like NaNbO$_3$ [9], and later to liquid crystals [10–12], hydrogen bounded systems like NH$_4$H$_2$PO$_4$ [13], even ice [14]. Among these, the liquid crystals gathered a lot of attention owing to their potential applicability in display systems [15], though little knowledge of the structure and its control was available. Eventually the arrival of better technology, and owing to the difficulties in understanding better the physics behind the ferroic states in liquid crystals [16], led to diminishing interest in organic antiferroelectrics, bringing the perovskites back in the spotlight.

By coupling of antiferroelectric perovskites (such as PbZrO$_3$ and NaNbO$_3$) with other ferroics like ferroelectrics (such as PbTiO$_3$ and KNbO$_3$), new phenomena such as the existence of a morphotropic phase boundary with giant electromechanical effects was observed in compositions such as the well-known Pb(Zr$_x$Ti$_{(1-x)}$)O$_3$[17] and K$_{1-x}$Na$_x$NbO$_3$ [18]. Antiferroelectrics in themselves gained interest through their giant electrocalorific effect [19] and giant electrostrictive effect [20]. Consequently, potential applications were proposed in micropumps [21], high charge storage capacitators [22], and even cardiac defibrillators [23]. Amidst all these discoveries pertaining to the properties, studies directed at the understanding of the origin of antiferroelectricity were undertaken simultaneously, though a complete picture was never obtained owing to the rather complex lattice dynamics of antiferroelectric materials, thus restricting the possibility of engineering the properties towards newer applications.

1.1 Motivation

The current study aims at a better understanding of the antiferroelectric materials through the consideration of PbZrO$_3$ as a prototypical antiferroelectric, by a detailed comprehension of the lattice dynamics above and below the phase transition. This insight will allow for the determination of the conditions under which the multiferroic behaviour of the antiferroelectric materials might be altered, thus allowing potentially for development of scenarios wherein the behaviour might be locally tailored for specific applications.

The understanding of the origin of antiferroelectricity, could yield the conditions under which one could imagine the introduction of a ferroelectric entity within the antiferroelectric matrix through a local modification of the lattice dynamics. Such local structures could serve as

potential entities for applications such as memory storage. If one is able to control the size of these entities to be smaller than conventional ferroelectric domains used in ferroelectric memories, it would aid in reducing the size of the elementary bit, thereby resulting in increased information density per unit volume and further, in the miniaturisation of memory devices. Besides, a clearer insight into the lattice dynamics in an antiferroelectric such as $PbZrO_3$, that is conditioned by a complex interplay of atomic interactions through the lattice modes, could potentially serve as a framework for the explanation of similar phenomena seen in other multiferroic systems such as modified $BiFeO_3$.

Alongside the theoretical knowledge of the system, the current study also includes the growth of thin films of $PbZrO_3$, aimed at analysing the effect of external parameters such as strain and electric field on the antiferroelectric nature of $PbZrO_3$, with explanations derived from the scenario for the origin of antiferroelectricity. At the same time, metastable growth conditions in thin films could increase the chances of local disruptions of order parameters, potentially useful in the search of structures containing the predicted local ferroelectric behaviour in $PbZrO_3$.

1.2 Outline of the thesis

After the section on the state of the art (Chapter 2) summarising the current understanding of antiferroelectrics, and a brief description of the experimental techniques used in this study (Chapter 3), the results obtained from the theoretical, experimental and numerical analyses carried out in the current study are presented.

Chapter 4 elucidates the lattice dynamics of $PbZrO_3$ across the phase transition as studied through various scattering techniques. This chapter provides a scenario for the explanation of the phase transition in $PbZrO_3$, using the interactions between the various instabilities in the system. Through the model created to describe the phase transition, an explanation for the traits commonly associated with antiferroelectrics are provided as well.

Chapter 5 presents the results pertaining to the growth of thin films of $PbZrO_3$ under different conditions of interfacial strain. The effect of the interfacial strain on the structural quality of the thin films is studied. Consequently, through the modulation of interfacial strain the control of the domain orientation as well as the defect concentration in the thin films is presented.

Chapter 6 analyses the dielectric properties associated with the thin films discussed in Chapter 5. The observation of typical antiferroelectric behaviour through the dielectric responses of

the film with external fields is presented, and the effect of the defects arising from the epitaxial strain relaxation towards these dielectric responses is discussed. The range of temperature for the stablity of the antiferroelectric behaviour in the thin films is estimated as well.

From a local disruption of the lattice symmetry, the antiferroelectric properties in local regions are perturbed, resulting in the appearance of a localised polarity. In Chapter 7, the prediction for the appearance for such local polarity is discussed, followed by the observation of the same in the thin films of $PbZrO_3$. The interaction of these strutures with the defects in the thin films is observed and discussed, and estimates of the density of these structures is provided.

Finally, in Chapter 8, the interaction with an external electric field of such structures with localised ferroelectricity (as shown in Chapter 7) is analysed. The necessary conditions for the displacement of the wall, as well as estimates of the displacement achievable from such interactions are shown. The dependance of these displacements with experimental parameters is studied as well.

Thus, a deeper understanding of the behaviour of $PbZrO_3$ as a prototypical antiferroelectric is obtained as summarised in the concluding chapter (Chapter 9).

2 State of the Art

Despite the long time that has passed since the prediction and the subsequent discovery of antiferroelectric materials, the understanding of the origin of antiferroelectricity is still incomplete; perhaps owing to its far more complex nature when compared to ferroelectrics. The phenomenological models, though explaining the observed properties, shed little light on the origin itself. Recent advances in the understanding of the lattice physics associated with antiferroelectrics provide for possible explanation of antiferroelectricity, as well as novel potential means of exploitation of these materials. In this chapter, a brief review of the existing studies on antiferroelectrics is given, with particular emphasis on $PbZrO_3$ as a prototypical antiferroelecric material.

2.1   Ferroelectrics and Antiferroelectrics

In materials undergoing ferroic transitions, the lattice structure of the material changes from a high symmetry phase at high temperatures to a lower symmetry phase at low temperatures, when passing through a specific ferroic transition temperature. Certain materials with a lattice constructed by ions, on undergoing a phase transition pass from a non-polar structure to a polar structure. Such a system can be defined as a ferroelectric if in the polar phase in the absence of an external electric field, the vector corresponding to the derivative of the polarisation ($\mathbf{P}_i$) with respect to temperature, called the pyroelectric coefficient ($\mathbf{p}_i$, see Eq. 2.1), *"attains new components which were zero, by symmetry, in the high symmetry phase"* [24].

$$p_i \quad = \quad \left(\frac{\partial P_i}{\partial T} \right)_{E=0} \tag{2.1}$$
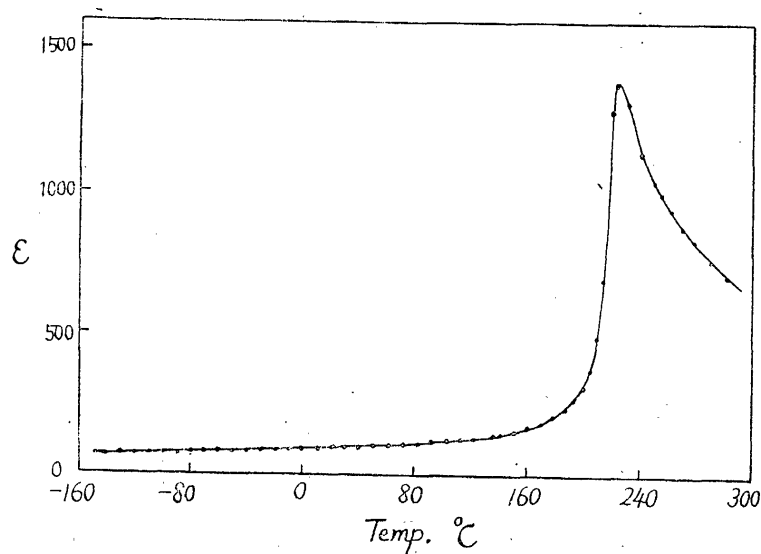
Figure 2.1: Dielectric constant of $PbZrO_3$ as a function of temperature showing a dielectric anomaly at the curie temperature [8] contradictory to Kittel's theory [7] which predicted no such behaviour.

In addition to the presence of a non-zero pyroelectric vector in the low symmetry phase, ferroelectric materials are also characterised by the possibility of changing the direction of the vector $\mathbf{p}_i$ through the application of an external mechanical stress or electrical field. This ability to "switch" the orientation of the polarisation through the reorientation of the pyroelectric vector is used in the form of Ferroelectric Random Access Memories (FeRAMs) [25], but meanwhile the gamut of current applications involving the use of ferroelectrics has diverged substantially to include ultrasonic devices, damping systems and fuel injection valves among others. The novel innovations possible through the use of thin films of ferroelectrics was summarised by Scott [26].

Antiferroelectrics, on the other hand, were first defined by Kittel [7], predicted to have lines of ions with a spontaneous polarisation but with neighbouring lines having the polarisation arranged in an antiparallel fashion. Starting from this definition and employing phenomenological theory to predict other properties, it was supposed that the material would exhibit no piezoelectricity owing to the presence of a center of symmetry and would not have an enhanced permittivity at the phase transition. The very same year, $PbZrO_3$ was observed to be an antiferroelectric, though with a dielectric constant comparable to that of $BaTiO_3$ at its transition temperature [8] (see Fig. 2.1), thus arousing curiosity towards antiferroelectrics. Currently, one can define antiferroelectrics as materials that undergo a phase transition from one centrosymmetric phase to another accompanied by a dielectric anomaly at the temperature of the phase transition.

6

2.1.1 Lead Zirconate

Lead Zirconate (PbZrO$_3$) undergoes a phase transition from a cubic paraelectric phase to an orthorhombic antiferroelectric phase at around 510K [8, 27]. The lattice parameters of the orthorhombic unit cell in terms of the cubic lattice parameter 'a' was shown to be $\sqrt{2}$a, $2\sqrt{2}$a and 2a along the a$_o$, b$_o$ and c$_o$ axes of the orthorhombic cell respectively [28]. The orthorhombic lattice of PbZrO$_3$ as seen along the 'c$_o$' axis is shown in Fig. 2.2. The Pb ions are displaced along the 'a$_o$' axis of the orthorhombic unit cell by 0.2 Å in an antiparallel fashion. Through this alternation of the displacement of Pb ions within the unit cell, the net dipole moment exhibited by the material within the a-b plane is 0. Initial speculations of a possible dipole moment along the c-axis were proposed from an alternative symmetry assigned to the structure [29], the same was discarded after refined neutron diffraction asserted a non-polar c-axis in an orthorhombic Pbam structure [30]. Another aspect of the structure, namely the oxygen octahedral rotations was analysed meanwhile as well and the Glazer tilt system of a$^-$a$^-$c^0 was associated with orthorhombic phase [30, 31].

(a)   **(b)**
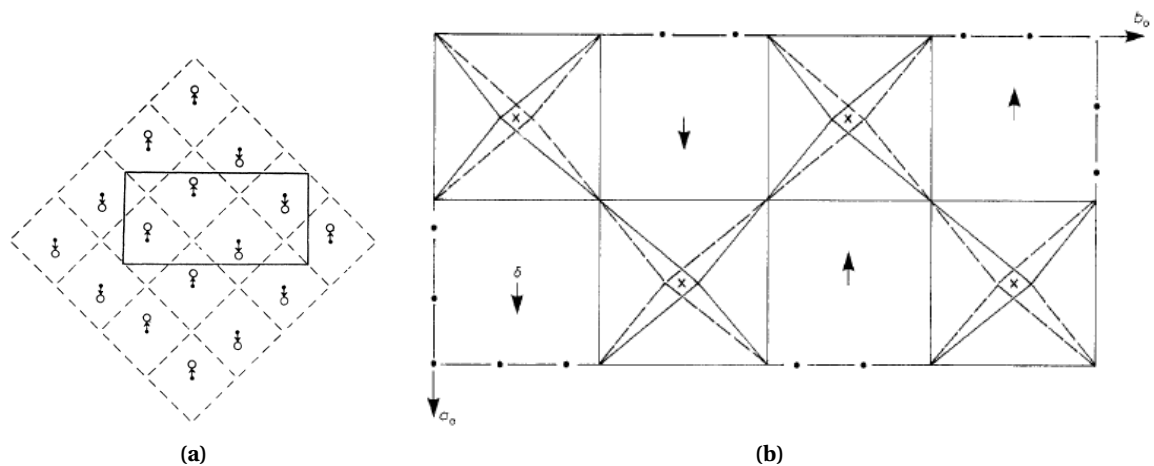
Figure 2.2: Construction of the PbZrO$_3$ unit cell. (a)Projection of the orthorhombic a-b plane on the cubic structure [28] . The dashed lines represent the cubic system while the solid lines show the orthorhombic unit cell (with the shorter of the two axes representing the 'a$_o$'). The arrows represent the shift of the Pb ions parallel to the a$_o$-axis. (b) Tilt of one layer of the ZrO$_6$ octahedra with the cation displacements (marked by δ) in one orthorhombic unit cell[32]. The corners of the squares as well as the junctions close to the 'x'(depicting the Zr ions) denotes the positions of the oxygen ions

The transition from the paraelectric cubic structure to the antiferroelectric orthorhombic structure, as mentioned before, occurs with a pronounced dielectric anomaly similar to a first order phase transition seen in ferroelectric materials like BaTiO$_3$, with the dielectric constant reaching several thousands, as shown in Fig. 2.1. This dielectric anomaly has been observed to obey the Curie-Weiss law at temperatures above the phase transition and to break down
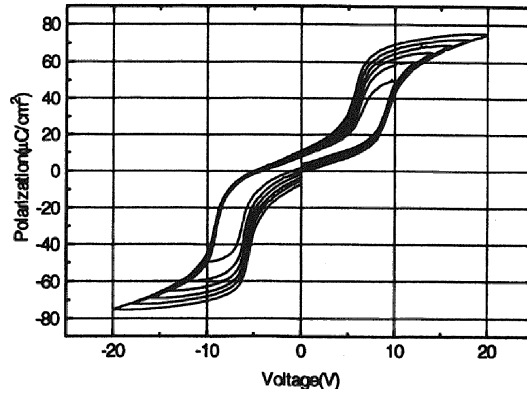
Figure 2.3: Double hysteresis loops observed in a $PbZrO_3$ thin film at room temperature with increasing field [44] proposing a field induced ferroelectric transition in the thin film.

immediately after the transition. In multiple studies there was also observed in between the cubic and the orthorhombic phases, a rhombohedral intermediate phase [33–35], having a stability only over a 10K temperature range, associated with a variation in the octahedral rotation [36] and predicted to be ferroelectric [37]. Though no valid consensus exists on the origin of this intermediate phase, it is mostly associated with stoichiometry and defects [38].

Another characteristic feature of the antiferroelectric materials, as has been observed in $PbZrO_3$, is the formation of double polarisation- field (P-E) hysteresis loops (see Fig. 2.3) [38, 39]. This was claimed to be as a result of a 'field-induced ferroelectric phase' into a rhombohedral structure with the free energy of the latter being only mildly higher than the former [40, 41]. Multiple trials towards the understanding of the low-symmetry polar structure of $PbZrO_3$ in high external fields have resulted in varied opinions, varying from a 90° in-plane rotation of all lead displacements to yield a polar structure[42], to an out-of-plane rotation of the lead displacement by 45° to yield a net polarisation along the c-axis [43]. So far, no consensus has been established on this subject, and the phenomenon of the "field-induced ferroelectric phase" remains unclear.

2.1.2 Lattice Instabilities in Lead Zirconate

There are three principle characteristic features of the orthorhombic unit cell in $PbZrO_3$ and these features can be associated with the instabilities of the phonon modes [45] at different points along the Brillouin zone owing to their symmetry (refer Fig. 2.4):

1. The anti-parallel displacement of the Pb ions along the [110] direction in the pseudocubic cell, leading to a four fold multiplication of the unit cell in the a-b plane. This defines the antiferroelectric character as per Kittel's definition [7], and is associated with an
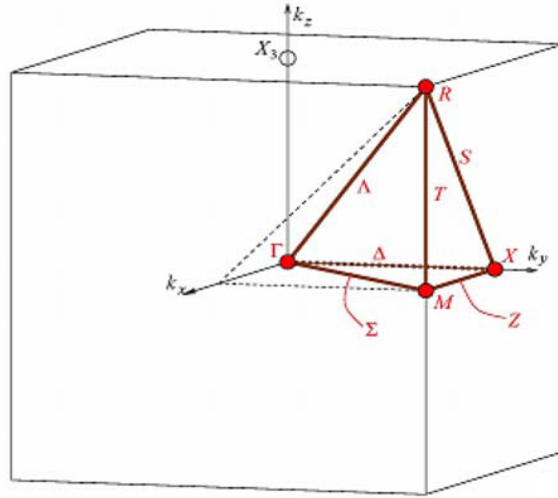
Figure 2.4: The first brillouin zone of the cubic PbZrO$_3$ crystal lattice. [49]

instability at the Σ or the $(\frac{1}{4}\frac{1}{4}0)$ point [31].

2. The opposite oxygen octahedral rotations in successive layers of the pseudocubic unit cell along the (001)-axis associated with an instability at the R or the $(\frac{1}{2}\frac{1}{2}\frac{1}{2})$ point [46, 47].

3. The dielectric anomaly observed during the phase transition, which has been associated previously with an instability at the zone center Γ or the (0 0 0) point [48].

For the complete understanding of the phase transition occuring in PbZrO$_3$, techniques such as neutron diffraction [30], infrared reflectivity [48], transmission measurements [50] and Raman studies [38] have been previously employed. Owing to the initial observation of polar regions in high zirconia content PbZr$_{(1-x)}$Ti$_x$O$_3$ samples [36] above the Curie temperature, the origin of the Curie-Weiss behaviour of the dielectric constant in PbZrO$_3$ above the curie temperature was associated with the presence of polar regions within the sample[38], but the appearance of the other features associated with the orthorhombic phase mentioned above remained unexplained.

The strong interaction between the Pb-ions and the neighbouring oxygen ions was established through neutron diffraction [51], and it was suggested that the distortion in the oxygen octahedral structure arose from the displacement of the lead atoms, potentially pointing towards the coupling of the two phenomena. This was also supported simultaneously through first principle calculations [52, 53] which associated the lead displacement not only with the ferroelectric soft mode seen at the zone center, but also with the antiferrodistortive feature of the phase transition. Further studies into the zone center phonon dynamics [54], announced the potential origin of the soft mode to exist outside the Brillouin zone center, while associating

the zone central mode with the anharmonic vibrations within the lattice.

In summary, in all of the above mentioned studies, the behaviour of the phonon modes was analysed very close to the Brillouin zone center, through the study of only the Γ point. Whereas the role played by the instabilities at the Σ point (lying far from the zone center), and the R point (lying at the zone boundary), which are as important to describe the change in the structure of $PbZrO_3$ in the antiferroelectric phase, have remained unanalysed. A study of the off-zone center phonon behaviour of $PbZrO_3$, thus, would help enunciate the role of the potential instabilities at these points to explain the phase transition in $PbZrO_3$, and would provide valuable information on the appointment of the primary order parameter associated with the phase transition, which in turn triggers the appearance of the other competing instabilities.

2.2 Competing Instabilities

Perovskite oxides exhibit a wide range of ferrodistortive and antiferrodistortive phase transitions, resulting in ferroelectric or antiferroelectric behaviour in the system, each of which is associated with a lattice instability (and thus with an order parameter in phenomenological theory) controlling the feature. The presence of more than one order parameter in a system defines the system as a multiferroic. The simultaneous coexistence of multiple instabilities in the system often results in them competing with one another, with the presence of one ultimately resulting in the absence of the other [55]. Balashova and Tagantsev [56] have shown using a phenomenological model consisting of two order parameters (one polar and one non-polar), that depending on the interaction between the two order parameters, a range of behaviour can be predicted varying from ferroelectric to antiferroelectric. The same model was applied to betaine arsenate [57] and the experimentally obtained results corresponding to the phase transitions in the system were successfully explained.

$SrTiO_3$ is another system known to have competing structural and polar instabilities [55], with a ferroelectric soft mode at the Brillouin zone center and an antiferrodistortive soft mode associated with the octahedral rotations at the R point of the Brillouin zone boundary. In this case, the suppression of the ferroelectricity was associated with the presence of the structural order parameter [58], implying that the absence of a structural order parameter could potentially result in the appearance of the ferroelectric order parameter. Tagantsev et al [59] developed a model based on the Gibbs model for the free energy of the system consisting of not only the elements from the previously developed model by Uwe and Sakado

[60], but also using the gradient terms previously described by Cao and Barsch [61], in order to include in the free energy formulation the contributions of the domains as well as the domain boundaries seperating regions with two different orientations of the order parameter. Applying this theory to the domain boundaries seperating two domains having the structural order parameter out of phase with respect to each other, the study predicts the appearance of a ferroelectric order parameter in the region where the structural order parameter is modified w.r.t. its equilibrium value in either domain.

This concept of competing instabilities is of particular interest when considering the case of the phase transition in $PbZrO_3$, since $PbZrO_3$ consists of a complex combination of multiple order parameters competing against each other. An understanding of the interaction between these competing instabilities would prove useful in the potential observation of regions where the absence of the primary order parameter suppressing the ferroelectricity, would result in the appearance of the ferroelectric order parameter.

2.3 Domains and domain walls

Domains can be defined as spatial entities wherein the magnitude and the orientation of a certain order parameter remains constant. Domains corresponding to different magnitude and orientation of the order parameter in question (select to those allowed from the symmetry of the material) coexist adjacent to one another when certain conditions established by mechanical and electrical compatibility of the two domains are fulfilled [24]. Since the order parameters are related to the symmetry of the system in ferroics, the relation between two domains can be described by the change in the lattice symmetry from one domain to the other, which can be either rotational or translational, or both. The region bordering such neighbouring domains, called domain walls or boundaries, are often areas subject to deviation of the order parameters away from the equilibrium values, and are known to exhibit properties anomalous to those normally observed from the domains themselves.

2.3.1 Anomalous behaviour of ferroic domain walls

In the case of systems with competing order parameters, owing to the local deviation of the primary order parameter in the domain wall, the instabilities previously subdued by the presence of the primary order parameter could potentially find themselves activated. In the case of $CaTiO_3$, the oxygen octahedra rotation suppresses the displacement of the Ti ions, resulting in the formation of a non-polar system. In such a case, along the twin boundaries
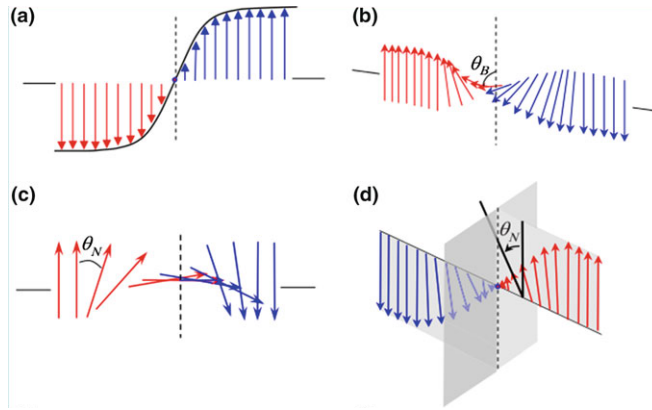
Figure 2.5: Different kinds of ferroic domain walls showing the variation of the order parameter across the boundary (a) Ising wall (b) Bloch wall (c) Neel wall (d) Mixed Ising-Neel wall. [62]

wherein the TiO_6 octahedral tilts are disturbed, the formation of polar clusters from the displacement of the Ti ions results in a polarity along such boundaries [63, 64].

In the tetragonal phase of $SrTiO_3$, the domain wall adjoining two domains whose oxygen octahedra rotations are 180° out of phase with respect to one another (hence called anti-phase domain boundary) was examined using phenomenological theory [59] to observe the appearance of the subdued "ferroelectric" order parameter over the variation of the primary "structural" order parameter. As foreseen, where the structural order parameter was found to be reduced along these boundaries, the ferroelectric order parameter was evoked, and a polarisation of 4.2 $\mu C/cm^2$ was estimated.

The potential utility of such ferroelectric entities in a non-ferroelectric matrix is underplayed owing to the low temperatures at which they are predicted to occur. Given the case of multiple competing instabilities in $PbZrO_3$, with a phase transition at much higher temperatures, the discovery of local ferroelectric behaviour at ambient temperatures would thus be of immense interest.

2.3.2 Domain structure in PbZrO$_3$

The understanding of the domain structure in $PbZrO_3$ was crucial to establish the non-polarity of the a-b plane. Jona et al [65] studied the formation of domains in $PbZrO_3$ by means of polarised optical microscopy, and observed the existence of 90° and 60° domains with the domain wall oriented along the $[110]_o$ and $[111]_o$ directions. A later study [66] claimed the existence of 180° domains through observations conducted on etched specimens in a transmission electron microscope.The simultaneous existence of all the three domain variants, i.e.
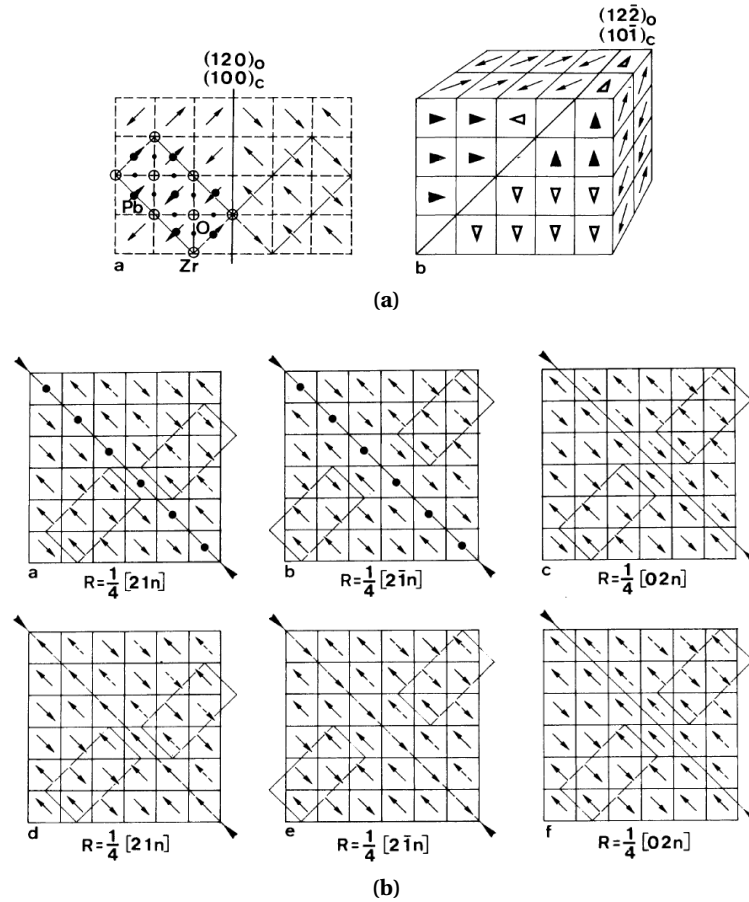
Figure 2.6: (a)Reconstruction of the 90° (left) and the 60° (right) twins in PbZrO$_3$ based on the pseudocubic unit cell, with the head to tail arrangement being satisfied at the boundary. The domains are related through a simple rotational transformation matrix. (b) Schematic reconstruction of the 180° (α) boundaries in PbZrO$_3$, with domains related through a displacement vector representing the vector describing the translational mismatch between the unit cells two domains (given by R). [67]

90°, 60° and 180° was shown by Tanaka et al [67] through convergent-beam electron diffraction. The importance of this study lies in the distinction established between simple 'twin' structure observed for the 90° and the 60° domains, and the α boundary feature of the 180° domain wall, which is solely characteristic of antiferroelectric materials. Whereas the 'twin walls' are boundaries across which the domains change their crystallographic orientation by a purely rotational transformation vector (see Fig. 2.6(a)), the 180° walls or the α boundaries are characterised by a displacement vector. In this study were also proposed the different variants possible for the formation of such α boundaries (see Fig. 2.6(b)), corresponding to different displacement vectors. The potential presence of a local ferroelectricity was also proposed for the cases where the boundaries are characterised by the displacement vectors R=$\frac{1}{4}$[21n] and R=$\frac{1}{4}$[02n], though no observation or reasoning for this local polarity was provided.
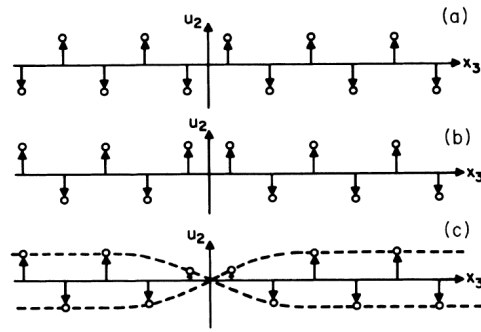
Figure 2.7: Illustration of an antiphase domain boundary in a system with the order parameter defined by the alternative displacement of the ions perpendicular to the x_3 axis. (a) Single domain (b) Discontinous antiphase domain boundary (c) Continous antiphase domain boundary. [61]

2.3.3 Antiphase domain boundaries

Antiphase domain boundaries are planar defects that seperate two domains where the order parameter in one domain is 180^0 out of phase with respect to the other. By virtue of its definition as a planar defect, an antiphase domain boundary entitles a local disruption of symmetry. Figure 2.7 demonstrates the concept of an antiphase domain boundary. In this example, the displacement of the ion acts as the order parameter for the single domain (Fig. 2.7 (a)) and a break in the phase of the displacement of this ion results in the formation of an antiphase domain boundary which might be abrupt (Fig. 2.7 (b)) or continous (Fig. 2.7 (c)). This being the simplest definition possible for the description of an antiphase domain boundary, the order parameter used to define an antiphase boundary could also consider the oxygen octahedral rotations.

Antiphase domain boundaries can also be linked to dislocations, since both defects are associated with an additional half plane in the crystalline lattice. Considering a perfect lattice of $SrTiO_3$ with the oxygen octahedral rotations as seen along the c axis in the tetragonal phase (see Fig. 2.8(a), shaded in gray), on the introduction of a dislocation (shaded red in Fig. 2.8 (b)) within this crystalline arrangement, i.e. by removing one unit cell from the top half of the structure, the local symmetry is reduced, and the oxygen octahedra on the right side of the dislocation are exactly 180° out of phase with respect to the octahedra on the left side of the dislocation. Hence, the missing half-plane around the dislocation would correspond, technically, to an antiphase domain boundary, seperating two antiphase domains (as described by the oxygen octahedral tilts) on either side.

It is thus not surprising that later on, microscopic examination of thin films of orthorhombic $SrRuO_3$ remarked the presence of antiphase boundaries alongside misfit dislocations [68, 69].

(a)

(b)
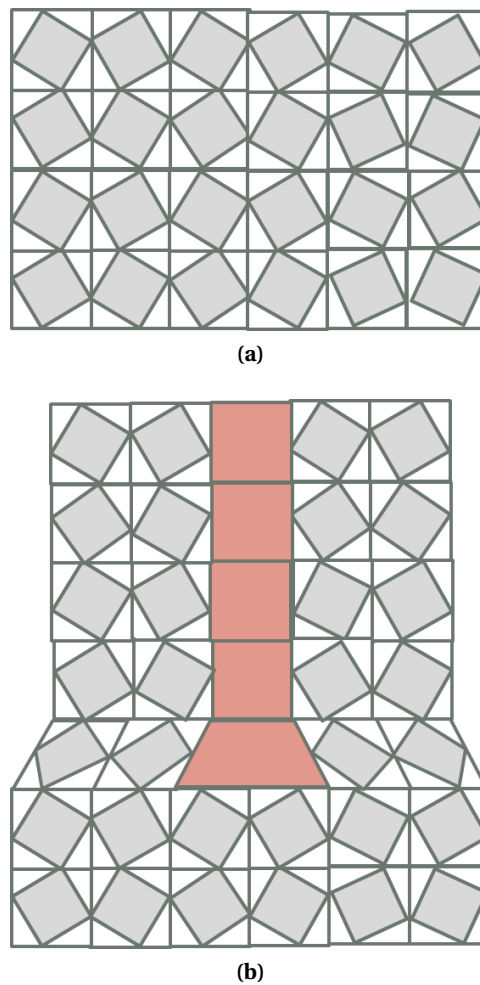
Figure 2.8: (a)Representation of a perfect crystalline lattice of tetragonal SrTiO$_3$ as seen along the c-axis, with the continuum in the oxygen octahedra (shaded gray) seen over the entire domain (b) Formation of an antiphase domain boundary (shaded in red) in the vicinity of the dislocation owing to the missing lattice unit.

In the search of antiphase domain boundaries in PbZrO$_3$, thus, dislocations could prove to be effective pointers.

2.4 Thin films

Thin films are material layers whose thickness varies from a fraction of a nanometer to several micrometers. The development and the understanding of processes associated with the growth of thin films allows for a precise control of the structure, and hence the properties, of the material concerned. Alongside, owing to the reduction of the dimension of the material, ferroic thin films allow for the integration of the material in various applications concerning micromechanical devices and non-volatile memories, aiding in the miniaturisation of

upcoming technologies.

Fabrication of thin films can be classified broadly into two subcategories: physical and chemical. In physical deposition techniques, a vapourised phase of the desired material is allowed to condense onto various workpiece (or substrate) surfaces. The vapourised phase of the material can be formed by various means: resistive heating into a vapour phase (evaporation), from a high power electric discharge (cathodic arc deposition), electron beam bombardment (electron beam physical vapour deposition), bombardment by a plasma discharge in an external magnetic field (sputter deposition), and ablation from a high power laser (pulsed laser deposition), to name a few. In chemical deposition techniques, reactants are introduced either in the vapour phase in the deposition chamber (chemical vapour deposition) or in the liquid phase on the surface of the substrate (e.g. sol-gel), and the conditions are moderated to allow for the reaction to occur, wherein the resulting product(s)formed/asdorbed on the substrate surface correspond to the desired composition for the thin film.

The current study will focus on the growth of thin films of $PbZrO_3$ from the vapour phase and the mechanisms accompanying such growth are discussed below.

2.4.1 Thin films: Nucleation and Growth

In a high energy process such as Pulsed Laser Deposition, the atoms arriving at the surface of the substrate usually have an energy much higher than that necessary for the diffusion along the surface, or that for desorption. Most of this energy is immediately dissipated by the interaction with the phonon vibrations in the substrate. These entities then exist in a high density vapour state. Among these entities (referred to as 'adatoms'), though some of them have enough energy to re-evaporate, most of them do not have enough energy to escape, and diffuse along the surface to accumulate and form metastable clusters[70], with the possiblity of incoming atoms to be deabsorbed being still high. These clusters become stable when the flux of incoming atoms is higher than the flux of the deabsorbed atoms, and the clusters are then called nuclei. The free energy for the formation of such a stable cluster can be described using the following equation

$$\Delta G = a_1 r^2 \Gamma_{c-v} + a_2 r^2 \Gamma_{s-c} - a_2 r^2 \Gamma_{s-v} + a_3 r^3 \Delta G_V \tag{2.2}$$

where r is the radius of the cluster, the Γ's are the interfacial energies (the subscripts s,c and v
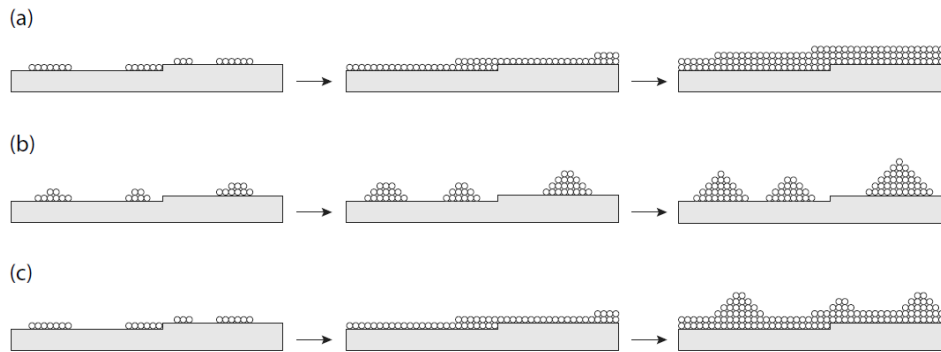
Figure 2.9: Illustration of the three growth modes depending on the surface energies (a) 2-Dimensional or Frank-Van der Merwe mode (b) 3-Dimensional or Volmer-Weber Mode (c) Mixed or Stranski-Krastanov mode.

stand for substrate, cluster and vapour respectively), ΔG_v stands for the change in the volume free energy on the formation of the cluster and the a's are constants dependant on the shape of the nuclei. Depending on the thermodynamics relating the surface energies (of the film and the substrate) and their interfacial energy as described above, three basic nucleation and growth modes can be enumerated [71, 72] (illustrated in Fig. 2.9). If $a_2\Gamma_{s-v} > a_1\Gamma_{c-v} + a_2\Gamma_{s-c}$, the film completely wets the surface to minimise the surface energies and growth occurs in a layer-by-layer fashion (called the Frank van der Merwe mode, Fig.2.9(a)). On the other hand, if $a_2\Gamma_{s-v} < a_1\Gamma_{c-v} + a_2\Gamma_{s-c}$, the volume energy dominates the free energy and the surface energy is minimised by the the formation of islands which grow in a 3-dimensional fashion to eventually coalesce with one another (called Volmer-Weber mode, Fig. 2.9(b)). In the case of heteroepitaxy with a certain mismatch, it is also possible that that the film starts to grow by the Frank van der Merwe mode but after a certain thickness relaxes the elastic strain through the formation of 3-dimensional islands, resulting in a mixed dimensionality (called Stranski-Krastanov mode, Fig. 2.9(c)).

In order to have single crystalline films, a fixed relation between the crystallographic planes of the film and the crystallographic planes of the single-crystalline substrate is to be ensured. Such films that have a fixed relation of their crystallographic planes with the crystallographic planes of the substrate are called epitaxial thin films. Low index crystalline planes are usually used for the substrate surface for epitaxial film growth. When the cutting angle used to obtain such low index planes varies by small values (usually between 0.05^o and 0.2^o), the surface is formed by lamellar terraces with a height equal to one interplanar distance (see Fig. 2.10 (a)). These are called vicinal faces and act as diffusion barriers (for interlayer diffusion) during the growth of thin films [73]. Such factors are important during the growth of thin films for the growth mode is determined not only by the thermodynamic conditions discussed above,
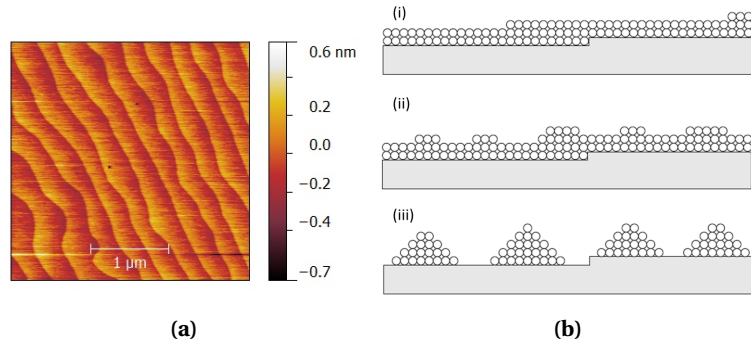
Figure 2.10: (a)AFM image of a (100) oriented SrTiO$_3$ substrate showing vicinal terraces of one unit cell height (0.39nm.) . (b) Illustration of kinetic growth modes of thin films on vicinal surfaces (i) Step flow growth (ii)layer-by-layer growth (iii)island growth (kinetic roughening)

but also from the kinetics associated with factors such as vicinal surfaces. If the energy of the adatoms is high enough to overcome all interlayer and across layer diffusion barriers, and the diffusion length is higher than the terrace width, the adatoms diffuse to join the closest terrace leading to step-flow growth (Fig. 2.10(b)(i)). When the energy is sufficiently high for interlayer and within layer diffusion, but the diffusion length is less than that of the terrace width, the growth proceeds by the two-dimensional islands resulting in a layer-by-layer growth (Fig. 2.10(b)(ii)). On the other hand, when the adatoms do not contain sufficient energy for interlayer diffusion, the growth proceeds through the formation of 3-dimensional islands, called kinetic roughening(Fig. 2.10(b)(iii)).

2.4.2 Epitaxial strain and relaxation

Epitaxial films grown on substrates of the same compositions are called homoepitaxial, whereas epitaxial films grown on substrates of a different composition are called heteroepitaxial. In most cases of heteroepitaxy, the lattice parameter of the thin film material is different from that of the substrate, resulting in a strain at the interface known as epitaxial strain. Given the lattice parameter of the substrate (a_s) and the lattice spacing in the corresponding direction in the film (a_f), the in-plane uniaxial strain (f) is given by Eq. 2.3.

$$f \quad = \quad \frac{a_s - a_f}{\frac{a_s + a_f}{2}} \tag{2.3}$$

During the growth of an epitaxial thin film, initially the film grows in a way to match perfectly the crystalline lattice of the substrate (i.e. pseudomorphically). Once a critical thickness (h_c)

of the film is reached, the thus-grown film is then capable of releasing the strain built into its lattice at the interface through the formation of misfit dislocations. During the formation of the misfit dislocations, in the case of a tensile epitaxial strain in the film, an extra half plane is added in the film, whereas in the case of a compressive epitaxial strain in the film, a half plane is absent from the film. For a thin film, while neglecting the elastic energy of the substrate, the energy of an epitaxially strained film contains two components: the elastic energy of the films and the energy for the creation of the dislocations. While the elastic energy in the film from the epitaxial strain varies linearly with the film thickness, the energy released per dislocation varies logarithmically with the film thickness [74]. From the total energy from the two contributions, the critical thickness is defined as the thickness when the energy released from the formation of a dislocation is equal to the elastic energy stored in the film from the misfit dislocation. The expression for the estimation of critical thickness, known as the Matthew-Blakeslee criterion, is expressed as the following:

$$ h_c \quad = \quad \frac{b}{2\pi f} \frac{1 - \nu \cos^2 \alpha}{(1 + \nu) \cos \lambda} (ln \frac{h_c}{b} + 1) \tag{2.4} $$

where b is the burgers vector for the dislocation, ν is the Poissons ratio, α is the angle between the dislocation line and its burgers vector, λ is the angle between the slip direction and the direction perpendicular to the intersection between the slip plane and the dislocation line. This estimation is valid only for small values of the misfit strain (typically less than 2 %), and for monolayered thin films. Since the Matthew-Blakeslee criterion considers only the energetics behind the formation of dislocations without including the dynamics, the criterion finds itself to be often limited. For cases considering epitaxial strains higher than 3 %, the critical thickness drops down to a few unit cells [75], and for those exceeding 5 %, to less than the lattice constant, implying higher dependance on the dynamics than the energetics. On the other hand, thin films (especially of ionic oxides) grown far beyond the critical thickness without the formation of equilibrium density of dislocations are also often reported [76, 77], since the high Peierl's Nabarro stress prevents the relaxation of the misfit strain through the formation of dislocations.

The variation of epitaxial strain is of particular interest in thin films, especially in ferroics, since it directly affects not only the domain fractions [78–80], but also the phase transition temperature [79], and the structure [81, 82] of the film among other properties. The study of ferroic properties as a function of the epitaxial strain has thus held immense interest. The possibilities for varying the lattice strain are, nevertheless, limited. For films grown with fairly

low values of epitaxial strain (<2%), given the large critical thickness, the thickness of the film can be varied to change the strain contained within the film, by allowing the film to relax to different extents by limited dislocation formation. This technique fails for thin films grown with larger epitaxial strain since the large strains facilitate the formation of dislocations (thus causing rapid relaxation) early into the growth. Another technique for varying the interfacial epitaxial strain is to change the substrate composition. By varying the substrate composition, the lattice parameter of the substrate can be varied, thus varying the epitaxial strain. This is a fairly limited method since the choice of substrates is far from being vast. Finally, the use of a buffer layer to modulate the epitaxial strain has been previously exploited for thin films [78, 83] in which the growth of an intermediate layer between the substrate and the film results in the formation of a pseudo-substrate on which the desired film may be grown under the conditions desired. To this effect, when using conventional substrates (whose lattice parameter varies usually between 0.37 and 0.39 nm) for the growth of thin films whose lattice parameter exhibits more than 4% lattice mismatch, the use of relaxed films of $BaZrO_3$ as buffer layers is well documented [84–86] owing to its elastic compatibility and easy growth [87]. Nevertheless, despite all these improvements in the field of growth of perovskites no existing technique allows for the possibility of a continuous variation of the epitaxial strain.

2.4.3   Thin films of PbZrO$_3$

Interest in thin films of $PbZrO_3$ arose initially to complete the understanding of growth of high zirconia content $Pb(Zr_{1-x} Ti_x)O_3$ systems [88]. But with the increased interest in the giant electrostrictive effect observed in antiferroelectric materials, more attention was given to the understanding of $PbZrO_3$ films and their growth. Several techniques including sol-gel [89–91], sputtering [92–94], molecular beam epitaxy [94] and pulsed laser deposition [43, 95–98] have been used to produce thin films of $PbZrO_3$.

It is of no surprise that the microstructure of the films thus grown and their properties depend heavily on the growth process [91]. Most of the films were grown on either Si [89, 99] or on $SrTiO_3$ [43, 98] substrates, with or without the usage of an intermediate buffer layer such as $PbTiO_3$[100] or $BaZrO_3/BaPbO_3$ [98]. Though a high preference of the orientation was achieved through all the initial trials for deposition [89], the films mostly remained multi-grained [97]. Nevertheless, the films did demonstrate the typical antiferroelectric behaviour expected from $PbZrO_3$, namely, the double hysteresis loops and the dielectric anomaly at the phase transition temperature (see Fig. 2.11).

The explanation for the appearance of the double hysteresis has always been related to the
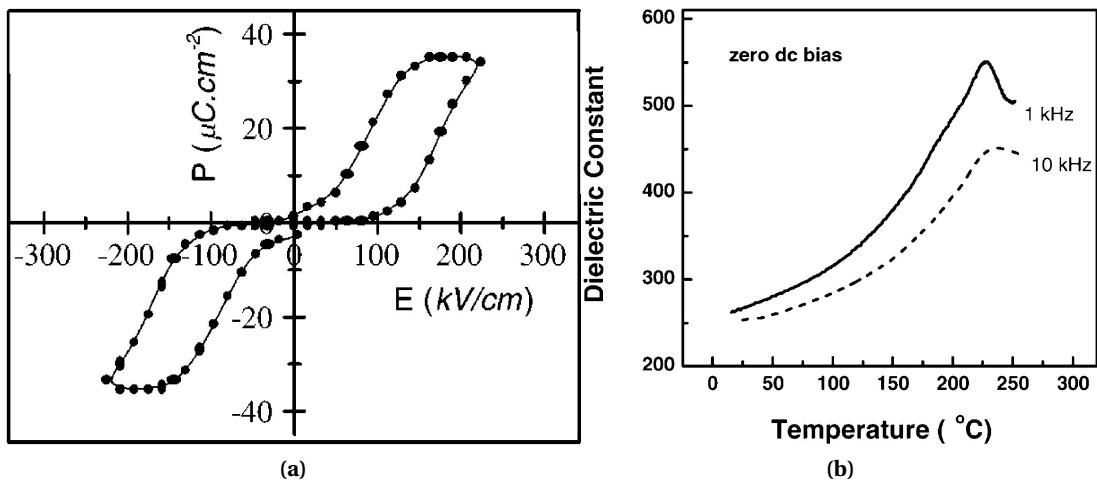
Figure 2.11: (a)Double hysteresis loops (b) Dielectric constant peak at the curie temperature, seen from thin films of $PbZrO_3$ deposited on Pt-coated Si substrates [97]

proposed "field induced ferroelectric phase transition". Such observations, though previously known for single crystals, have not been observed for bulk ceramics since the critical fields necessary for the proposed "induced transition" is beyond the breakdown field of the material [101]. Thin films, on the other hand, prove useful in the understanding of the influence of external factors on such traits of antiferroelectric behaviour, since they allow for a higher control of the stress state, the composition, and the orientation of the sample.

Since the closest ferroelectric phase to the orthorhombic antiferroelectric phase in the phase diagram of Pb $(Zr_{1-x} Ti_x)O_3$ system is of a rhombohedral symmetry, and since the intermediate ferroelectric phase observed occasionally in between the paraelectric and the antiferroelectric phase is of rhombohedral symmetry as well, the "ferroelectric" phase supposed to be "induced" at either extremity of the double hysteresis loop was assumed to have a rhombohedral symmetry. Through experiments and calculations carried out through various studies [8, 40, 41], the free energies of the orthorhombic phase and the "ferroelectric" rhombohedral phase were shown to be very close to one another, thus supporting the argument that the double hysteresis loop was a result of the "field-induced" transition of the material into a rhombohedral "ferroelectric" phase. Despite frequent observations of these hystereses loops, there has been no proof of the existence of this claimed ferroelectric phase in the absence of an external electric field. Without casting any doubt on the validity of the above observations, since by definition a ferroelectric material presents a spontaneous polarisation in the absence of an external electric field, the above proposed terminology is found to be inconsistent.

The effect of lattice strain on the antiferroelectric behaviour of $PbZrO_3$ has also been studied

through the variation of epitaxial strain on thin films. Through the study of epitaxial films grown on $SrRuO_3$ (with 5.8 % compressive strain) and on $BaPbO_3$ (with 1.2% tensile strain) [98], the films were seen to be oriented (in the orthorhombic phase) along the (120) or 'a_o' axis and along (001) or 'c_o' axis respectively, which was explained through the mechanical compatibility of the domains with the imposed stress state at the interface. Films of both orientations were seen to be antiferroelectric, with the 'a_o' oriented film demonstrating a small amount of remnant polarisation. The study showed a raise in the phase transition temperature by 30K in the case of a compressive strain, though the effect of the tensile strain on the phase transition is unknown. Moreover, while the 'c_o' oriented films were shown to have complete ferroelectric behaviour at low temperatures, the 'a_o' oriented film was seen to have mixed ferroelectric-antiferroelectric behaviour (seen from a triple hysteresis loop) at similar temperatures [43]. This was explained through the stabilisation of different 'potential' orientations (including a rhombohedral and a tetragonal type of polarisation) for the polarisation depending on the orientation of the film, and the direction of the applied field, though no evidence for the orientation of the polarisation through structural analyses of these phases has been given. When compared with existing studies on the stability of the potential 'ferroelectric phase' of $PbZrO_3$, the above study is found to be contradictory to density-functional theory calculations [102], wherein the stabilisation of the ferroelectric phase was suggested in the case of compressive strain only.

Meanwhile, there seems to exist as well a lacking consistency in the exact minimal thickness necessary for the disappearance of ferroelectric behaviour. For the case of $PbZrO_3$ films grown on Pt-coated Si alone, the minimum thickness of the film needed for the change from single hysteresis loop to double hysteresis loops varies from 80nm [89] to 260nm [99]. In the case of epitaxially grown $PbZrO_3$ films of varying thickness on $SrRuO_3$ electrodes, the change from a pure rhombohedral phase below 8nm thickness to a mixture of a rhombohedral and orthorhombic phases, to a pure orthorhombic phase above 22nm film thickness was associated with the origin of ferroelectricity seen at ultrathin films of $PbZrO_3$, though no such phase was observed in previous studies [98]. The appearance of such ferroelectricity has also been previously attributed to defects and surface charges [89] and self biasing [95]. Thus, in general, though there exist multiple examples of the dwindling ferroelectric-antiferroelectric behaviour in $PbZrO_3$ possibly induced from multiple sources, no concrete consensus on the explanation of these observations is currently existant.
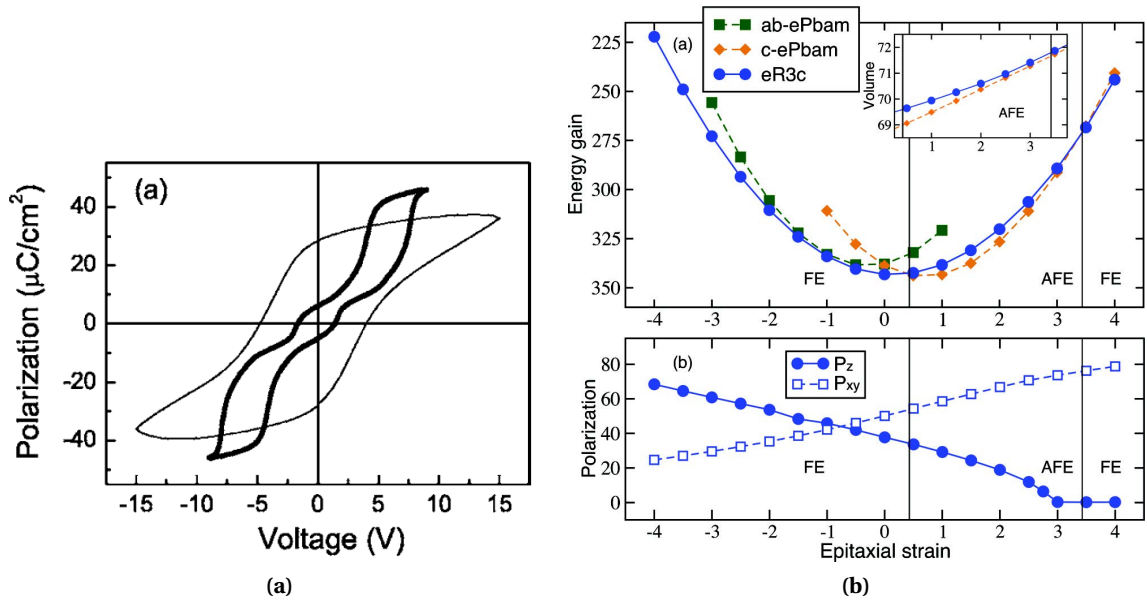
Figure 2.12: (a)Hystereses loops for an 'a$_o$' oriented (thick line) and for a 'c$_o$ oriented (thin line) PbZrO$_3$ film at 4.2K showing the mixed-ferroelectric-antiferroelectric behaviour of the former and the ferroelectric behaviour of the latter [43] (b) DFT calculations showing the stability of the different ferroelectric (eR3c, rhombohedral) and antiferroelectric (ab-e Pbam and c-ePbam, orthorhombic) phases for varying epitaxial strain, showing the preferred stability of the ferroelectric phase in the case of compressive strains [102]. The two studies are seen to be contradictory to one another, with no consensus on the exact relation between the appearance of ferroelectricity and epitaxial strain being established.

2.5 Control of defects in thin films

Macroscopic crystalline defects such as stacking faults, dislocations (partial and full) and antiphase boundaries are often encountered in thin films. The presence of such defects in ferroelectric thin films causes significant change in the behaviour of materials in many ways, like local backswitching in the vicinity of dislocations [103], pinning of domain walls [104], formation of a non-reactive dead layer at the interface from the misfit dislocations [105], asymettric ferroelectric loops [106] to name a few. On the other hand, the absence of these defects in cases of heteroepitaxial growth allows for the retention of the elastic strain in the lattice, which indirectly changes the ferroelectric properties, for example, through the change in the domain fractions [107]. An understanding of the origin and the nature of such defects is, thus, important for the comprehension of the effects seen thereafter.

2.5.1 Origin of defects in thin films

Following from the theory developed in Section 2.4.2, the formation of misfit dislocations for strain release during thin film growth is favoured only once the critical thickness h$_c$ is
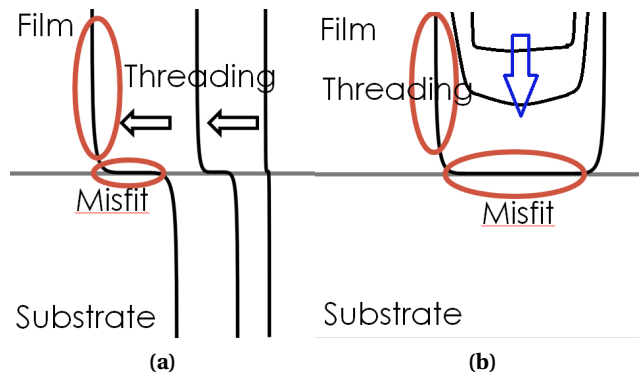
Figure 2.13: Illustration of the two sources of misfit dislocations in thin films (a) Through the propagation of existing dislocations in the substrate upto the surface (called threading dislocation), these dislocations can glide along the surface resulting in a section parallel to the interface (called misfit dislocation), causing the release of misfit strain. (b)Through the formation of half loops at the free surface, when a dislocation segment parallel to the interface (held by two threading segments perpendicular) climbs down the thickness of the film to reach the interface and release the misfit strain.

crossed. At this stage in the thin film growth, there are many possible sources for the origin of dislocations in the thin films. In the case of perfect epitaxy, existing dislocations in the substrate/underlayers can be grown into the growth of the thin film, growing upwards from the film-substrate interface upto the surface of the film, called a 'threading dislocation', which does not participate in the strain release process. Once the critical thickness has been crossed, the threading segments begin to grow along the interface, resulting in the release of the misfit strain and this segment of the dislocation line lying along the interface is called the 'misfit dislocation' (see Fig. 2.13(a)).

A second mechanism for the nucleation of dislocation is through the formation of half loops at the free surface. In this mechanism a local perturbation in the growth results in the breaking of the local symmetry, resulting in the formation of a dislocation line close to the surface (known as a half loop), consisting of two threading segments (perpendicular to the interface) joined by a misfit segment (parallel to the interface). With time, the threading segments can both 'climb' down the thickness of the film resulting in the lowering of the misfit segment. This usually ends with the misfit segment reaching the interface and releasing the misfit strain. This mechanism is more active in the case of chaotic growth conditions. Once the threading segments have lowered the misfit segment all the way to the interface, they can also grow similar to the previous mechanism, to result in the elongation of (and further strain release from) the misfit segment.

Other defects such as antiphase boundaries are formed when the symmetry between two adjoining areas of the film are shifted by a fraction of a translational symmetry vector. In the
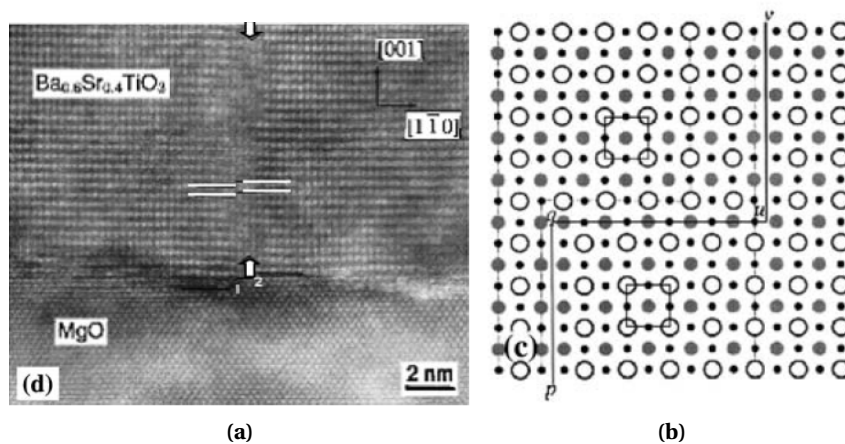
Figure 2.14: (a)TEM image showing the formation of an antiphase boundary (marked by arrows) across the step edge bordering two terraces (labelled 1 and 2) in a thin film of $Ba_{0.6}Sr_{0.4}TiO_3$ on MgO substrate [108](b)Illustration showing the atomic arrangement on a planar view of the thin film along a kink on the terrace edge accompanied with an antiphase domain boundary. [108]

case of vicinal substrates, this shift in the symmetry can occur either at the step edge [108] (see Fig. 2.14(a)), or across a kink along the terrace (see Fig. 2.14 (b)). Observations of antiphase boundaries associated with the step edge have been made for thin films of $Ba_{0.6}Sr_{0.4}TiO_3$ on MgO substrates [108] and for $SrRuO_3$ films on $SrTiO_3$ subtrates [68, 69].

2.5.2 Control of planar defects in thin films

Given that misfit dislocations are a direct result of the relaxation of thin films grown with a heteroepitaxial strain, the most direct way of controlling the misfit dislocation density would be through the control of interfacial strain. Due to a lack of a variety of substrates (of varying lattice parameters), this simple concept falls short of direct implementation. The use of buffer layers to form pseudo substrates has been known before (see Section 2.4.2), but the possibility of tuning the interfacial strain has so far remained unachieved to our knowledge. Threading dislocation density has been previously controlled during the growth of semiconductor thin films through the introduction of buffer layers as well [109, 110].

The dynamics of the growth of thin films including such parameters as growth rate, growth temperature and ambient pressure can have an impact on the nature and the density of the defects present as well. In the case of a step flow growth of low lattice misfit films , the growth occurs in a quasi-equilibrium state thus obeying the Matthew-Blakeslee condition, yielding dislocations only at thicknesses above the critical value. But these conditions break down in the case of a system with a high lattice misfit, or with volatile components(or both) or in cases

25

of high growth rate. By simply controlling the growth rate, the growth conditions were shifted away from equilibrium and epitaxial thin films of $BaTiO_3$ have been prepared previously in full strained, partially strained and fully relaxed conditions [107] corresponding thus to varying dislocation densities. By the growth of films in the island mode, the coalescence of two islands can result in the formation of the half loop [74], which act as source for dislocations as previously explained. In cases of high lattice misfit, of compositions containing a volatile oxide, or of change in the growth conditions (e.g. lowering of temperature), such non-equilibrium growth can be attained in thin films, resulting in the formation of more threading dislocations. The control of dislocations is thus possible by controlling the various aspects associated with equilibriated or dynamic growth as well.

2.6 Objectives of current work

With the backing of all the information presented previously, the current work treats $PbZrO_3$ as a prototypical antiferroelectric in search of a precise model to explain the phase transition and the structure in the material while also incorporating the features currently known. The question of the origin of antiferroelectricity will be approached through analysis of the vibrational modes outside of the Brillouin zone center. This understanding will elucidate the roles and the coupling between various instabilities during the phase transition, which is crucial in the search for localised ferroelectric behaviour in an antiferroelectric material such as $PbZrO_3$. Using the theoretical framework for describing the origin of antiferroelectricity, the requirements for localised ferroelectricity can be obtained, and used for its observation. In this study, the observations will be carried out in thin films that allow for localised strain engineering while permitting also dielectric analyses on the macroscopic scale.

In other words, the study aims at answering the following questions:

? What is the nature of the transition in $PbZrO_3$? What kind of interactions does one notice between the instabilities in the system? What is the exact reason for the suppression of ferroelectricity and how does it (/do they) cause the antiferroelectic nature of the system?

? What are the conditions for the extinction of the order parameter associated with the suppression of ferroelectricity? What structures correspond to these conditions and how can they be realised in thin films of $PbZrO_3$? How do they react to an external electric field?

? What kind of domain walls exist in $PbZrO_3$? How do the competing instabilities behave across these domain walls? How do they affect the local dielectric properties?

? What is the local atomic structure along these boundaries? Does one observe a ferroelectric transition across these boundaries?

3 Experimental Techniques

This chapter enunciates the details of the experimental techniques used towards the understanding of $PbZrO_3$ as a prototypical antiferroelectric. Various techniques were used to understand the lattice instabilities and dynamics in single crystal $PbZrO_3$ samples, most of them for the first time. Alongside, thin films of $PbZrO_3$ were grown and characterised, with control on the structural quality of the films. The hence prepared films were characterised for their dielectric properties.

3.1   Material Preparation Techniques

For the experiments concerning the understanding of the lattice instabilities and the dynamics of $PbZrO_3$, single crystals were used in order to avoid the contribution of grain boundaries, while having minimal defects in the structure. To this end, single crystals of $PbZrO_3$ were grown using a flux growth method in collaboration with Institute of Physics, University of Silesia, Krakow, under the guidance of Prof.K. Roleder. Meanwhile, thin films of $PbZrO_3$ were grown for the observation of the antiphase domain boundaries and for achieving a control on their density. Simultaneously, for intricate control of the epitaxial strain experienced by the film, and for the understanding of the variation in the dielectric behaviour with the presence of this epitaxial strain, thin films prove to be ideal. For the growth of these thin films, Pulsed Laser Deposition technique was used.

3.1.1   Flux Crystal Growth

The crystals were prepared by a molten flux growth method where in a crucible of highly stable, non-reactive material, the oxides are dissolved in a solvent (or flux, B_2O_3 in this case) at

high temperatures (here ~1350K). When cooling this solution in a very slow fashion at 3.5K/h down to 1210K, the cystals start to crystalise along the walls of the crucible, at which point the remaining solution was decanted and the crystals are cooled down at 10K/h. Finally, the crystals are washed with dilute acetic acid to remove any traces of the flux. The crystals used in this study were grown at the Institute of Physics, University of Silesia, Katowice (Poland).

3.1.2 Pulsed Laser Deposition

Since its first trial in 1965 [111], Pulsed Laser Deposition (PLD) has evolved as a technique for the deposition of thin films. Though initially lagging behind other techniques such as Molecular Beam Epitaxy (MBE) and sputtering, PLD re-emerged as a technique for the growth of epitaxial thin films with advances made in laser technology. Its significance was established through the work of Cheung and Magee [112] wherein semiconductor thin films deposited by PLD were shown to have very high crystalline quality. Currently, it is one of the most versatile physical vapour deposition methods used for the deposition of a wide range of materials including metals[113], high-temperature superconductors[114], ferroelectrics [115], and ferromagnets [116] to name a few.

The operational principle of the PLD is as follows (refer Fig. 3.1): a focussed excimer laser beam strikes at a rotating target at a preset frequency, causing the excitation of the atoms at the surface of the target and resulting in a high energy plasma plume, which then deposits on the substrate. The individual steps that amount to the final film are crucial to the structural control and are discussed briefly below.

When the laser strikes the target (stage 1), a rapid heating of the ablated region occurs followed by its vaporisation, which owing to the high energy of the laser breaks down and forms a dense plasma (stage 2). The rest of the pulse is used to heat and accelerate the plasma, which contains neutral atoms, ions and electrons, occuring in natural as well as in excited states. Right above the surface of the target these excited entities collide with each other, forming a dense layer (called Knudsen Layer), thus losing a part of their kinetic energy achieved from the ablation. Once beyond the Knudsen layer, out of the high plume pressure, the particles fly out perpendicular to the surface of the ablated target to form an expanding fluorescent plume (stage 3). The presence of a background gas in the deposition chamber causes the collision of these particles with the gas molecules, thus causing a deceleration with increasing distance (stage 4). Finally, only the particles that retain enough energy after these stages reach the surface of the heated substrate situated at a certain distance from the target (5-10 mm.) and get adsorbed onto it (stage 5). The substrate is usually held at high temperatures during the
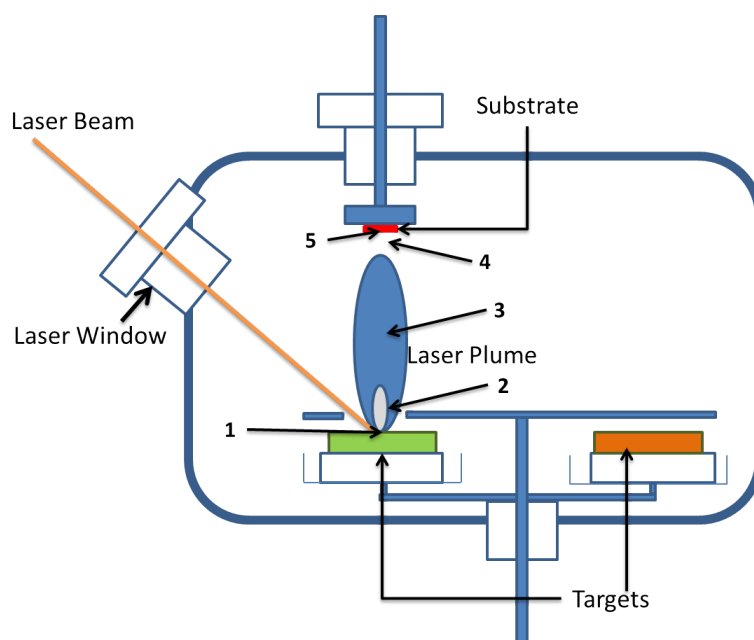
Figure 3.1: Illustration of the PLD deposition chamber showing the different components such as the target carousel, the substrate holder and the laser beam path. The different stages of the deposition process as described are denoted as well.

deposition period in order to allow for an easy diffusion of the particles reaching the surface, promoting the formation of films with better structural properties.

By controlling the various parameters associated with the above described process, it is possible to obtain amorphous, polycrystalline or epitaxial films. By varying the laser energy, the energy of the particles reaching the substrate can be altered, thus altering the energy that they contain to diffuse along the surface of the substrate. Altering the pressure of the background gas in the deposition chamber alters not only the energy of the particles reaching the surface of the substrate (as described above) but also has a significant effect on the stoichiometry on the thus deposited film. A high background gas pressure by virtue of its physical pressure on the surface of the crystal prevents the reevaporation of oxides from the heated substrate. Especially when depositing films containing volatile oxides, since the vapour pressure of the metal (and thus their tendency to evaporate) decreases in their oxide form, the use of oxygen as a background gas is common. For example, it has been shown that during the deposition of Pb containing oxides, the presence of oxygen as a background gas, promotes the formation of PbO in the plasma, allowing for easier nucleation at the surface [**?**]. Nevertheless, increasing oxygen pressure in the deposition chamber also decreases the deposition rate due to increased energy loss from collisions between the plasma particles and the oxygen molecules, thus demanding an optimal partial pressure for good growth.

The principal advantages of PLD over other deposition techniques include [117] (1) congruent/ stoichiometric transfer of material from the target to the film (2) precise control on the film growth rate and structure quality through control of the laser energy and the repetition frequency (3) flexibility concerning the materials deposited through the process, with recent advances including the use of liquid targets [118]. The simplicity of the technique is, nevertheless, accompanied by certain disadvantages: (1) deterioration of the target surface with time amounting to rapid drop in deposition rates over time, limiting the thickness of the films, (2) homogeneity of films limited to small areas owing to inhomogeneous plume and ablation of a small fraction of the target by the beam.

3.2 Structural Characterisation

3.2.1 Lattice Dynamics Characterisation

3.2.1.1 Inelastic X-Ray Scattering

Inelastic X-Ray Scattering (IXS) employs synchrotron radiation to study and observe the phonon behaviour and dispersion, which in turn allow for the understanding of the atomic dynamics in the crystal lattice. Realised for the first time at the European Synchrotron Radiation Facility (ESRF) [119], this technique proves to be more advantageous than its predecessor, Inelastic Neutron Scattering (INS) [120] since it allows for a higher energy resolution (1.5meV vs. 20meV),provides for access to smaller (μg vs mg) samples, and has minimal background (from smaller attenuation lengths for X-Rays when compared to neutrons).

Through the scattering arising from the interaction of the X-Rays with the vibrational modes present in the sample, the energy of each vibrational mode can be measured. This variation in the energy of the vibrational mode can be studied as a function of the lattice vector in the reciprocal space through a variation in the alignment of the analyser (also referred to as detector) with respect to the sample. Thus, through different alignments of the detector, a mapping of the energy of the vibrational modes present in the sample can be obtained, yielding eventually the phonon dispersion across the Brillouin lattice. The phonon dispersion, in turn, helps understand the lattice dynamics in play, and on studying the variation of the phonon dispersion with temperature, it is possible to understand the mode interactions across the phase transition in certain materials.

3.2.1.2 Thermal Diffused Scattering

The presence of thermally populated phonons in crystals when tested with a synchrotron source results in a loss of intensity of the Bragg Peaks and in a simultaneous scattering of the incoming X-Rays [121]. The latter effect is known as Thermal Diffused Scattering(TDS) and is used in combination with IXS to undertsand the lattice dynamics. A 2-dimensional imaging of the scattered intensities provides a spatial mapping of the population of the phonon modes along different points in the reciprocal lattice. Through the acquisition of these maps along different symmetry axes, a distribution of the phonon modes at different reciprocal lattice points is obtained. Using theoretical simulations to fit the distribution of the phonon modes, the force constants for the vibrations along the different directions are obtained, used consequently to obtain the phonon dispersion along different symmetry axes.

3.2.1.3 Raman spectroscopy

Raman spectroscopy is a spectroscopic technique used to observe the vibrational, translational and rotational modes in a crystalline lattice. It employs the use of a coherent, monochromatic electromagnetic wave source (usually a laser) which is incident on a sample. Through the interaction of the electromagnetic waves with the modes in the crystal, elastic and inelastic scattering processes occur [122]. From the scattered radiations, the elastic part is filtered out and the inelastically scattered radiation is filtered according to its wavelength. The interaction of the incident wavelength with the modes present in the sample can result either in the shift of the vibrational state towards higher energy, resulting in a scattered wave of smaller wavelength (Stokes shift) or in the relaxation of an excited vibrational state towards lower energy yielding a scattered wave of higher wavelength (Antistokes shift). The difference between the wavenumbers (called waveshift) corresponding to the wavelength of the incident beam (λ_0) and the scattered radiation (λ_1) is calculated using Eq. 3.1. The intensity of all scattered radiation is plotted as a function of the waveshift, and the peaks in such a plot correspond to the energies (E, using the Planck's constant (h), see Eq. 3.2) of the various active modes in the sample.

$$\Delta\omega = (\frac{1}{\lambda_0} - \frac{1}{\lambda_1}) \tag{3.1}$$
$$E = h\Delta\omega \tag{3.2}$$

For a sample undergoing a structural phase transition, thus, the Raman spectra obtained from the two different phases would be different owing to difference in the vibrational modes. As is usually the case in most ferroic transitions, the shift from a high symmetry phase to a low symmetry phase also results in the splitting of peaks, owing to lower degeneracy of the modes in the lower symmetry phase. Hence on measuring the Raman spectra as a function of the temperature, by observing the change in the spectra, the phase transition can be studied. Further, since the intensity and the width of the peaks is affected by the presence of impurities, defects and strain, the analyses of these spectra yields important information on the structural aspects of the sample. In the present work, the Raman spectroscopy measurements were carried out at the Laboratoire Structures, Propriétés et Modelisation des Solides (Ecole Centrale, Paris) under the guidance of Dr. Brahim Dkhil.

3.2.2 Macroscopic Structural Characterisation

3.2.2.1 X-Ray Diffraction

X-Ray Diffraction is a non-destructive method for the structural characterisation of materials including phase identification, composition, grain size estimation for ceramics, and determination of preferred orientation, thickness and strain state for thin films. In a typical X-Ray Diffractometer, a collimated beam of monochromatic X-Rays with a wavelength λ is incident on a specimen and due to the crystalline symmetry associated with the material, this beam is diffracted according to Bragg's law (Eq. 3.3)

$$n\lambda \quad = \quad 2d\sin\theta \tag{3.3}$$

where n is the order of diffraction (=1 in this case), θ is the angle between the incident beam and the atomic planes, and d is the interplanar distance (refer Fig. 3.2). The intensity of the diffracted beam is measured as a function of 2θ (the angle between the incident and the diffracted beams), yielding the diffraction spectrum or the diffraction pattern for the sample. This is known as a symmetrical 2θ scan. For a measurement involving a polycrystalline sample, since multiple planes with different interplanar seperations are simultaneously oriented parallel to the sample surface, the diffraction pattern shows multiple peaks representing each lattice plane. Using an universal powder diffraction database, one can then index these peaks, and determine the composition of the sample through comparison of spectra of the possible components. On the other hand, when analysing single crystalline specimens (crystals or
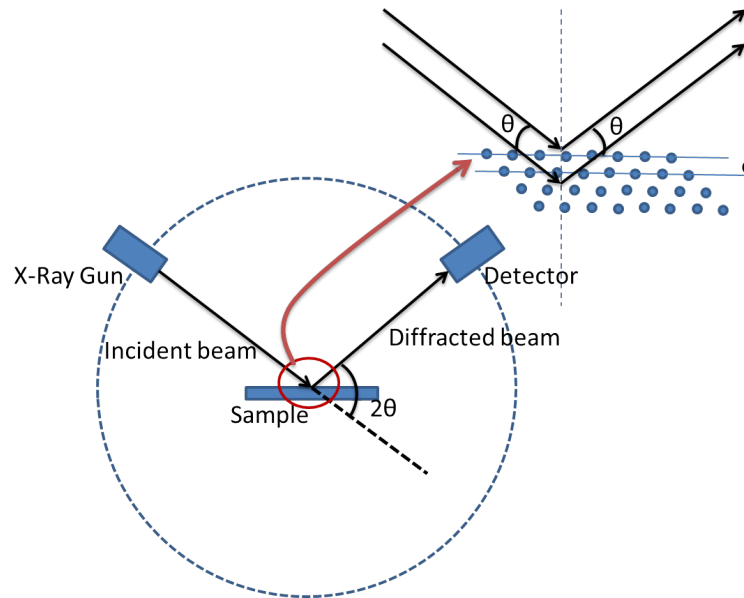
Figure 3.2: Illustration of the X-Ray Diffraction setup showing the symmetry of the experiment as well as the Bragg's law.

epitaxial thin films), given the preferred orientation of only one family of lattice planes parallel to the surface, only a certain set of peaks will be visible in the diffraction pattern, corresponding to the family of these lattice planes. In the case of such samples, an initial knowledge of the composition is obligatory. On knowing the composition of the films, these peaks are indexed by cross-referencing their positions with the powder diffraction database for the same composition.

The diffraction patterns obtained from epitaxial thin films can also often be used to estimate the thickness of the thin film. Owing to their layered nature, The diffracted beams from the top and the bottom of the films interfere, and one observes satellite peaks on either side of the Bragg reflection (known as thickness or Kiessig fringes [123]). Using the position of two such consecutive satellite peaks (at angles θ_1 and θ_2) and the wavelength (λ), the thickness (t) of the thin film can be estimated using Eq. 3.4.

$$t \quad = \quad \frac{\lambda}{2(\sin\theta_1 - \sin\theta_2)} \tag{3.4}$$

In the case of materials that undergo a phase transition at a certain temperature, the change in the structure of the material at the transition is accompanied by either a discontinuity (in the case of a first order phase transition) or a change in the slope (w.r.t. temperature, in the case of a second order phase transition) of the lattice parameter. Hence, by obtaining diffraction

patterns from the material at varying temperatures, through the observation of the change of the lattice spacing, the temperature as well as the nature of the phase transition can be measured.

For thin films, through a precise measurement using a symmetrical 2θ scan as shown in Fig. 3.2, the lattice parameter for the substrate and the film parallel to the surface can be obtained using Eq.3.3. In the case of epitaxial thin films, the difference between these values is used to estimate the epitaxial strain acting on the film along the direction perpendicular to the surface (called the out-of-plane strain). In most cases of epitaxial films though, because of the presence of lattice strain parallel to the surface (called in-plane lattice strain) as well, which is not obtained from conventional 2θ scans. To overcome this limitation, alongside conventional 2-dimensional mapping of the Bragg peaks for thin films, it is also necesarry to map the precise position of the Bragg peaks in 3-dimensional reciprocal space, known as a reciprocal space map. Through this mapping, precise values of the lattice parameter for thin films can be obtained, allowing for an estimation of not only the out-of-plane strain, but also the in-plane strain.

3.2.2.2 Transmission Electron Microscopy

Transmission Electron Microscopy (TEM) is an extremely powerful tool to visualise the microstructure of thin films. Offering atomic resolution for imaging purposes, it renders the visualisation of lattice defects such as dislocations and stacking faults possible. It uses an accelerated electron beam for the imaging operation, with the optical mechanism being comparable to a transmission optical microscope. An electron source replaces the optical lamp, and instead of physical lenses, electromagnetic lenses are used to manipulate the electron beam. For an acceleration of 50kV, the electrons have a wavelength of approximately 5pm, which would technically define the limit of the resolution according to Rayleigh criterion. Nevertheless, owing to the aberrations associated with the lenses, this resolving power is fairly reduced. The working of a TEM is illustrated in Fig. 3.3.

Electrons on striking the sample interact with the nuclei present, and in the case of crystalline samples are diffracted according to Bragg's law (refer Eq. 3.3). The diffracted electrons are transmitted through the sample in the form of coherent beams, and depending on the positioning of the objective aperture, either the diffraction pattern (refer Fig. 3.3(a)) or a magnified image of the sample (refer Fig. 3.3(b)) is recorded on the imaging screen. Contrasts in the image arise from both the amplitude and the phase of the beams leaving the sample. The bright central spot in a diffraction pattern consists of the residual electrons transmitted

through the sample whereas the other spots in the diffraction pattern consist of electrons diffracted through the sample. By using an aperture and limiting only the non-diffracted, transmitted beam to pass through, one obtains what is known as a bright field image, with the image contrast formed on a uniformly bright background. Depending on the diffraction conditions crystalline samples result in an uniform image contrast. Since the diffracted beams are blocked by the objective aperture during bright field imaging, lattice imperfections result in modification of the diffraction conditions, thus changing the diffracted and non-diffracted intensities locally providing for an image contrast. On the other hand, by permitting only one of the diffraction spots to be transmitted through the aperture, the image obtained (called a dark field image) contains the intensity from only those regions in the sample satisfying the diffraction conditions for the given spot. They appear as bright objects on a dark background. This imaging contains information on the lattice planes associated with the diffraction spot chosen and gives more information on the crystallographic orientations in the specimen. With the aperture placed appropriately to allow many diffracted beams, an interaction between these reflections allows for the formation of a phase contrast, resulting in a High Resolution TEM (HRTEM) image, which can yield atomic resolution with appropriate imaging conditions. A schematic of the different imaging conditions for the imaging techniques discussed above are shown in Fig. 3.4 [24].

In addition to the above, the interaction between the electrons and the nuclei results in the release of many other radiations including X-Rays, Bremmstrahlung, fluorescence, and secondary electrons. Among these, the release of characteristic X-Rays is often used for the detemination of the atomic composition of the films through the comparison of the intensities of the X-Rays released by the different atoms present in the sample.

3.2.3 Negative C_s corrected HR-TEM

Interpretation of conventional HRTEM images are limited due to the aberrations effects associated with the objective lens of the microscope. Though the position of heavier metallic atoms is decipherable in these images, the observation of the atomic positions of lighter atoms such as oxygen is cumbersome [125]. The correction of the spherical aberration (C_s) allows for the overcoming of these limitations to a large extent[126]. By using an electromagnetic hexapole/octapole system combined with the other lenses, the C_s as well as the astigmatism may be systematically controlled resulting in the observation of even low atomic number elements such as oxygen. By comparison of the obtained images with simulated images from quantum-mechanical calculations, upto picometer precision can be obtained for the atomic
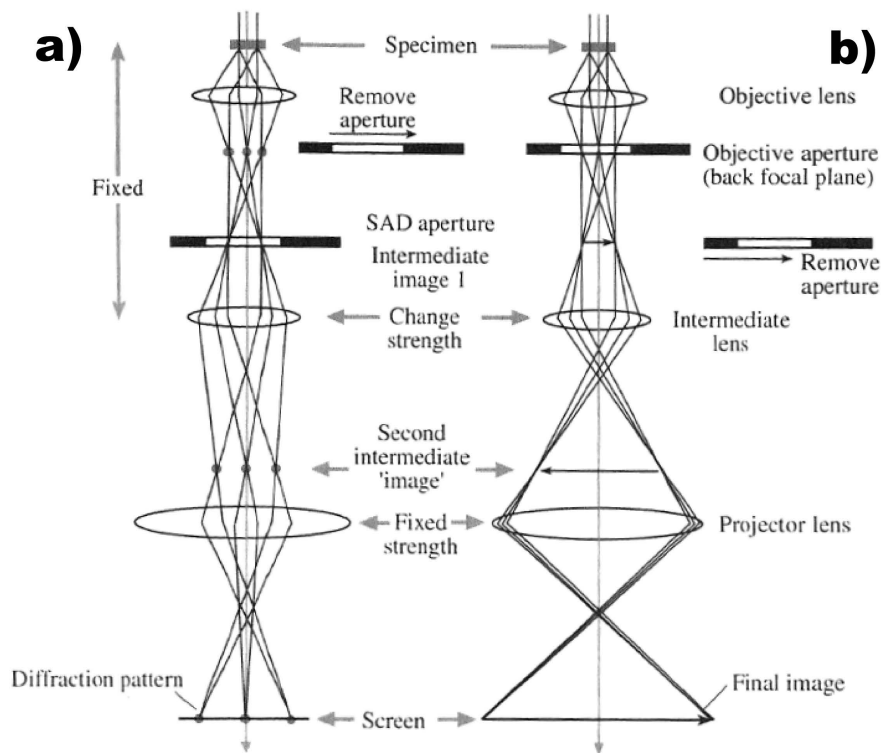
Figure 3.3: Illustration showing the working of a TEM [124] in (a) selected area diffraction (SAD) mode wherein the diffraction pattern is projected onto the imaging screen (b) imaging mode wherein the image from the sample is magnified on to the imaging screen (bright field image). On placing the objective aperture (at the back focal plane) in such a way to allow only one (or a few) spot(s) from the back focal plane to get magnified, a dark field image corresponding to the spots (corresponding to atomic planes) can be obtained.
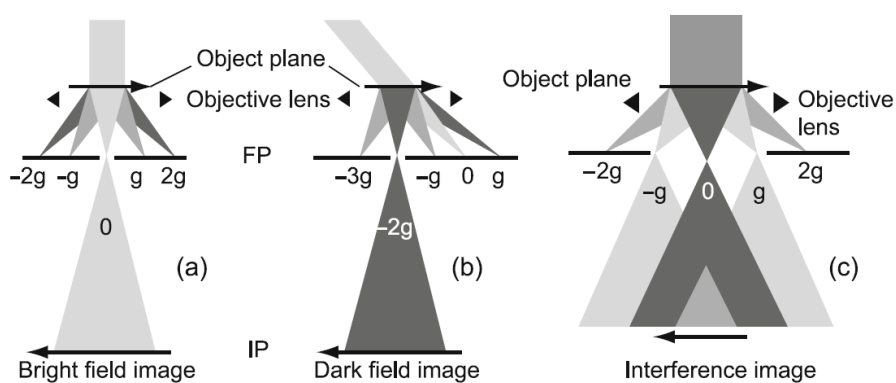
Figure 3.4: The imaging conditions for bright field, dark field, and High Resolution (Interference) TEM techniques. While the non-diffracted, transmitted beam is used for the bright field imaging, dark field imaging uses a single diffraction spot. By using the interference between multiple diffraction spots for interference imaging, atomic resolution can be easily obtained. [24]

positions in the lattice[127]. In the present work, the negative C_s corrected HRTEM studies were carried out at the Ernst-Ruska Center for Microscopy and Spectroscopy with Electrons (Jülich, Germany) by Dr. Xian-Kui Wei under the guidance of Prof. Chunlin Jia.

3.3   Scanning Probe microscopy

Scanning Probe Microscopy (SPM) is a branch of microscopy that employs a physical probe to study various surface properties of materials. Depending on the interactions measured between the probe and the sample, multiple surface properties can be measured simultaneously. The lateral resolution of the images depends on the mode of interaction as well as the mechanics related to the movement of the scanning probe, but with the advent of piezoelectric actuators, the limit for the lateral as well as the vertical resolution in the images has been pushed to the nanometer regime, with the latter being capable of providing very often even atomic resolution.

3.3.1   Atomic force microscopy

An Atomic Force Microscope (AFM) probes the surface of the sample through the atomic interactions between the cantilever and the tip. A sharp tip fixed to the end of a flexible cantilever is made to approach the sample surface and when the distance between the tip and the sample is small enough, the van der Waals forces between the tip and the sample surface become significant (see Fig. 3.5 (b)) and the tip gets attracted further towards the sample. When pushed even closer to the surface, this interaction force becomes repulsive, implying that instead of the tip approaching the surface any further, the cantilever bends to resist this motion. In addition to the van der Waals forces, in an ambient atmosphere, the presence of water molecules on the surface exerts a capillary force on the tip. Thus, when the tip scans across the surface of the sample at a constant height of a few angstroms from the surface (called contact mode), it experiences repulsive or attractive forces depending on the roughness (and hence the seperation between the sample and the tip) of the sample, leading to a distortion of the cantilever holding the tip. A laser reflected off the back of the cantilever measures these distortions through a photo-detector, which is later interpreted in terms of the roughness of the sample. One of the disadvantages associated with this mode of imaging is the wearing out of the tip with subsequent scans owing to the friction between the tip and the surface, as well as potential damage incurred by delicate samples from the force of the AFM tip.
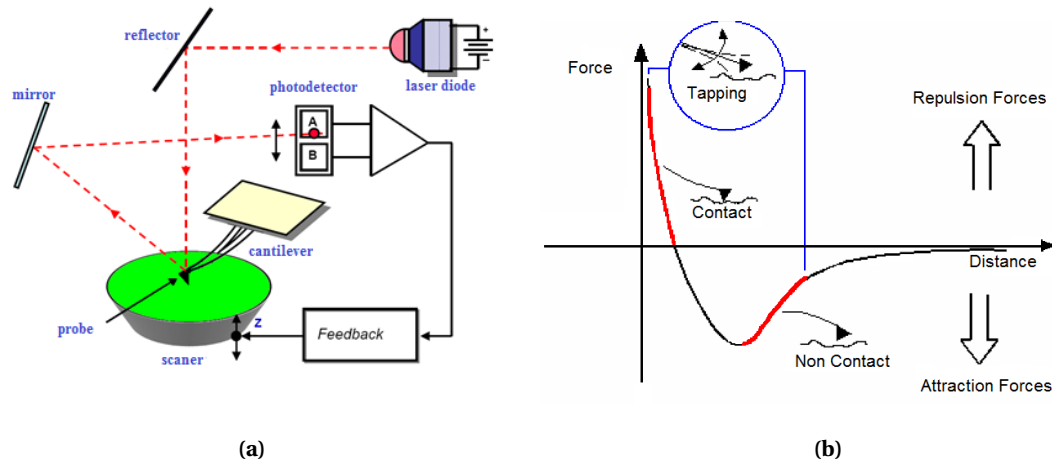
Figure 3.5: (a) Construction of the Atomic Force Microscope. (b) Van der Waals forces from the tip-sample interaction as a function of the tip-sample seperation. [128]

In order to avoid these surface damages, it is possible to operate the AFM from a few nm above the surface of the sample, called tapping mode. In this mode, the cantilever vibrates at its resonant frequency (typically 100-400 kHz) with an amplitude such that it just about touches the surface at the point of highest deflection. On scanning the sample using this vibrating probe, changes in the vibrating frequency and amplitude are mapped spatially, which contains information on the tip-sample seperation, or in other words, the surface topography.

3.4 Macroscopic Dielectric Measurements

The following techniques were employed to analyse the dielectric responses from the thin films to confirm their antiferroelectric nature, and to estimate the phase transition temperature between the antiferroelectric and paraelectric phases.

3.4.1 Small signal capacitance vs. field measurement

Owing to the dielectric nature of the ferroelectric film, the film acts as a capacitor whose permittivity and loss behaviour (through the phase lag and leakage current) may be estimated through its response to an external field. Small signal capacitance vs. field (*C-E*) and loss tangent tanδ measurements yield important parameters of ferroelectric capacitors, with additional information on the reversible parts of the polarisation and the switching process being accessible [129]. A typical excitation signal used for such measurements is shown in Fig 3.6 (a). The reading bias consists of a series of unipolar excitation signal pulses, which
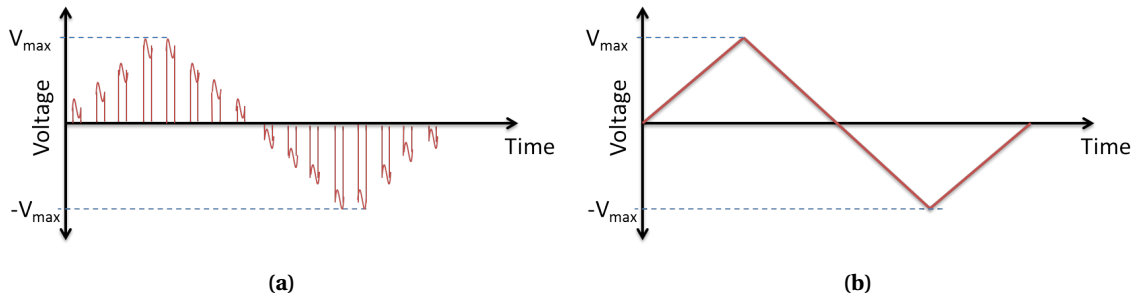
Figure 3.6: Excitation signal for (a) small-signal measurements used in measuring capacitance vs. field analyses. (b) large signal measurements used in the polarisation vs. field analyses.

are DC pulses, with an added sine AC wave superimposed. The DC bias starts at zero and goes to the positive value of the maximum amplitude defined (usually above the coercive field) and then descends to the negative value of the maximum amplitude, before rising back to zero. In this manner, it covers the whole hysteresis. At each point, the capacitance (and hence the permittivity and the loss tangent) are derived from the AC small signal. In this study, the permittivity and the loss was measured using an *HP 4284A LCR meter* connected to the thin films through probes connected to the top and bottom electrodes deposited of the film. The samples were heated in a mini furnace and the C-E measurements were carried out as a function of temperature.

3.4.2   Polarisation vs. field measurement

The polarisation vs. field responses of the thin films are obtained using the dynamic hysteresis measurement. In the case of low leakage current and trapped charges in the film, the current response of a thin film corresponding to an external applied voltage is measured, and the integration of the measured current yields the polarisation. The calculation of polarisation as a function of the applied electric field yields the hysteresis response according to the material being analysed. The voltage excitation signal used to measure the dynamic hysteresis is shown in Fig. 3.6(b). The measurements for the current study were undertaken using the AIXACCT TF2000E setup. The current flowing through the circuit on the variation of the bias applied to the capacitor is measured through a current amplifier and is integrated to obtain the polarisation. The curves measured in this fashion are dependant on the sample history as well as the measurement technique. Hence, the shape and the symmetry of the curves change with frequency, amplitude as well as the number of cycles. Special attention is given to this factor during the analysis of the data.

3.4.3 Permittivity vs. Temperature measurement

The measurement of the permittivity as a function of the temperature is among the most common tools to observe the phase transition in ferroelectric systems. The measurement of the real and imaginary parts of the permittivity at various frequencies, also reveals additional information on the dielectric properties of the material. For example, through the measurement of the imaginary component of the permittivity as a function of the frequency (and their variation with temperature) the conduction mechanisms active in the thin films may be deciphered. The measurements in the current study were conducted using an *HP 4284A LCR meter* connected to the thin films through a probe tip polished to have a tip radius smaller than the size of the top electrodes deposited on the film. The samples were heated in a mini furnace, and the temperature was controlled using an external thermocouple placed near the saphhire holder containing the sample. A bias of 1V was applied with a frequency of 1kHz for measuring the permittivity.

4 Antiferroelectricity in PbZrO$_3$

The complex interactions between the competing instabilities in PbZrO$_3$ have been understood only partially due to a lack of information on the lattice dynamics outside of the Brillouin zone center. In the current chapter, using X-Ray and visible light scattering techniques, the lattice dynamics above the phase transition are observed, shedding light on the exact nature of the interactions between the various instabilities. Using attractive and repulsive biquadratic couplings to describe the observed phenomena, a scenario for the phase transition in PbZrO$_3$ has been provided. Alongside, the origin of the antiferroelectricity in PbZrO$_3$ and its typical characteristics have also been explained using the same model.

The characteristics of the phase transition in PbZrO$_3$ have been previously explained in Section 2.1.2, and it has been established that such a phase transition would require the almost simultaneous condensation of three instabilities associated with the Γ, Σ and the R points of the first brillouin zone, statistically a rather improbable event. The interactions between these instabilities remain unexplored, and resolving this absence of information could explain the origin of antiferroelectric behaviour in PbZrO$_3$. Since the instabilities lie outside the zone center, direct ways to measure the generalized susceptibility away from the Brillouin zone center include neutron and X-ray inelastic scattering. Some qualitative information can also be extracted from energy-integrated diffuse scattering experiments. The critical dynamics in PbZrO$_3$ as evidenced by complementary use of inelastic X-ray scattering, diffuse X-ray scattering and Brillouin light scattering techniques have been analysed.

4.1 Dynamics of the phase transition

The following scenario was proposed by Prof. Alexander K. Tagantsev for the phase transition in PbZrO$_3$ considering the interactions between the multiple instabilities. The ferroelectric mode or the transverse optic (TO) mode is coupled with the transverse acoustic phonon (TA) mode through a repulsive biquadratic coupling along the [110] reciprocal direction in the cubic phase. On approaching the phase transition from the high temperature phase, the ferroelectric mode softens at the Γ point, resulting in its lowering. Through its repulsive biquadratic coupling, this results in the lowering of the branch of the TA mode along the [110] direction. At this point, the system is very close to an incommensurate instability, which is avoided through the onset of a first order phase transition to a commensurate phase corresponding to the Σ point. The appearance of this first order phase transition prevents further lowering of the TA mode, which correspondingly (through the repulsive biquadratic coupling with the TO mode), prevents further softening of the TO mode, causing the ferroelectric transition to be avoided. Meanwhile, the condensation at the Σ point causes the onset of the oxygen octahedral rotations through an attractive biquadratic coupling, described by the Holakovsky mechanism [130]. In the following sections, each of the features of the claimed scenario will be substantiated.
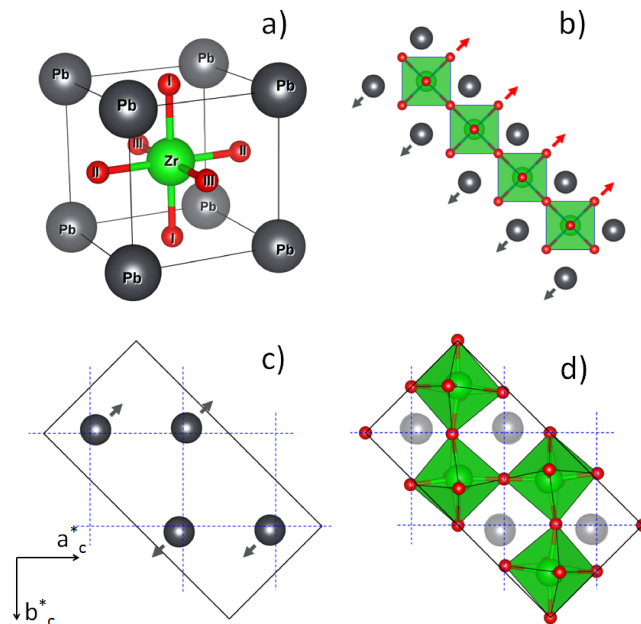
Figure 4.1: Unit cell of lead zirconate in the cubic phase (a), and lattice modes relevant to its antiferroelectric behavior: (b) the Γ -point polar mode controlling the dielectric anomaly (shown schematically for one of the possible orientations of its dipole moment); (c) lead displacements in the Σ -mode; (d) oxygen-octahedron rotations in the *R* -mode. Directions of the cubic crystallographic axes in the *ab* plane are shown. In c) and d), the projections of the orthorhombic unit cell onto the *ab* plane are shown.
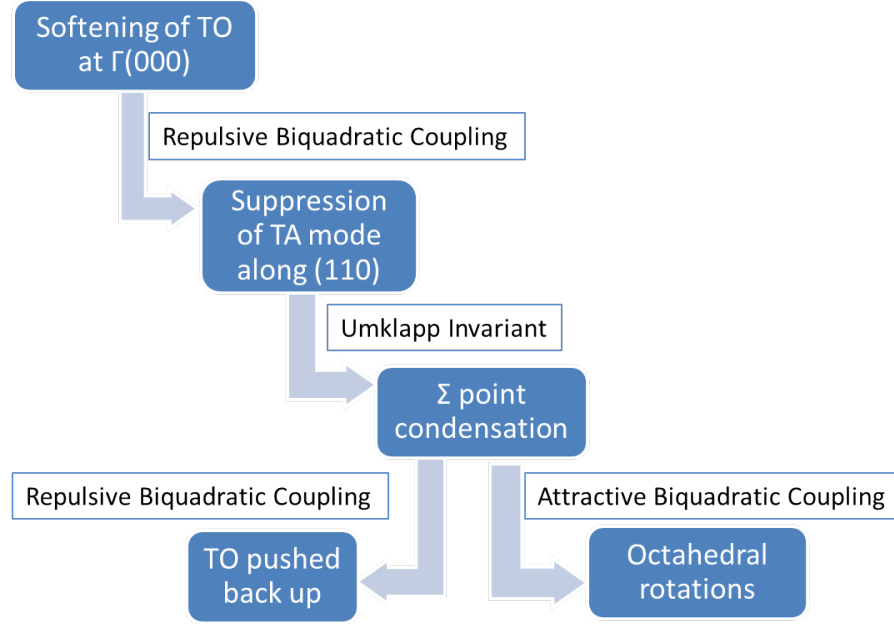
Figure 4.2: Schematic explaining the phase transition in PbZrO$_3$

4.2 Phonon dispersion from X-Ray Scattering

4.2.1 Experimental Construction and Details

For the current study, the experiments were conducted at BL35XU high-resolution IXS beam-line of the SPring-8 synchrotron radiation source in Hyogo prefecture, Japan. A Si (11 11 11) monochromator was used, giving 1.5meV full width at half maximum resolution. X-Rays scattered by the sample were analysed by 12 analysers, providing information for 12 values of the scattering vector. Experimentally measured spectra were fitted using the least-square technique to a sum of phonon resonances approximated by the damped harmonic osciliator lineshape convoluted with experimental resolution and Lorentzian-shaped quasi-elastic peak at zero transmitted energy.

The inelastic structure factor for a one-phonon scattering event with a momentum transfer ($\vec{Q}$) with a jth mode is given by the following sum over all the atoms (a) of the unit cell

$$F_{jn}(\vec{Q}) = \left| \sum_a \frac{f_a(\vec{Q})}{\sqrt{M_a}} [\vec{e}_a^j(\vec{q}) \cdot \vec{Q}] \exp(i\vec{Q} \cdot \vec{r}_a) \exp(-w_a) \right|^2 . \tag{4.1}$$

43

where n is the Bose factor, M_a represents masses of the ions, $f_a(\vec{Q})$ - the atomic scattering form factors, $\vec{e}_a^j(\vec{q})$ - the mode eigenvector (or the polarisation vector), $\vec{r}_a$ - positions of the atoms in the unit cell and $\exp(-w_a)$ - the Debye-Waller factor. The key factor for deciding the experimental geometry lies in the term $\vec{e}_a^j(\vec{q}) \cdot \vec{Q}$, where $\vec{Q} = \vec{\tau} + \vec{q}$ with $\vec{\tau}$ the nearest reciprocal lattice vector and $\vec{q}$ the scattering vector. Given the position of the special point Σ on the [110] direction of the reciprocal lattice, special attention is given to $\vec{q}$ oriented along [110]. Transverse modes propogating along this direction have two polarisation vectors corresponding to $\vec{e} = [1\bar{1}0]$ (for the in-plane polarisation) and $\vec{e} = [001]$ (corresponding to the out of plane polarisation). For the observation of the in-plane polarised transverse modes, a lattice point ($\vec{\tau}$) of the form [h h 0] would be ideal because of the large value of the product $\vec{e}_a^j(\vec{q}) \cdot \vec{Q}$ and the minimal scattering from the longitudinal modes along this direction. But this advantage is limited by the high strength of the acoustic reflections from these points (strong reflections (hkl) in the cubic phase are given by h+k+l=even), potentially disturbing the observation of the optic mode. It is hence preferable to choose other lattice points to observe the optic mode more distinctly, at the cost of some interference from the longitudinal modes. Thus, to ensure minimal contribution from the longitudinal modes while avoiding strong reflections, the reciprocal lattice point (320) is chosen for $\vec{\tau}$. In this experiment particularly, special attention is given to $\vec{q}$ oriented in the [110] direction, for polarisations oriented along [1-10]. Additionally, phonons at and around R-point, and out-of-plane polarised TA mode along the [110] were studied carefully around the reciprocal lattice point $\vec{\tau} = (300)$. For maximising the intensity of the in-plane polarised TA mode at these points (corresponding to a high value of the factor $\vec{e}_a^j(\vec{q}) \cdot \vec{Q}$), for the former a scattering vector $\vec{q}$ along the [111] direction was used, while for the latter $\vec{q}$ was aligned along [011].

4.2.2 Phonon Dispersion

Figure 4.3 shows the spectra corresponding to the $\vec{q}$ along the Γ-M line, measured in a way that mostly the transverse in-plane polarized phonons are visible. The spectra cover the range of points from $\vec{q} = (0.1\ 0.1\ 0)$ through Σ (1/4 1/4 0) to M (1/2 1/2 0) point. The spectra contain two pairs of phonon resonances and the central peak. Phonon resonances were fitted to damped harmonic oscillators lineshape function convoluted with the experimental resolution. The low energy phonon resonances can be associated with the transverse acoustic (TA) branch.

The spectra in Fig. 4.3 show a distinct temperature dependence both in the TA phonon frequency and in the intensity of the central peak. At low q values close to the transition temperature the TA phonon resonance and the central peak become poorly distinguishable.
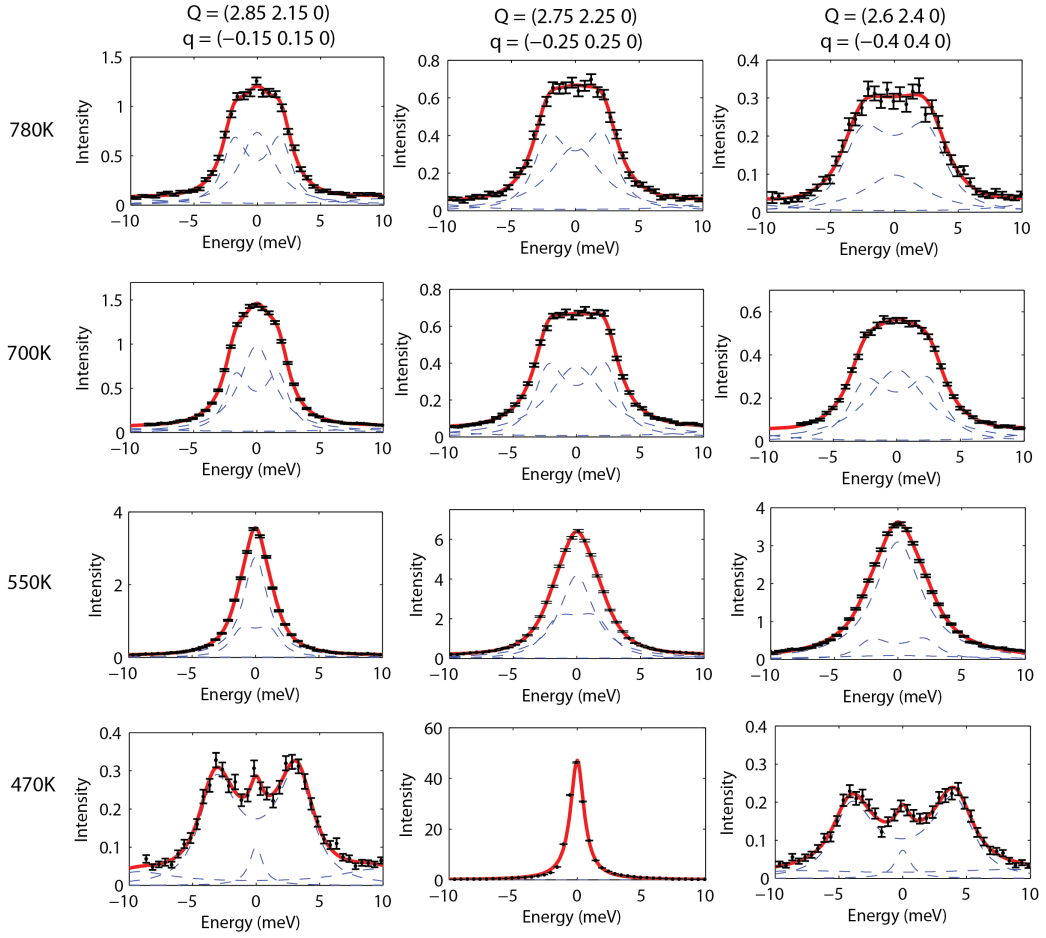
Figure 4.3: Temperature evolution of the IXS spectra along Γ-M direction. The figures are arranged in the matrix with different columns corresponding to different q values and different rows to different temperatures. Dashed lines define the fit by the sum of 2 damped harmonic oscillator (DHO) and the central peak. At T=470 K, q=(0.25 0.25 0) the huge peak is observed due to formation of the superstructure.

Nevertheless in a broad $T - q$ range they can be reliably analyzed separately. Figure 4.4 shows the phonon dispersion curves for the in-plane polarized TA and TO modes. Already at q =0.1 the TA phonon frequencies both at 780 K and 550 K are much lower than the value extrapolated from the sound velocity determined at 550 K (see below, Fig. 4.7). For the q-range from 0.1 to 0.5 the TA mode at 780 K and at 550 K has close to linear dispersion and the dispersion softens when temperature decreases. For $\vec{q}$=(0.1 0.1 0) the decrease is of about 40% from T=780 K to T=550 K. At T=550 K the phonon energy at Σ-point in PbZrO$_3$ is about 2 meV. Below the transition temperature (see T=470 K in Fig. 4.3) the values of the in-plane TA phonon energy are recovered to about 4–5 meV, which is typical for the lead based perovskites. This can be seen in the bottom row of Fig. 4.3 which shows the same Γ-M direction but below the transition temperature. One may note the appearance of the Σ-point superstructure in that
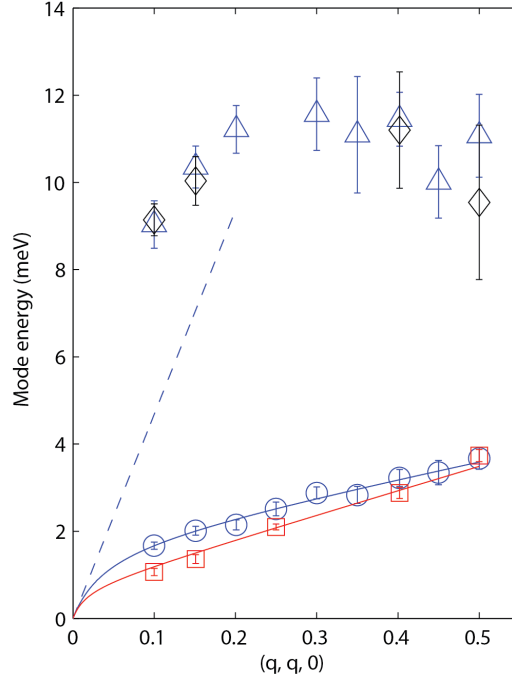
Figure 4.4: Dispersion of the TA and TO phonons, propagating in Σ direction ($\vec{q} = (q, q, 0)$) of the reciprocal space and polarized in (0 0 1) plane: circles – TA at 780 K, squares – TA at 550 K, triangles – TO at 780 K, diamonds – TO at 470 K (X-ray scattering data). Error bars correspond to 95% confidence interval. The dashed line indicates the slope of the dispersion curves in the vicinity of the Γ point, extracted from Brillouin light scattering data.

row (Fig. corresponding to $\vec{q}$=(0.25 0.25 0) at 470K, note the difference in the intensity scale). The central peak, which is not related to the superstructure, is strongly suppressed below T$_c$.

The anomalously low frequency of the TA phonon is seen only for in-plane polarized TA phonons propagating in Γ-M direction. Owing to the simultaneous measurement of multiple points in the Brillouin zone around the original q of interest from the 12 point detector system, it was possible to obtain the phonon resonances at points deviating slightly from the Γ-M direction. A mapping of the phonon resonances on these points allows for the visualisation of a phonon dispersion surface, and not just a phonon dispersion curve, as seen in Fig. 4.5 for the dispersion of the in-plane polarised TA mode in the (001) plane. It is evident that once the wavevector deviates from the Γ-M direction the dispersion starts to appear more 'usual', thus implying a strongly anisotropic in-plane polarised TA mode. The IXS spectra for q along [110] and q deviating from this direction are shown in Fig. 4.6 (a) and (b). The length of q is nearly the same for different plots in the figure. It is clearly seen that moving away from the 'soft' [110] direction results both in increase of the phonon frequency and suppression of the central peak (Fig. 4.6(b)).
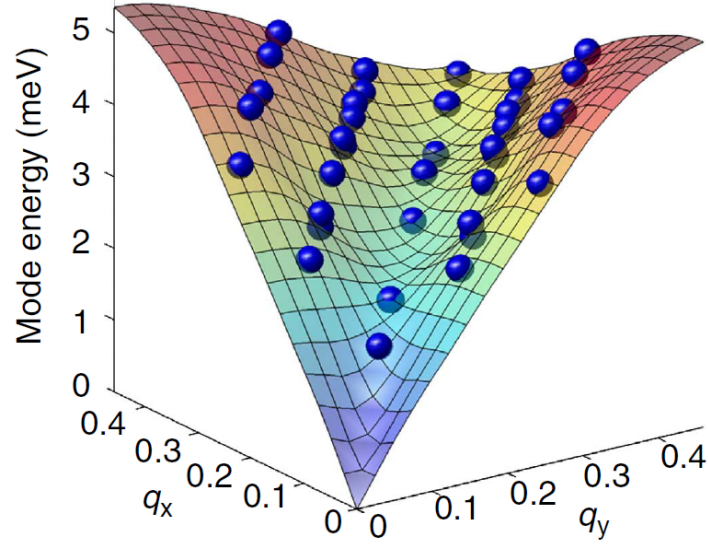
Figure 4.5: Dispersion surface for the lowest TA phonons propagating and polarised in the (001) lattice plane at 780K. The wave vectors are measured in the units of the reciprocal cubic lattice constant. The presence of a 'valley' along the Σ direction points to the anisotropy of the in-plane polarised TA mode.

Normally-high energy is observed for the out-of-plane polarised phonons, even along Γ-M direction (Fig. 4.6(c)). The high-energy phonon resonances, observed in the spectra of Figs. 4.3 and 4.6 and corresponding to the transverse optic (TO) mode, do not show any temperature dependence. Figure 4.4 shows the dispersion of the TO phonon resonance for the temperatures $T = 780$ K and $T = 470$ K (below the transition). Obviously the data points above and below the transition correspond to the same curve within the precision of error bars. Due to the resolution limitations, only the TA resonances with q-vector magnitude above or equal to 0.1 r.l.u. were observed and these data give the dispersion relations depicted by data points in Fig. 4.4. On the other hand, at small q the TA branch has a dispersion of linear form $\omega_{TA} = Cq$, where the constant C depends on the direction and is determined by the elastic tensor of the crystal. Brillouin light scattering was used to determine the initial slopes of the dispersion curves for the acoustic branches. The temperature dependences of the speed of sound for the TA phonons propagating in [1 0 0] and [1 1 0] directions are shown in Fig. 4.7. There is about 14% decrease in the speed of sound for the TA phonons propagating in [1 1 0] direction on cooling from approximately 660 K to the transition temperature, while for [1 0 0] direction the speed of sound does not change notably. This decrease is attributed to the effect of electrostrictive interaction between the squared order parameter and the strain caused by the acoustic waves[131]. It is instructive to note that at high temperatures the crystal appears to be highly isotropic with regard to the initial slope of transverse phonons: the values of speed of sound along [1 0 0] and [1 1 0] are nearly identical. This means that the TA phonons in Γ-X
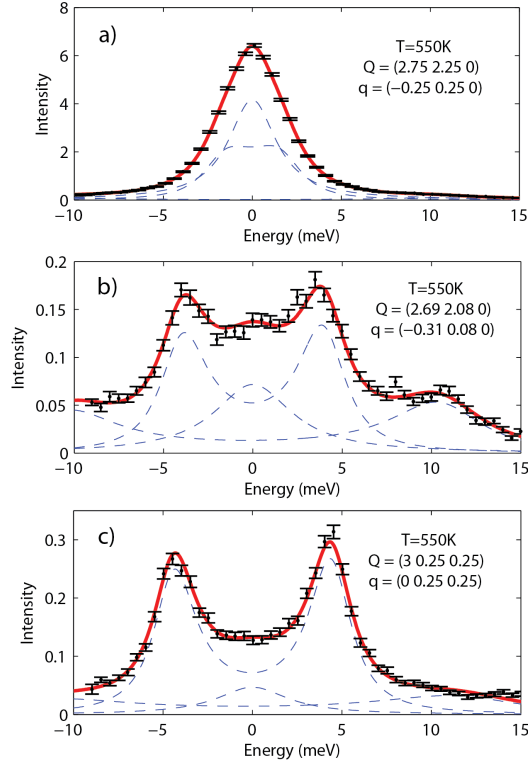
Figure 4.6: IXS spectra at T=550 K (E – Energy transfer in meV) for different directions of the reduced wavevector $\vec{q}$ and contributing polarization $\vec{e}$ given by the scalar product $\vec{e} \cdot (\vec{\tau} + \vec{q})$ (see Eq. 4.1). (a) $\vec{q}$ along [1 1 0] at τ= [3 2 0] and $\vec{e}$= [1 -1 0]; (b) $\vec{q}$ aside of [1 1 0] direction at τ= [3 2 0] and $\vec{e}$ in H K 0 plane; (c) $\vec{q}$ along [0 1 1] at τ= [3 0 0] and $\vec{e}$= [1 0 0] direction (neglecting longitudinal contribution along [0 1 1] and in-plane contribution along [0 1 -1]).
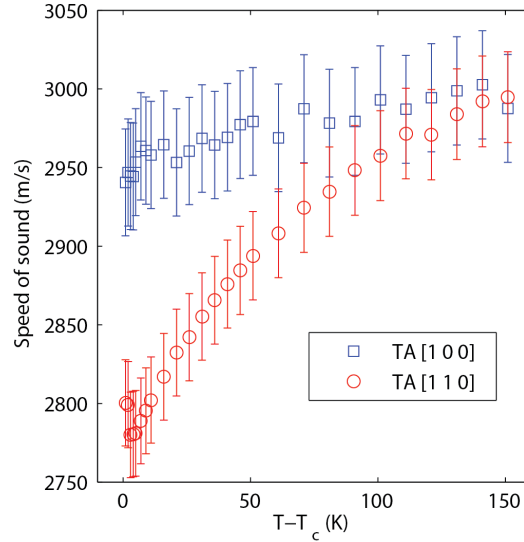
Figure 4.7: Temperature dependence above the antiferroelectric phase transition of the speed of sound for the TA phonons in PbZrO$_3$ determined by the Brillouin light scattering. TA [1 0 0] indicates the TA phonons propagating along the [1 0 0] direction polarized in the (1 0 0) plane, while TA[1 1 0] denotes the TA phonons propagating along the [1 1 0] direction polarized along [1 -1 0] direction.

and Γ-M directions have the same dispersion close to the Γ-point, making the huge anisotropy in TA dispersion at high temperatures and at higher q-values especially remarkable.

4.2.3 Central peak and flexoelectric mode coupling

As seen from the results presented in the previous section the observed TO mode resonance is practically temperature independent and cannot be considered as the origin of the increase of the dielectric permittivity. Instead of the mode softening we see the growth of the central peak (CP). Ostapchuk et al. [48] observed in the IR absorption spectra a similar feature - an independent critical 'central mode' responsible for the dielectric anomaly. However it is well established that the critical growth of the CP is not necessarily related to an additional degree of freedom critically slowing down but can result from the coupling of the soft mode with an intrinsically temperature independent degree of freedom. Such approach was developed during the last 40 years and is widely discussed in the literature [132–135].

Incidentally, the temperature dependence of the central peak intensity is seen to be consistent with the assumed critical decrease of the ω_0 frequency of the ferroelectric soft mode. Figure 4.8 shows the fit of the experimental data to the formula [134]

$$I^{\text{crit}}(q, T) = \frac{T}{T - T_0 + g q^2}. \tag{4.2}$$

This formula describes the expected temperature dependence of the central peak intensity due to the condensation of the soft mode with critical temperature $T_0 = 485$ K [27]. Parameter g is connected to the correlation length and treated as a constant. Thus the central peak is indeed a signature of the PbZrO$_3$'s ferroelectric lattice instability that is reflected by the dielectric anomaly, i.e. the central peak attests to the softening of the ferroelectric mode at the Γ point on approaching the Curie temperature T$_o$. Rattling motion of the Pb^{2+} ions in the multi-well potential can be tentatively considered as the microscopic realization of the slow relaxing degree of freedom. This rattling is not the origin of the phase transition but strongly renormalizes the critical dynamics.

The temperature independant TO mode (manifesting as the temperature dependant central peak in the IXS observations) and the heavily temperature dependant TA mode, are inter-connected. Previously, the TA-TO mode coupling was identified as the source of "pushing down" of the TA mode in KTaO$_3$ [136] and other crystals with ferroelectric soft modes. Since the piezoelectric coupling is forbidden by symmetry in the paraelectric phase, the interaction between TA and TO modes in PbZrO$_3$ is described not by bilinear coupling of polarization and
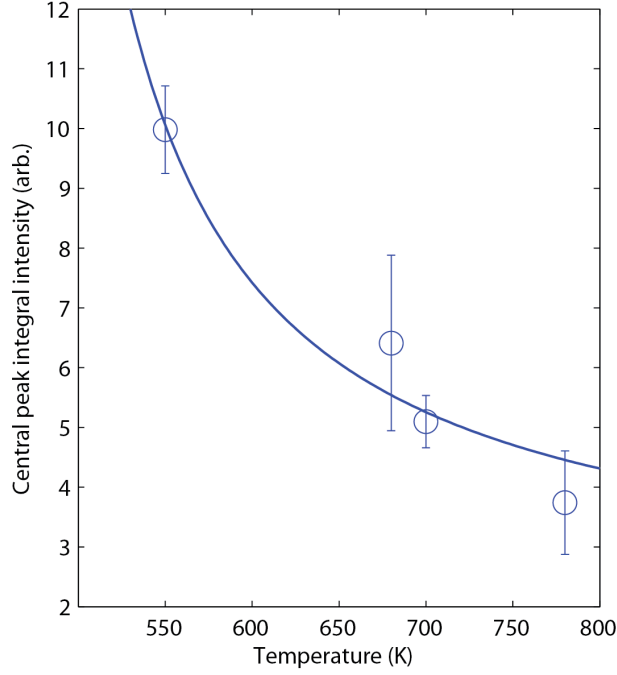
Figure 4.8: Temperature dependence of the central peak integral intensity. The dependence corresponds to the the momentum transfer $\vec{Q}$=(2.15 2.85 0) (reduced scattered wavevector $\vec{q}$=(0.15 -0.15 0)). Error bars correspond to 95% confidence interval. Fit to Eq. (4.2) is shown as solid line.

deformation but by gradient terms involving these quantities in the free energy expansion. The latter (F) reads

$$F = \frac{\alpha}{2}P^2 + \frac{c_{ijkl}}{2}u_{ij}u_{kl} + \frac{g_{ijkl}}{2}\frac{\partial P_i}{\partial x_j}\frac{\partial P_k}{\partial x_l} - \frac{f_{ijkl}}{2}\left(P_k\frac{\partial u_{ij}}{\partial x_l} - u_{ij}\frac{\partial P_k}{\partial x_l}\right) \tag{4.3}$$

where $\alpha = A(T - T_0)$, P_i - components of the polarization vector, c_{ijkl} are the stiffness coefficients, g_{ijkl} are the correlation energy coefficients and u_{ij} - components of the elastic strain tensor. Hereafter the Einstein summation convention is adopted. The flexoelectric tensor f_{ijkl} describes the interaction between polarization and gradient of deformation and the interaction between gradient of polarization and deformation. The flexoelectric coupling works only at finite wavevectors q, leaving the initial slope of the elastic waves dispersion intact. The effect of this coupling on the finite-q phonon spectrum is a "repulsion" between the frequencies of the TA and TO modes.

4.3 Thermal Diffused Scattering

When compared to PbTiO$_3$ and KTaO$_3$ where the soft mode presents itself as a temperature-traceable phonon-type excitation[135, 137], PbZrO$_3$ presents a much more complicated dynamical response for the soft mode through the appearance of the central peak, resulting in a relaxation type excitation and making it difficult to trace the spectral evolution of the soft mode. At the same time, the accuracy of the IXS experiment does not suffice for the evaluation of the parameters required to elaborate the 'flexoelectric scenario' previously described. A flexoelectric coupling should, nevertheless, result in a specific correlation pattern of thermal atomic displacements, and to confirm this coupling, X-Ray Diffused Scattering experiments were undertaken.

4.3.1 Experimental Details

The diffused scattering measurements for the current study were carried out using general purpose KUMA6 diffractometer at BM01A Swiss-Norwegian Beamline of ESRF. A sagitally focussing Si (1 1 1) monochromator was used, and wavelength λ=0.99A was selected and calibrated with a NIST LaB$_6$ standard. Diffraction patterns were recorded using a MAR345 detector. All the measurements were performed on a parallelepipedon shaped single crystal mounted on a goniometer heated by a flow of hot nitrogen. The temperature was regulated with a stability of 0.5K. Three dimensional reconstructions of the scattering intensity in reciprocal space and two-dimensional cross-sections of these reconstructions were performed using Volvox program.

4.3.2 Results and Discussion

The intensity of integral diffuse scattering due to the 3 acoustic modes (2TA + LA) and the 2 lowest energy transverse optic modes (2TO) is given by

$$I(\mathbf{Q}) \propto T \sum_{i=1}^{5} \sum_{l=1}^{2} \frac{1}{\omega_i^2(\mathbf{q})} |\mathbf{Q} \cdot \mathbf{w}^{(i,l)}(q)|^2. \tag{4.4}$$

Here $\omega_i(\mathbf{q})$ are the frequencies of the renormalized phonon modes, $i = 1..5$ enumerates the eigenmodes and $l = 1, 2$ specifies the Cartesian components of the contributions from the unperturbed optic ("1") and acoustic ("2") modes. The data from the diffuse scattering experiments were fitted to a lattice dynamics model incorporating the flexoelectric coupling [136, 138]. Figure 4.9 shows the experimental data and the fit for the six two-dimensional

cross-sections of the diffuse scattering intensity maps around the (0 0 -2) and the (0 1 -2) reciprocal space points. A very good qualitative agreement between the experimental and the simulated cross sections is provided with the model that takes into account the flexoelectric coupling, whereas without this coupling, the specific features of the diffuse scattering maps cannot be reproduced. This confirms that the softening of the optical mode acts as the driving force, through the flexoelectric coupling, for the subdued form of the anomalous transverse acoustic mode.

4.4   Modulation Instability and Missed Incommensurate Phase

The presence of the flexoelectric term in the free energy expansion (4.3) makes the system potentially unstable with respect to spatial modulations of polarization and strain. The criterion for the appearance of such instability, formulated in terms of phonon eigenstates, was proposed by Axe *et al* [135]. These authors also supposed that "the materials exhibiting such instability existed or would be found". The fact that the apparent "pushing down", or renormalizing of the TA mode in PbZrO$_3$ is much more pronounced than in other studied systems suggests that it could be the prime candidate in the search for materials where the modulation instability "would be found". Triggering of such instability would happen if the TA branch would touch (in the case of the second order transition) or "almost touch" (in the case of the first order transition) the zero energy level at some q-point along the $\Gamma - \Sigma$ direction. In this case the newly formed modulated phase should be characterized by the same or similar ionic displacements as would have a frozen renormalized TA phonon in the corresponding q-point. And indeed, the AFE phase of PbZrO$_3$ has the pattern of the lead displacements consistent with the scenario in which it is formed as the result of the TA mode condensation at $q = q_\Sigma$ (the 'lock-in' phase corresponding to the incommensurate instability in its vicinity). This pattern corresponds to the so-called Σ_3 normal mode of the cubic structure [30, 139].

For cubic (perovskite) materials the modulation instability criterion (i.e. the criterion for the formation of an incommensurate phase) can be readily rewritten in terms of the c, g, and f tensors. For the modulations along the [1 1 0] direction there are two such formulations possible depending on the polarization vector [140]. For the in-plane polarization (along [1 -1 0]) the criterion reads

$$\Theta_1 = (f_{11} - f_{12})/\sqrt{(c_{11} - c_{12})(g_{11} - g_{12})} \qquad (4.5)$$
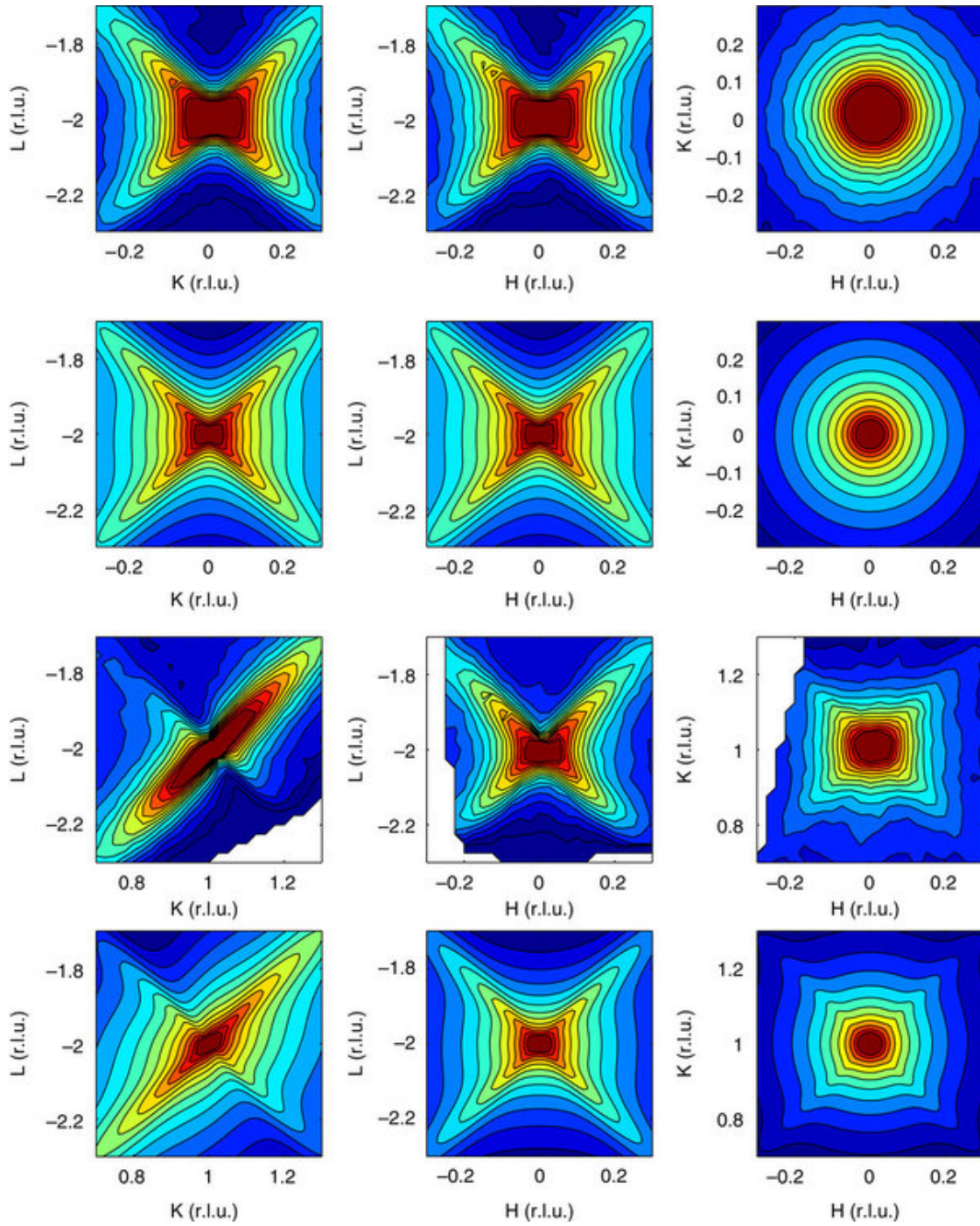
Figure 4.9: Distributions of the diffuse scattering intensity at 550K. Rows 1 and 3 correspond to the experimental maps, and rows 2 and 4 show corresponding calculations. Taking into account the flexoelectric coupling in these simulations enables a good qualitative description of the peculiar shapes of these maps.

while for the out-of-plane polarization (along [0 0 1]) it is

$$\Theta_2 = f_{44}/\sqrt{c_{44}g_{44}}; \tag{4.6}$$

where f_{ii} stands for the flexoelectric coefficients, g_{ii} for the correlation coefficients and c_{ii} for the stiffness coefficients. The values of the parameters θ_1 and θ_2 if greater than 1, would imply a potential incommensurate instability. It is possible to estimate the parameter Θ_1 from Eq. 4.5 for PbZrO$_3$ from the parameters previously used in the simulation of the intensity maps. Using these values, an estimated value of $\Theta_1 = 0.9$ is obtained, which is close to the critical value of 1 as determined previously [140]. It is thus clear that PbZrO$_3$ is not far from the incommensurate instability.

Instead, what one observes is that the transition is of the first order, the modulation vector is $\vec{q} = \vec{q}_\Sigma$ and the TA branch is softening as a whole, without any point on it being special. Consequently one needs to find a mechanism by which the modulation with this particular commensurate wavevector occurs instead of modulations with the arbitrarily close incommensurate variants. In systems with real incommensurate phases it often happens that the generally incommensurate modulation is pinned down to the particular commensurate wavevector. The terms in the free energy expansion responsible for this effect are called Umklapp terms [134].

In order to elaborate, the description of the scenario with the formation of an incommensurate phase with a wave vector parallel to the [1 1 0] direction, having an absolute value k_0 is considered. An order parameter A$_k$ corresponding to the low-lying acoustic mode for a wave vector k parallel to this direction is evoked, and atomic displacements corresponding to this modulated structure are proportional to the real part of the complex wave

$$\xi_k \quad = \quad A_k e^{ikx} \tag{4.7}$$

For any k, the contribution of this order parameter to the free energy can be written as follows [134]

$$F_{\mathrm{k}} = \frac{\alpha_k(T)}{2}|A_k|^2 + \frac{\beta_k}{4}|A_k|^4 + \frac{\gamma_k}{6}|A_k|^6 \tag{4.8}$$

where $\alpha_k(T)$ decreases with lowering temperature and $\gamma_k > 0$ to provide the global stability of the system. A second order phase transition to an incommensurate phase with a structural modulation corresponding to wave vector k_0 occurs at $T = T_i$ if (i) $\beta_{k_0} > 0$, (ii) $\alpha_k(T)$ has a

minimum at $k = k_0$, and (iii) $\alpha_{k_0}(T_i) = 0$. If $\beta_{k_0} < 0$, a first order phase transition will take place at a temperature higher than T_i.

This framework also enables a competing scenario with the formation of a commensurate modulated structure corresponding to the wave vector $\vec{k} = \vec{k}_\Sigma \equiv \frac{2\pi}{a}(1/4, 1/4, 0)$. The point is that, in view of a spatially oscillating form of the order parameter given by Eq. (4.7), for a general point of the Brillouin zone, only its absolute value (where the oscillations are eliminated) can enter the expression for the free energy (see Eq. (4.8)). Meanwhile, for the points corresponding to 1/4 of a reciprocal lattice vector, taking the 4th power of the order parameter eliminates these oscillations as well. This way the so-called Umklapp invariant $(A_k)^4 + (A_{-k})^4$ enters the Landau expansion [134]. Thus, the energy describing a transition with the wave vector $\vec{k}_\Sigma$ can be presented in the form

$$F_\Sigma = \frac{\alpha}{2}\rho^2 + \frac{\beta_\Sigma}{4}\rho^4 + \frac{\beta_U}{4}\rho^4 \cos 4\varphi + \frac{\gamma}{6}\rho^6 \tag{4.9}$$

where the third r.h.s. term is conditioned by the Umklapp invariant (β_U is the Umklapp coefficient). Here, α, β_Σ, and γ are $\alpha_k(T)$, β_k, and γ_k taken at $\vec{k} = \vec{k}_\Sigma$, respectively and the amplitude of complex order parameter is expressed in terms of its modulus ρ and phase φ:

$$A_k = \rho \exp(i\varphi). \tag{4.10}$$

The ground state for the system described by Eq. (4.9) occurs at the values of the order-parameter phase φ, satisfying the condition $\partial F_\Sigma / \partial \varphi = 0$. For $\beta_U > 0$, this minima in the free energy corresponds to $\varphi = \pi/4, 3\pi/4, 5\pi/4, 7\pi/4$, while, for $\beta_U < 0$, to $\varphi = 0, \pi/2, \pi, 3\pi/2$. Inserting these values of φ into Eq. (4.9), one finds the free energy in terms of the modulus of the order parameter

$$F_\Sigma = \frac{\alpha}{2}\rho^2 + \frac{\beta}{4}\rho^4 + \frac{\gamma}{6}\rho^6 \tag{4.11}$$

where $\beta = \beta_\Sigma - \beta_U$ for $\beta_U > 0$ and $\beta = \beta_\Sigma + \beta_U$ for $\beta_U < 0$. Note that $\beta < \beta_\Sigma$ independently of the sign of β_U.

Using Eq. 4.11, the condition for the appearance of a modulated structure with $\vec{k} = \vec{k}_\Sigma$ in PbZrO$_3$ (corresponding to the lead displacements) can be determined. First of all, if $\beta > 0$ this free energy cannot describe such a structure at all. In this case due to $\beta > 0$, a *second order* phase transition to the low temperature phase might occur, provided that $\alpha_k(T)$ has a minimum at $k = k_\Sigma$. However, the latter is not the case since the anomalous transverse mode does not have minimum at $k = k_\Sigma$ as seen from Fig.4.4. If $\beta < 0$, the free energy given by

Eq. (4.11) does describe a first order phase transition to a modulated structure with $\vec{k} = \vec{k}_\Sigma$. Remarkably, in this case there is no need in minimum of $\alpha_k(T)$ at $k = k_\Sigma$. In contrast to the case of the second order phase transition, the priority of the commensurate modulation is ensured not by the corresponding minimum on the dispersion curve of the relevant lattice excitation but rather by the fact that the coefficient for anharmonic term, β (controlling the transition at $\vec{k} = \vec{k}_\Sigma$) is always smaller than β_Σ which controls possible transitions at the neighboring wave vectors. Note that the energy of the anomalous acoustic mode at this wave vectors, ≈ 1.5 meV, is comparable with that of the ferroelectric soft mode in BaTiO$_3$ just above the first order phase transition, ≈ 1.8 meV (evaluated from the dielectric data). Thus we can consider the energy of the anomalous acoustic mode to be low enough to trigger a first-order phase transition.

Thus the weak softening of the anomalous transverse mode with lowering temperature is compatible with the formation of a modulated structure with $\vec{k} = \vec{k}_\Sigma$ via a first order phase transition. The characteristic pattern of the lead displacements in PbZrO$_3$ shown in Fig.2.2a can be readily reproduced under the condition $\beta_U > 0$ through the relation:

$$\vec{r}_{Pb} \propto \begin{pmatrix} -1 \\ 1 \\ 0 \end{pmatrix} \cos\left[\frac{\pi}{2a}(x+y) + \varphi\right] \tag{4.12}$$

where x and y are the lead ions' Cartesian coordinates in the cubic reference frame, and φ is the phase modulation (see Eq. 4.10). This scenario can be viewed as an incommensurate phase transition going directly to the lock-in phase skipping the incommensurate phase, the flexoelectric coupling being the driving force of the effect. The onset of this lock-in phase transition, "pushes back" the TO mode (through the disappearance of the central peak, seen in fig. 4.3) resulting in the absence of the ferroelectric phase transition.

4.5   Octahedra rotations

4.5.1   R-point

A complete description of the phase transition in PbZrO$_3$ needs to address the mechanism by which the additional oxygen octahedra tilts develop below T_A. These rotations were previously predicted to be associated with a softening at the R-point of the Brillouin zone[46, 47]. Figure 4.10 shows the evolution of the R-point IXS spectra at different temperatures. These spectra consist of the normal phonon resonances and the central peak. No temperature
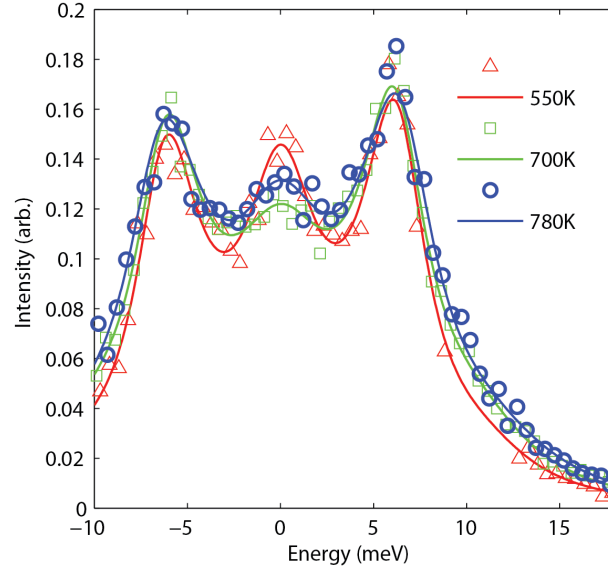
Figure 4.10: Experimentally measured IXS spectra at the R-point ($\vec{Q}$=(3.5 0.5 0.5)) at several temperatures. $\vec{Q}$ is measured in the units of the reciprocal cubic lattice constant $a^* = 2\pi/a$.

dependence of the phonon peaks is observed, while the central peak demonstrates weak increase on approaching the transition temperature. It is important to estimate whether the observed growth of the CP can be considered as an evidence of the instability relevant to the observed phase transition. In compounds containing heavy atoms it may be difficult [141] to reliably analyze the oxygen-involved zone-boundary distortions by X-ray scattering due to small atomic scattering factor of oxygen. However, in the case of inelastic scattering this is partially compensated by the small mass of the oxygen atoms, providing reasonable ratio of the scattering intensities due to modes dominated by the motion of heavy ions and oxygen-related modes. It can be shown that the scattering intensities of a lead containing mode and of a purely oxygen one, once these are of comparable frequencies, should differ by less than one order of magnitude.

Indeed the measurements at the mentioned R-point, presented in Fig. 4.10, give distinct spectra containing phonon resonances which one can tentatively identify with the overdamped R_{25} mode, and showing the central peak. In contrast with the temperature independent phonon resonances, the central peak demonstrates a traceable evolution with temperature. To quantify the evolution of the corresponding mode frequency, the fact that at high temperatures the temperature-normalized integral central peak intensity I_{CP}/T is proportional to the generalized static susceptibility is used [134]. The temperature evolution of T/I_{CP} is presented in Fig. 4.11. Apparently, the softening of the R_{25} mode does not correspond to any critical process
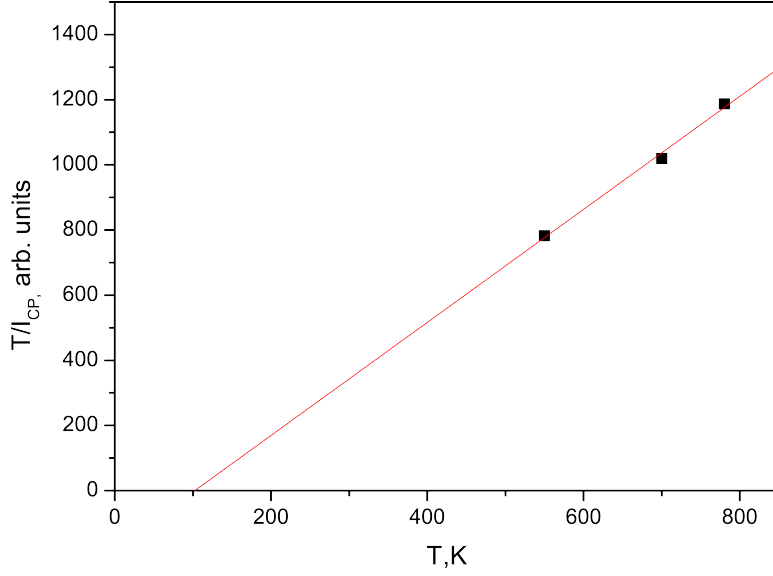
Figure 4.11: $T/I_{CP}(T)$ dependence, where I_{CP} - integrated intensity of the central line at R-point ($\vec{Q}$=(3.5 0.5 0.5)). $\vec{Q}$ is measured in the units of the reciprocal cubic lattice constant $a^* = 2\pi/a$.

with characteristic temperature close to the transition temperature (503 K). The extrapolation of the temperature trend of T/I_{CP} gives the critical temperature about 100 K, making it unlikely for the R point to be a relevant instability with regard to the AFE phase transition at $T = 503$ K.

4.5.2 Holakovsky mechanism

Instead, these rotations are described as being triggered by the Holakovsky mechanism [130], which was recently identified in perovskite ferroelectrics [142]. Similar to the above treatment of the suppressed ferroelectricity, the expansion of the free energy in terms of the order parameter (ρ) describing lead displacements for a given orientational domain state and a real pseudovector $\vec{\Phi}$ describing the oxygen-octahedron rotations, is given as follows:

$$F_\Phi = \frac{1}{2}\alpha_\Phi \Phi^2 + \frac{1}{2}\delta_{\Phi 1}(\Phi_1^2 + \Phi_2^2)\rho^2 + \frac{1}{2}\delta_{\Phi 3}\Phi_3^2\rho^2 + F_\Sigma + \text{high-order terms in } \Phi. \qquad (4.13)$$

where F_Σ is a function of the Σ-point order parameter only. If at least one of the coupling constants $\delta_{\Phi 1}$ and $\delta_{\Phi 3}$ is negative, the appearance of the spontaneous order parameter of the transition, ρ_0, may trigger the appearance of the order parameter Φ. This happens if at the transition point either $\alpha_\Phi + \delta_{\Phi 1}\rho_0^2$ or $\alpha_\Phi + \delta_{\Phi 3}\rho_0^2$ is negative. In the case of PbZrO$_3$ $\Phi_1 = \Phi_2 \neq 0$ while $\Phi_3 = 0$ [32]. Hence, in the case where $\delta_{\Phi 1} < 0$ and at the transition $\alpha_\Phi + \delta_{\Phi 1}\rho_0^2 < 0$., the described oxygen octahedral rotations are obtained. This is proposed as the mechanism

for the onset of the oxygen octahedral rotations. Thus, in the current scenario, the oxygen-octahedron rotations in PbZrO$_3$ are induced by the anti-polar lead displacements via an attractive biquadratic mode coupling.

4.6 Antiferroelectricity

The anti-polar lead displacements giving the quadrupling of the unit cell can ,thus ,be viewed as a result of the softening of a zone-center ferroelectric mode. At the same time the ferroelectric instability does not lead to the formation of a stable ferroelectric state in PbZrO$_3$. The suppression of the ferroelectric instability can be explained in terms of a two-mode model with competing interactions [56]. For PbZrO$_3$, these two modes are the zone-center ferroelectric polar mode with polarization P as the order parameter and the Σ_3 mode associated with the lead displacement. Taking into account the symmetry of the problem, the free energy describing the aforementioned competing interaction reads:

$$F(P, \xi) = \frac{1}{2} A(T - T_0) P^2 + \frac{1}{2} \delta_{P1} (P_1^2 + P_2^2) \rho^2 + \frac{1}{2} \delta_{P3} P_3^2 \rho^2 + F_A(\xi) \tag{4.14}$$

The term $F_A(\xi)$ describes the free energy associated with the structural order parameter and accommodates the terms describing Umklapp interaction that triggers the transition and the constants δ_{P1} and δ_{P3} define the repulsive biquadratic coupling between the polarization and the structural order parameter.

4.6.1 Dielectric Anomaly

The equation of state for polarization $\partial F / \partial P_i = E_i$ (E_i is a component of electric field vector), for the high-temperature phase (with $\xi = 0$), yields the Curie-Weiss law $\chi \propto 1/(T - T_0)$ for the dielectric susceptibility defined as $\chi = dP/dE$. For the low-temperature phase where the order parameter of the transition, ξ, acquires a spontaneous value ρ_0, the susceptibility is described by a diagonal tensor with elements

$$\chi_{ii} = \frac{1}{A(T - T_0) + \delta_{\text{Pi}} \rho_0^2}, \tag{4.15}$$

where ρ_0 is the modulus of the spontaneous value of the structural order parameter $\xi_0 = \rho_0 \exp(i \vec{q}_\Sigma \vec{r} + i\phi)$. Here the subscripts in χ_{ii} do not mean summation. Equation (4.15) correspond to the aniferroelectric-type anomaly if the denominators $A(T - T_0) + \delta_{\text{Pi}} \rho_0^2$ increase

on cooling. This is possible if the increase of ρ_0 with lowering temperature dominates the behavior of these terms. Such a condition can be assured by large enough coupling constants δ_{P1} and δ_{P2}. Thus, the ferroelectric instability does not end up with a ferroelectric phase for it is suppressed by the developed structural order parameter.

4.7 Conclusions

The antiferroelectricity in PbZrO$_3$ has been studied using off-zone-center scattering experiments to understand the interplay between the order parameters actively participating during the phase transition. It has been seen that the slowing down of the TO mode induces the slowing down of the TA mode in the $\Gamma - M$ direction on approaching the phase transition through flexoelectric coupling. While it is the TO mode that drives the phase transition, the TA mode at finite q in this direction corresponds to the motion of the primary order parameter, i.e. the antiphase Pb shifts. This system is potentially unstable against incommensurate modulations, but through sufficiently large Umklapp interactions, it goes directly to the commensurate phase, leaving the incommensurate phase unattained. In this manner, the ferroelectric softening is subdued to yield an antiferroelectric transition. Through repulsive and attractive biquadratic couplings respectively, the spontaneous polarisation is suppressed and the oxygen octahedral rotations are invoked. Using the anti-parallel Pb shifts as the primary order parameter, and constructing a two-mode free energy model with a coupling of the former with other order parameters, the characteristics of antiferroelectrics, e.g. the dielectric anomaly can be explained.

5 Growth and structural control of PbZrO$_3$ thin films

Thin films of PbZrO$_3$ were grown for the observation of the polarisation within the anti-phase domain boundaries. Considering the large misfit strain between PbZrO$_3$ and most single crystalline substrates, buffer layers of BaZrO$_3$ were used to modulate the misfit strain acting at the lower interface of the PbZrO$_3$ film. Using Pulsed Laser Deposition (PLD) as the growth technique, the growth conditions were optimised to obtain epitaxial films despite the large misfit strain. By varying the thickness of the buffer layer, and thus by varying the misfit strain at the lower interface of the PbZrO$_3$ film, a systematic control over the domain composition of the thin film as well as the misfit dislocation density at the film interface was achieved.

Thin films of PbZrO$_3$ are ideal materials for the analysis of structural anomalies. Defects such as antiphase boundaries that are related to other defects such as dislocations can be more easily controlled in thin films than in single crystals owing to an easier modulation of the stress conditions in the former through the control of epitaxial strain. To this end, epitaxial thin films of PbZrO$_3$ are fabricated with the use of buffer layers of BaZrO$_3$. Though the use of BaZrO$_3$ as a relaxed buffer layer to obtain a tensile misfit strain for PbZrO$_3$ is known [43, 98], the controlled use of BaZrO$_3$ to tune the interfacial strain remains unexplored, and has been undertaken in the present study. The effect of the modulation of interfacial strain on the domain orientations and the defect density is analysed as well.

5.1 Experimental Details

5.1.1 Target Preparation

Polycrystalline ceramic targets of PbZrO$_3$ were prepared through solid state reaction process using starting powders of PbO and ZrO$_2$ of very high purity (>99.9 %). In order to compensate for the lead loss during the calcination and sintering processes and to a ensure stoichiometric composition during the film deposition, a 10 % excess of PbO was included in the initial oxide mixture. The powders were mixed thoroughly with a 1.1:1 (PbO:ZrO$_2$) molar ratio in an attritor mill using an isopropyl alcohol medium for 24h. The mixed powders were then dried and calcined in a sealed crucible at 800°C for 3 hours. The powders showed less than 1% of weight loss after the calcination process. An X-Ray diffraction (XRD) Analysis of the composition of the calcined powders showed the existence of only two compositions corresponding to PbZrO$_3$ and PbO. The calcined powders were mixed and pressed uniaxially in a cylindrical mould with a force of 10kN to yield 32mm diameter pellets, which were then sintered at 1200°C for 2h. To ensure minimal lead loss from the pellets during sintering, the pellets were placed within a sealed crucible in a bed of PbZrO$_3$ powder of the same compositon. The sintered pellets had a relative density higher than 95 % and had suffered less than 1% weight loss during the sintering process. XRD analysis of the sintered pellet (see Fig. 5.1) shows only the PbZrO$_3$ peaks with traces of PbO originating from the excess PbO added initially. Similarly, dense targets (>95% relative density) of BaZrO$_3$ were prepared using commercial BaZrO$_3$ powder with the sintering conducted at 1650°C for 12h.

5.1.2 Substrate Treatment

All films were grown on commercially available pure SrTiO$_3$ and 0.5% Nb doped-SrTiO$_3$ single crystal substrates oriented along the (001) direction, manufactured by Crystech GmbH. These substrates are known to have mixed oxide termination on the surface owing to their processing history which can prove disadvantageous for perfect 2-dimensional heteroepitaxial growth of thin films [143]. To ensure atomic smoothness of the surface of these substrates before the film deposition, the substrates were immersed in deionised water for 30mins to hydrolyse the SrO oxide terminations on the surface, following by etching in a buffered HF solution (pH=1) for 25s to attack the hence formed Sr(OH)$_2$, leaving behind only a TiO$_2$ terminated surface. The treated substrates are then annealed at 925°C for 1h in order to help the diffusion of these TiO$_2$ adatoms towards the nearest edge, finally resulting in well ordered terraces of one unit cell height, as seen from in Fig. 5.4 (a).
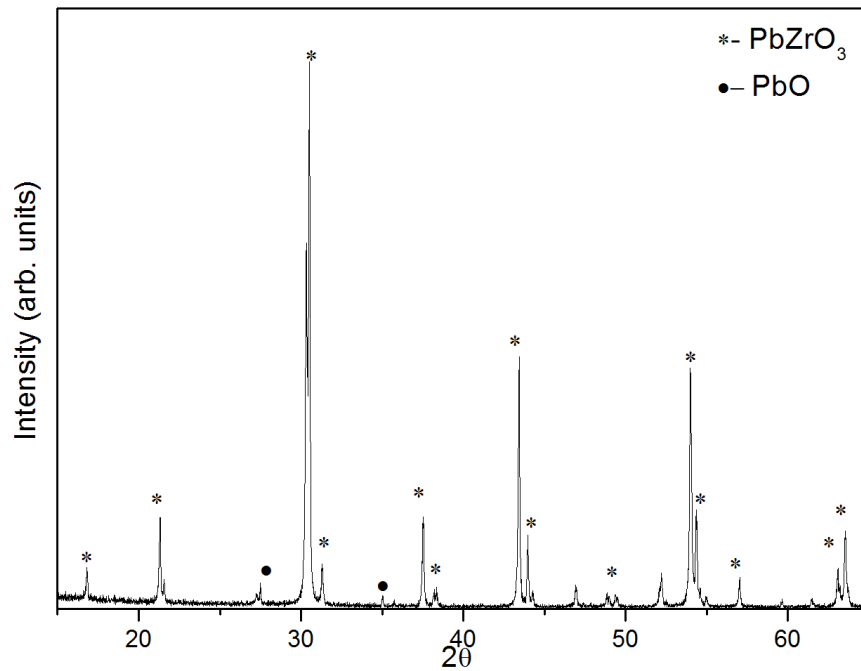
Figure 5.1: X-Ray Diffraction analysis of the PbZrO$_3$ target showing peaks from the bulk PbZrO$_3$ with some traces of PbO arising from the excess PbO added during the calcining process to compensate for the lead loss.

5.1.3 Growth Conditions

Thin films were deposited by Pulsed Laser Deposition (PLD) using a KrF excimer laser (λ= 248nm). Except for the films grown on the Nb-SrTiO$_3$ substrates, wherein owing to its conductive nature the substrate itself acted as a bottom electrode for the thin film capacitor, all other films were grown on top of insulating layers (either the substrate SrTiO$_3$ or the buffer layer BaZrO$_3$). For each of the layers grown, the growth parameters including the temperature, the partial pressure of oxygen in the chamber, the pulse rate of the laser, the laser energy, and the seperation between the substrate and the target were optimised to obtain smooth films with surface roughness lower than 1nm and with minimal particles on the surface. The optimised parameters for the growth of the various layers are shown in Table 5.1. The average growth rate was calculated by dividing the thickness of the film obtained after 30mins of deposition (observed from XRD or TEM) by the number of pulses used. In order to study the effect of relaxation of the buffer layer (BaZrO$_3$) on the interface between the BaZrO$_3$ and PbZrO$_3$ films, the thickness of the BaZrO$_3$ layer was varied from 0 to 60nm. A minimum thickness of 50nm was ensured for all the PbZrO$_3$ films grown.

Parameter	PbZrO$_3$	BaZrO$_3$
Growth Temperature(^{o}C)	565	650
Partial pressure of oxygen(mTorr)	150	150
Laser pulse rate (Hz)	3	3
Laser beam energy (mJ)	200-220	200
Average growth rate (*10^{-2} nm/pulse)	7	8

Table 5.1: Table of optimised parameters for growth of thin films

5.2 Reconstruction of the orthorhombic unit cell

On passing through the phase transformation temperature into the orthorhombic structure, the cubic axes of PbZrO$_3$ can convert into either of the 3 orthorhombic directions (refer Fig. 5.2): [120]$_o$, [-210]$_o$ and [002]$_o$, where the subscript 'o' stands for orthorhombic axes. The magnitude of the pseudocubic lattice parameter along [001]$_o$ is 0.411nm, while along both [120]$_o$ and [-210]$_o$ this value is around 0.416nm, varying by less than 0.2%. For conventional XRD techniques, the distinction between the [120]$_o$ and [-210]$_o$ is extremely difficult because of limiting experimental resolution. The distinction between the [120]$_o$ and [002]$_o$ is, nonetheless, possible. To this effect, a pseudotetragonal symmetry is assumed in this chapter to discuss the thin films, with the [120]$_o$ and [-210]$_o$ directions considered parallel to the a-axis of the pseudotetragonal structure, and the [002]$_o$ considered as the c-axis of the pseudotetragonal structure, as shown in Fig. 5.2.

(a) **(b)**
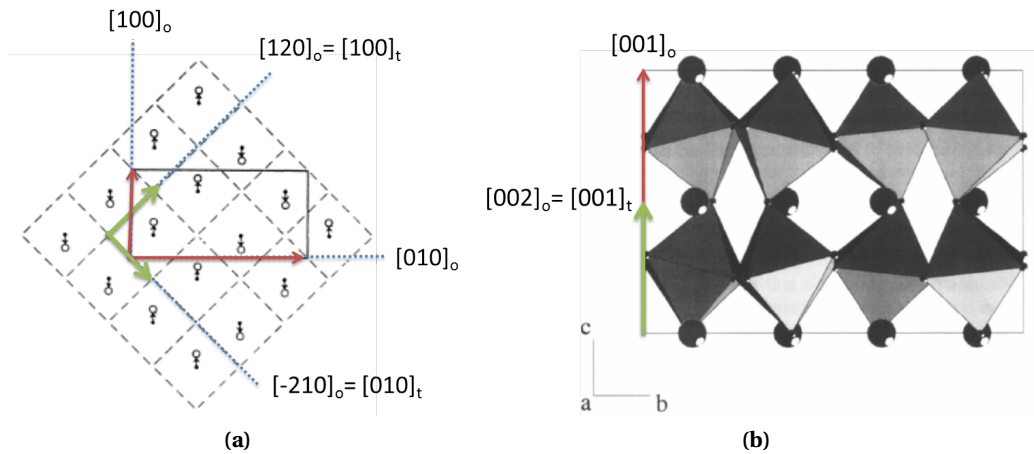
Figure 5.2: (a)The a-b plane of the orthorhombic unit cell (solid lines) constructed from the pseudocubic unit cell (dashed lines)[8]. The [120]$_o$ and [-210]$_o$ directions are indistinguishable from conventional XRD patterns and the lattice unit cell is redefined as a pseudotetragonal lattice with the a-axes (marked as [100]$_t$ and [010]$_t$) parallel to the [120]$_o$ and [-210]$_o$ directions in the orthorhombic unit cell. (b) The b-c plane of the orthorhombic unit cell [141] showing the orthorhombic [001]$_o$ and pseudotetragonal-c (marked as [001]$_t$)axes.

5.3 Misfit and thermal strain calculations

The variation of the lattice parameters of $PbZrO_3$, $SrTiO_3$ and $BaZrO_3$ with temperature [32, 144, 145] are shown in Fig. 5.3. While $PbZrO_3$ has a cubic perovskite structure with a lattice parameter of 0.416nm at its growth temperature (565^oC), at the same temperature both $SrTiO_3$ and Nb-$SrTiO_3$ substrates have a cubic perovskite structure with a lattice parameter of 0.392nm. This corresponds to a compressive misfit strain of 5.8% for a $PbZrO_3$ film grown directly on the substrate. In order to moderate this lattice strain experienced at the $PbZrO_3$ film interface, $BaZrO_3$ was employed as a buffer layer between the substrate and the $PbZrO_3$ film. $BaZrO_3$ has a cubic perovskite lattice structure, with a lattice parameter of 0.421 nm at its growth temperature(650^oC) corresponding to a compressive misfit strain of 7.2% when grown on $SrTiO_3$ (lattice parameter 0.393nm at 650°). The thermal strain accumulated in the $BaZrO_3$ layer between its growth temperature and the growth temperature of $PbZrO_3$ (with a thermal expansion coefficient of $3*10^{-6o}C^{-1}$) is less than 0.07% and is neglected henceforth. $PbZrO_3$ when grown on fully relaxed films of $BaZrO_3$ will experience a tensile misfit strain of 1.2%. $BaZrO_3$ buffer layers were thus used to moderate the interfacial strain for the $PbZrO_3$ film, ranging from high compressive strains for very thin layers, to tensile strains for thick layers. The coefficients of thermal expansion for (cubic) $PbZrO_3$ and $BaZrO_3$ are around $3*10^{-6o}C^{-1}$, the corresponding value for $SrTiO_3$ is determined to be $2.3*10^{-6o}C^{-1}$ implying a thermal strain of <0.1% from the substrate. Comparing this value with the pre-existent lattice mismatch (>5%), the thermal mismatch is neglected.

The critical thickness (h_c) [74] for the formation of misfit dislocations (with burgers vector along <110>) in the cubic phase was calculated using the Eq. 2.4. The values used for the calculation of the critical thickness of the films are given in Table 5.2. Given the high misfit strains between the substrate and the oxides grown thereon, the critical thickness for the formation of dislocations is seen to be less than 1 unit cell, implying that right from the beginning of the growth of the film the elastic energy stored in a perfectly coherent interface between the oxide and the substrate would be theoretically large enough to allow for the formation of defects like dislocations, allowing for the film to start relaxing immediately.

Film	b (along <110>, in nm)	ν	f (%)	α	λ	h_c (nm)
$PbZrO_3$	0.588	0.3	5.8	90	0	0.27
$BaZrO_3$	0.595	0.3	7.2	90	0	0.29

Table 5.2: Table of parameters for determining critical thickness of $PbZrO_3$ and $BaZrO_3$ films grown on $SrTiO_3$. The misfit strain is calculated at the growth temperature.
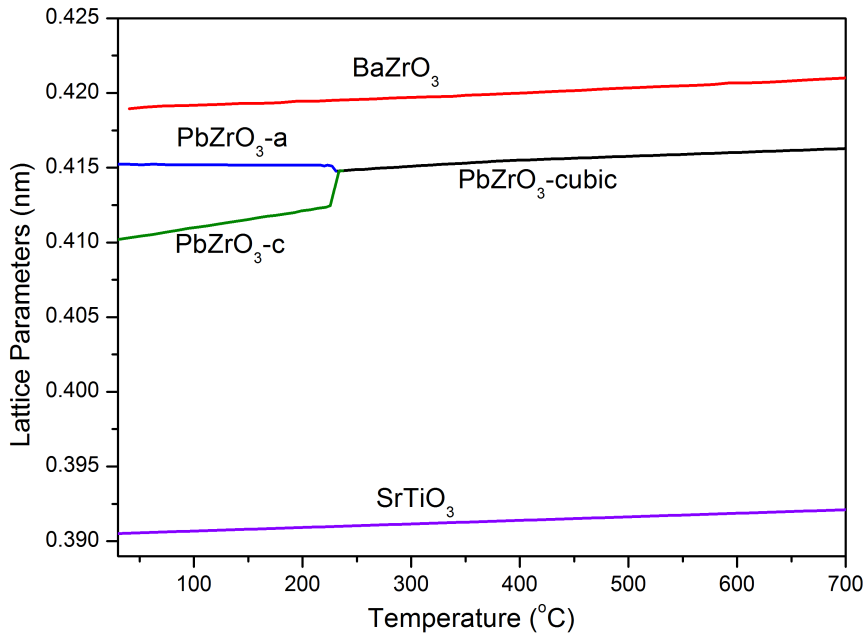
Figure 5.3: Variation of lattice parameters of SrTiO$_3$, BaZrO$_3$ and PbZrO$_3$ with temperature [32, 144, 145]. The PbZrO$_3$ unit cell is represented as a pseudo-tetragonal structure, as described previously. The thermal expansion coefficients of all the three materials are comparable and the thermal mismatch can thus be neglected.

5.4 Structural Characterisation of the films

5.4.1 Surface topography and crystalline quality

The surface topography of the films was studied by Atomic Force Microscope (AFM) using an Asylum Scanning Probe Microscope. Seen in fig. 5.4 are AFM images from typical films of BaZrO$_3$ and PbZrO$_3$ produced for this work. The topography for all films shows terrace formation, the origin of which can be traced back to the terrace-like topography of the treated substrate arising from the miscut angle associated with the substrate fabrication. The appearance of the particles was seen to be not systematic with variations in the growth parameters, but a high density is most likely to be associated with a low laser energy resulting in insufficient energy for the formation of the plasma during the growth.

XRD analyses were carried out on a Bruker-D8 Diffractometer and used to determine the orientation of the thin films. From a θ-2θ scan (see Figs. 5.5, 5.8),it was observed that the PbZrO$_3$ films showed only peaks corresponding to the $\{120\}_o$ and/or the $\{001\}_o$ peaks of the orthorhombic phase corresponding to the pseudotetragonal-a($\{100\}_t$) and the pseudotetragonal-c axes($\{001\}_t$), alongside the $\{001\}$ peaks of the substrate and of the buffer layer (wherever present), implying an epitaxial relation between the substrate and the film.

Figure 5.4: Typical AFM images corresponding to (a) annealed $SrTiO_3$ substrate (b) 10nm thick film of $BaZrO_3$ grown on $SrTiO_3$ (c) 60nm thick film of $PbZrO_3$ grown on 5nm thick $BaZrO_3$. The extension of the topography of the substrate to the top surface of the film is evident in the terraced topography of the films. All films have a surface roughness of <1nm when excluding the particles.

Transmission electron microscopy (TEM) imaging was carried out on the cross-section samples of the thin films on the Philips CM30 and the FEI OSIRIS microscopes. The images thus obtained (see Fig. 5.6) showed no grain boundaries in any of the samples and the selected area diffraction images showed single crystalline behaviour over large areas of sampling. A dotted contrast seen close to the interface with the substrate is associated with the dislocations arising from the relaxation of the large misfit strain between the $PbZrO_3/SrTiO_3$ or the $BaZrO_3/SrTiO_3$ systems (the latter not shown). These results combined with the XRD and the AFM analyses confirm the high crystalline quality of the thin films grown.
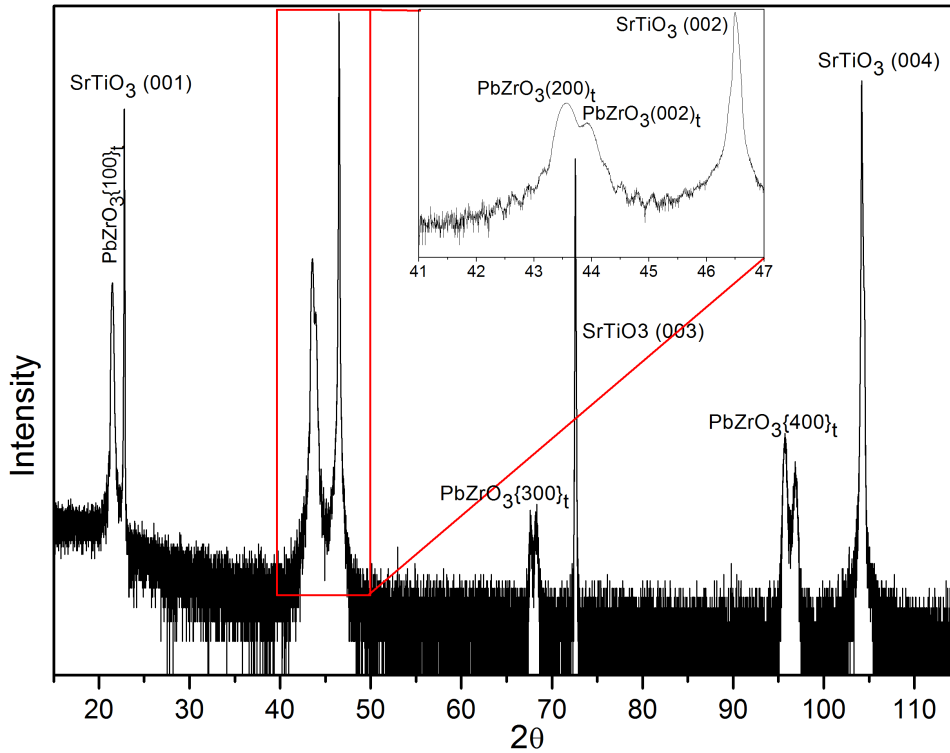
Figure 5.5: Typical $\theta - 2\theta$ scan for a PbZrO$_3$ film grown on top of an SrTiO$_3$ substrate showing only peaks corresponding to the $\{120\}_o/\{100\}_t$ and the $\{001\}_o/\{001\}_t$ family of planes from the PbZrO$_3$ film alongside the $\{001\}$ set of planes for the SrTiO$_3$ substrate. Inset: Magnification of the peaks around the (002) peak of the SrTiO$_3$ substrate showing the $(240)_o/(200)_t$ and the $(004)_o/(002)_t$ peaks from the PbZrO$_3$ film, implying an epitaxial growth of the thin film.

5.4.2 Growth mode

Given the absence of any evidence of step bunching at the surface from the AFM images, it can be safely concluded that the rate of arrival of the adatoms is lower than the time needed for the diffusion of the adatoms along the surface towards the nearest step, allowing for the growth of the films in a step-flow growth mode. Nevertheless, it is not impossible that multiple nucleation sites form on each step of the substrate, leading to the formation of epitaxial islands which eventually coalesce to form a single epitaxial layer. The coalescence of such epitaxial islands usually results in the formation of threading dislocation loops. This is observed in Fig. 5.6 where one notices threading segments climbing down from the surface without reaching the interface, thus substantiating the claim of the growth and coalescence of epitaxial islands.
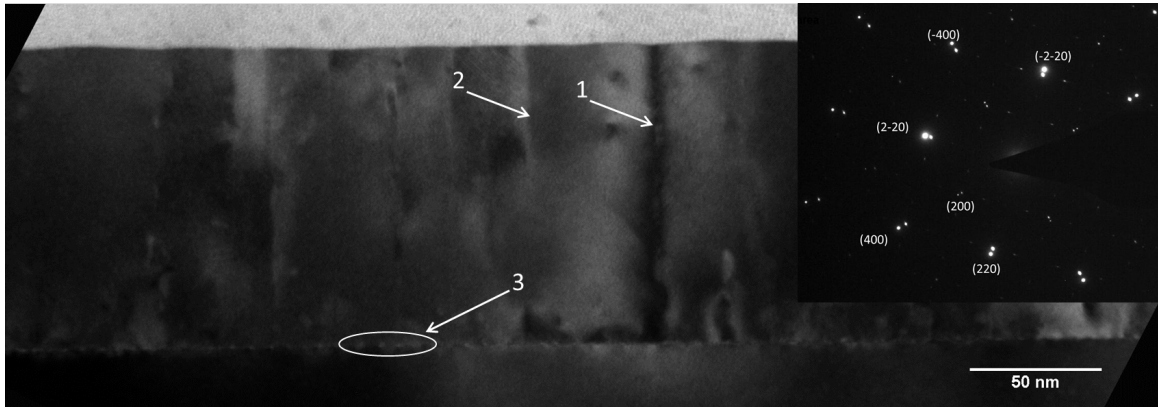
Figure 5.6: Cross section bright field TEM image of a 120nm thick PbZrO$_3$ film grown on SrTiO$_3$. The lines running between the top surface and the substrate (marked as '1') represent the threading dislocations arising during the growth of the thin film. Threading segments from the surface that climb down partially without reaching the substrate (marked as '2') suggest the growth from coalescence of epitaxial islands. The spot contrast seen close to the interface (marked as '3') arises from the misfit dislocations due to the relaxation of the high misfit strain. Inset: Selected Area Diffraction image taken from 1 micron length of the film showing epitaxial relation between the substrate and the film from the twin spots. Note: Only the cubic notations for the substrate (corresponding to pseudotetragonal notations for PbZrO$_3$) are indicated. The observations were carried out by Dr. Cosmin Sandu.

5.4.3 Control of domain fraction

5.4.3.1 Domains in pseudotetragonal PbZrO$_3$

Starting from the pseudotetragonal unit cell used to describe the PbZrO$_3$ unit cell in its low temperature phase, for a cube-on-cube epitaxial thin film of PbZrO$_3$ grown in its cubic phase, the low temperature phase can result in three different domains as shown (with some exaggeration of the tetragonality) in the schematic Fig. 5.7(a). When considering the analyses of these domains using regular $\theta - 2\theta$ scans, the out-of-plane lattice parameters for domain types A and B are identical, and hence are indistinguishable, whereas the out-of-plane lattice parameter for domain type C is sufficiently different from A and B, making it distinguishable from the latter two. The difference in the three domain types could potentially be derived by measuring simultaneously the in-plane and the out-of-plane lattice parameters, which in this study has been attempted through the measurement of reciprocal space maps. The in-plane (IP) and the out-of-plane (OP) lattice parameters for the three variants are in the following order:

$$IP(A) = IP(C) > IP(B) \tag{5.1}$$

$$OP(A) = OP(B) > OP(C) \tag{5.2}$$

which would result in a reciprocal space map as shown in Fig. 5.7(b) with respect to the substrate (which has a much smaller lattice parameter). Though ideally one would expect to see the difference in the peaks between the domain variants A and B, the resolution of the measurement of the in-plane lattice parameter is lower than that for the out-of-plane lattice parameter, and in this case, prevents the distinction of the peaks arising from variants A and B, as will be seen later.
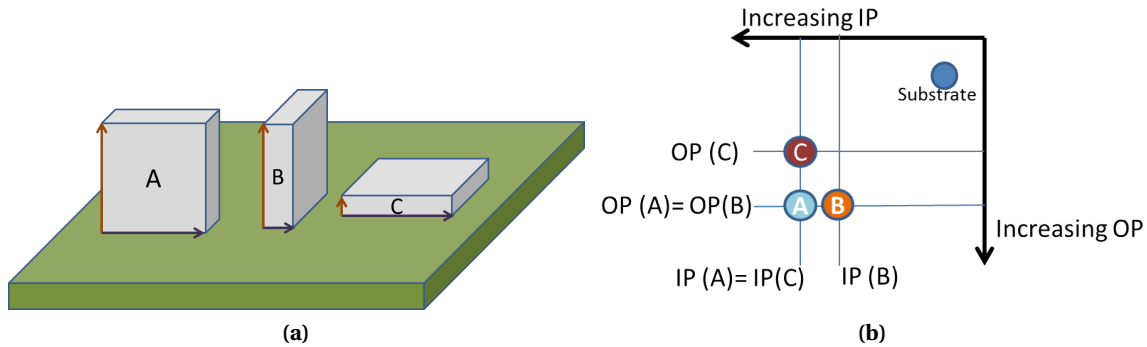
Figure 5.7: (a)Three possible domain variants for the pseudotetragonal PbZrO$_3$ unit cell showing their corresponding in-plane (black arrows) and out of plane (red arrows) lattice parameters. (b) A schematic of the mapping for the three domain variants w.r.t. the substrate derived from the relative magnitudes of the in-plane(IP) and the out-of-plane (OP) lattice parameters for the three domain variants shown in (a).

5.4.3.2 Domain fraction control through interfacial strain

The domain fractions in PbZrO$_3$ films are related to the interfacial misfit strain owing to the difference in the misfit strains associated with each domain variant w.r.t the substrate. This effect was previously studied and a compressive strain was found favourable for domain variants A and B (without any distinction between the two), while a tensile strain was said to favour the variant C [43, 98], though the change in the domain fractions with varying magnitudes of interfacial strains and the effect of the interface between the film and the substrate (through the presence of an ultrathin buffer layer) was not analysed.

To analyse this effect, the thickness of the BaZrO$_3$ film was varied from 0 to 60nm, allowing for the BaZrO$_3$ buffer layer to relax to varying extents, and hence varying the misfit strain for the PbZrO$_3$ layer grown subsequently on top of the BaZrO$_3$ film. For determining the out-of-plane orientation of these films, XRD analysis through $\theta - 2\theta$ was carried out on the films for 2θ values varying between 42° and 47°. Besides the substrate peaks, the resulting spectra consists principally of three peaks from all the films (see Fig. 5.8): (002) peak from the BaZrO$_3$ film at 43.1^o, the $(240)_o/(200)_t$ peak of the PbZrO$_3$ film at 43.5 ^{o} (corresponding to the domain

variants A and B) and the $(004)_o/(002)_t$ peak of the PbZrO$_3$ film at 44° (corresponding to the domain variant C). When comparing the diffraction data obtained from the different films by varying the thickness of the buffer layer, it is observed that with increasing thickness of the buffer layer, i.e. with increasing intensity of the (002) peak of BaZrO$_3$, there is a rapid decrease in the intensity of the peak corresponding to the A and B variants and an increasing intensity in the C variant.
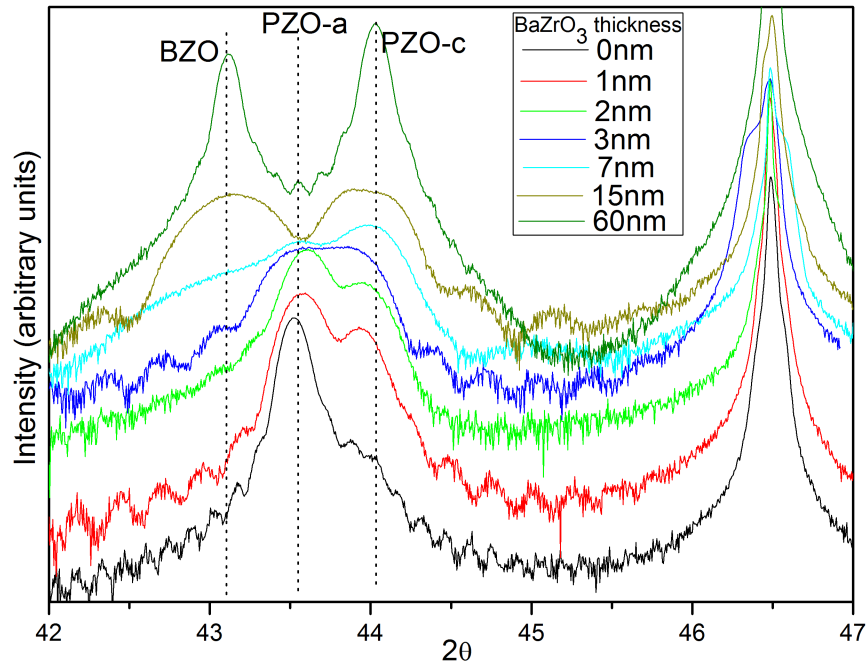
Figure 5.8: X-Ray diffraction data obtained from 70nm thick films of PbZrO$_3$ grown directly on single terminated SrTiO$_3$ substrates with varying thickness of BaZrO$_3$ buffer layer. Three principle peaks corresponding to the (002) plane of the BaZrO$_3$ (marked BZO), domain variants A and B from PbZrO$_3$ (marked as PZO-a), and domain variant C from PbZrO$_3$ (marked as PZO-c) are seen. With increasing buffer layer thickness, a decrease in the fraction of A and B domains and an increase in the fraction of the domain C is clearly observed.

For the reciprocal space maps, the (103) peak of the SrTiO$_3$ substrate was chosen as a reference and the corresponding $\{103\}_t$ peaks from the three domain variants of PbZrO$_3$ layer were mapped in relation to the SrTiO$_3$ peak. Shown in Fig. 5.9 are three such reciprocal space maps for three different thicknesses of the BaZrO$_3$ layer (1nm, 3nm and 7nm), with peaks corresponding to the SrTiO$_3$ (103) peak and the $\{103\}$ peaks from the A+B and C domains variants in the PbZrO$_3$ layer (labelled PZO-a and PZO-c respectively). On correcting the position of the SrTiO$_3$ (103) peak to standard bulk values and applying the same correction to the PZO-a and PZO-c peaks, the lattice parameters for the a and the c-axes of the PbZrO$_3$ pseudotetragonal unit cell were found to be 0.415nm and 0.411nm, corresponding well to their bulk lattice parameters, thus implying fully relaxed films in all cases. Simultaneously, on comparing the relative intensities of the PZO-c and the PZO-a peaks from these films, it

is observed that the intensity of the PZO-a peak decreases rapidly with increasing BaZrO$_3$ thickness, being barely discernable for the film with a BaZrO$_3$ layer of 7nm. This corroborates well with the $\theta - 2\theta$ results wherein one sees a faint PZO-a peak, and for all thicknesses of BaZrO$_3$ higher than 7nm, the peak becomes invisible. Conclusively, on increasing the thickness of the BaZrO$_3$ layer from 0 to over 15nm, the orientation of the PbZrO$_3$ film converts from a purely pseudotetragonal-a oriented film at 0nm to a purely pseudotetragonal-c oriented film above 10nm, with a mixture of the two domains existing in between these two values.

In order to explain the variation in the fraction of each of the domain variants in the films with/without a buffer layer of BaZrO$_3$, one can resort to the energetics associated with the domain formation [43, 98]. The elastic energy associated with an epitaxially grown film in the absence of dislocations is known to scale with the square of the misfit strain (U$_{epi} \propto \epsilon^2$)[78]. Though in these samples the formation of dislocations occurs fairly early into the growth of the film, the release of elastic energy from the formation of dislocations is assumed constant in all cases as a first approximation. Two perpendicular azimuthal directions along the substrate are considered, and using the different epitaxial relations for the two differentiable domain variants, the misfit strain (ϵ) along these two directions is calculated individually using Eq. 5.3. The sum of the squares of the misfit strains from the two different directions is used to denote the strain factor (k, see Eq. 5.4) which scales linearly with the elastic energy (U) of the system.

$$\epsilon_i \text{(in \%)} \quad = \quad \frac{(d_i^{\text{film}} - d_i^{\text{lowerlayer}})}{\frac{(d_i^{\text{film}} + d_i^{\text{lowerlayer}})}{2}} X100 \tag{5.3}$$

$$U \propto k \quad = \quad \epsilon_1^2 + \epsilon_2^2 \tag{5.4}$$

This technique is applied for both the A/B and the C variants, growing on pure SrTiO$_3$ and on completely relaxed BaZrO$_3$ individually. The epitaxial relations for the azimuthal planes used in the calculation of the misfit strain, for the two domains is given by:

For A and B variants

$$(100)_t^{PZO} || (100)^{STO/BZO} \text{ and } (001)_t^{PZO} || (010)^{STO/BZO} \tag{5.5}$$
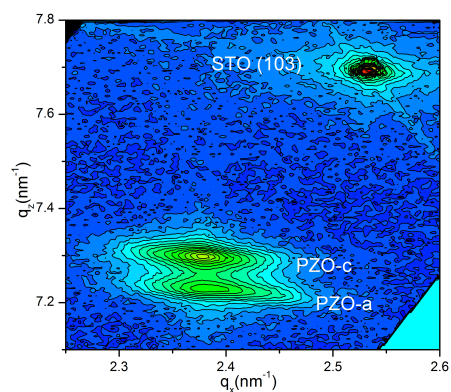
(a)
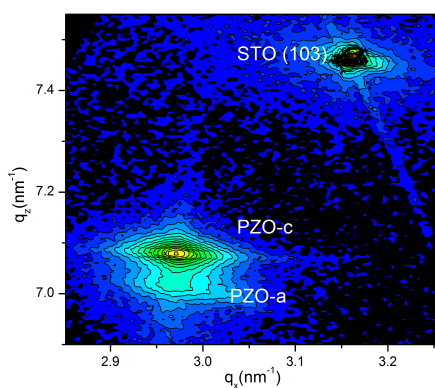
(b)
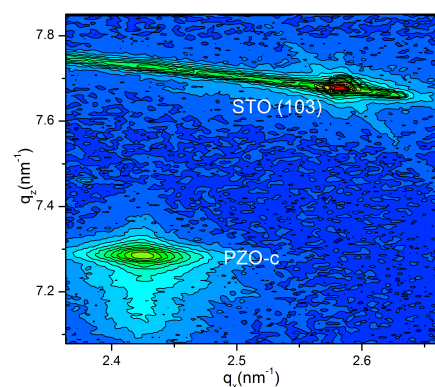
(c)

Figure 5.9: Reciprocal Space Maps obtained through High Resolution XRD measurements showing the positions of the (103) peak of SrTiO$_3$ (labelled STO) and the corresponding {103}$_{pc}$ peaks from the A and B domain variants (labelled PZO-a) and the C domain variant (labelled PZO-C) in the thin films, for BaZrO$_3$ buffer layer thickness corresponding to (a) 1nm, (b) 3nm and (c) 7nm. With increasing buffer layer thickness, a decrease in the A and B domain variant and an increase in the C domain variant is observed. All PbZrO$_3$ films are 70nm thick.

System	d$_1^{PZO}$	d$_1^{STO/BZO}$	d$_2^{PZO}$	d$_2^{STO/BZO}$	ϵ_1	ϵ_2	k
A/B variant on SrTiO$_3$	0.416	0.392	0.411	0.392	6.38	5.25	68.27
C variant on SrTiO$_3$	0.588	0.554	0.588	0.554	6.55	6.55	82.85
A/B variant on BaZrO$_3$	0.416	0.421	0.411	0.421	-0.66	-1.79	3.64
C variant on BaZrO$_3$	0.588	0.595	0.588	0.595	-0.67	-0.67	0.6425

Table 5.3: Table of strain factors corresponding to two different epitaxial domains on two different lower layers

For C variant

$$(110)_t^{PZO}||(110)^{STO/BZO} \text{ and } (1-10)_t^{PZO}||(1-10)^{STO/BZO} \qquad (5.6)$$

Using the relations 5.5 and 5.6 with the bulk lattice parameters for the different directions, the energy factor for the 4 cases was calculated. Since a higher value of 'k' implies a higher contribution of the misfit strain to the elastic energy of the system, the system with a lower k would energetically be preferred to others. Using this interpretation and the results of the calculations shown in Table 5.3, it is easily identified, that in the case of compressive strain, i.e. when the PbZrO$_3$ film is grown on pure SrTiO$_3$ or on very thin layers of BaZrO$_3$, the A and B variants are preffered over the C variant, whereas for the case of tensile strain, i.e. when the PbZrO$_3$ film is grown on a completely relaxed film of BaZrO$_3$, the C variant is preferred, which correlates perfectly with the observations in the current study. Moreover, on comparing the differences between the values of k for the two variants on SrTiO$_3$ and for the two variants on BaZrO$_3$, the values of k for the former varies by about 20% (between 68.27 and 82.25) while for the latter the variation is almost 600% (between 2.89 and 7.36). This suggests accordingly that the effect of stabilisation of the C variant by BaZrO$_3$ is much larger than the effect of the compressive strain from SrTiO$_3$ towards the preference for the A/B variants.

The choice of the preferred domain variant is extremely sensitive to the condition of the interface as well. When growing infinitesimally thin BaZrO$_3$ layers, the thickness of the grown BaZrO$_3$ layer is determined through extrapolation of the growth rate from thicker layers towards shorter deposition times. It is highly possible, that at estimated thicknesses of the order of 1nm, the BaZrO$_3$ film is discontinous on the SrTiO$_3$ surface, implying that the PbZrO$_3$ film that is subsequently grown on the BaZrO$_3$ layer is partially exposed to BaZrO$_3$ and partially to SrTiO$_3$. Even at such infinitesimal thicknesses and incomplete coverage, the rise in the fraction of C variant is rapid. Compared in Fig. 5.10 are the $\theta - 2\theta$ scans from 75nm thick PbZrO$_3$ films grown directly on SrTiO$_3$ and on a BaZrO$_3$ layer of expected thickness of 1nm. The increase in the stability of the C variant in the presence of such an infinitesimal,

discontinous layer of $BaZrO_3$ is remarkable despite the negligible difference in the misfit strain in the 2 cases. Also, when comparing $\theta - 2\theta$ spectra from $PbZrO_3$ films of different thicknesses grown on the same discontinous layer of $BaZrO_3$ (1nm thick), with increasing deposition time, i.e. with increasing thickness of the $PbZrO_3$ layer, the fraction of the C variant is seen to increase (see Fig. 5.11), though for similar thicknesses of $PbZrO_3$ films grown directly on $SrTiO_3$, only a very small increase in the C variant is seen with increasing $PbZrO_3$ thickness. All these results point towards the heavy stabilisation of the C variant in the presence of $BaZrO_3$, as was stated previously while considering the energetics.
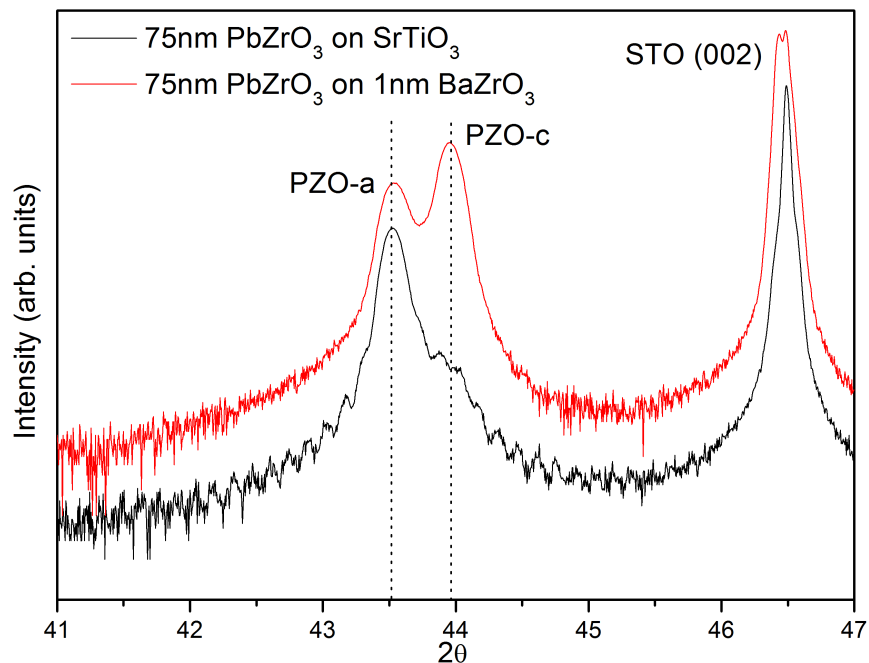
Figure 5.10: X-Ray diffraction data comparing the domain fractions in 75nm thick $PbZrO_3$ films grown on pure $SrTiO_3$ and on 1nm. thick $BaZrO_3$. Despite the infinitesimal thickness of the $BaZrO_3$ film, it is seen to stabilise heavily the C variant domain.

In summary, though previous studies suggest the stabilisation of the A/B variants for compressive interfacial strains and the C variant for tensile interfacial strains [43, 98], it is observed here that along with the stress state, the interface plays a role in favouring certain domain orientations as well. As an example, a 1nm thick layer of $BaZrO_3$, whose contribution to relieving interfacial strain is negligible, stabilises substantially the C variant despite the presence of a compressive interfacial strain. Nevertheless, while controlling the interfacial strain through the thickness of the $BaZrO_3$ buffer layer, mixtures of A/B and C domain states of varying fractions can be obtained for varying interfacial misfit strains.
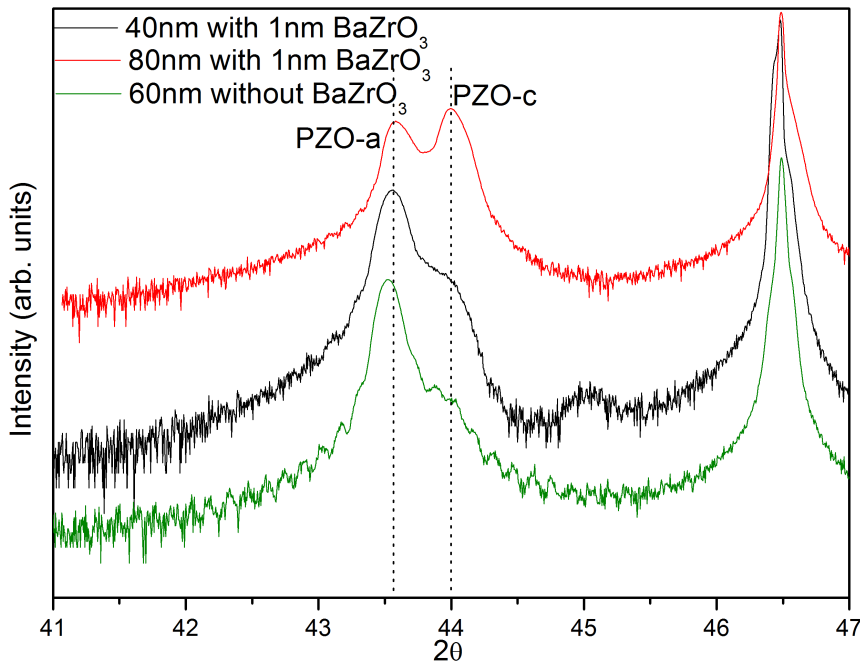
Figure 5.11: Comparison of domain fractions in PbZrO$_3$ films with increasing thickness with and without 1nm thick buffer layer of BaZrO$_3$. In the presence of even an extremely thin layer of BaZrO$_3$, the fraction of C variant (labelled PZO-c) is seen to increase substantially with increasing thickness, whereas films of similar thickness grown directly on SrTiO$_3$ show a negligible fraction of C variant and a dominance of the A/B variant (labelled PZO-a).

5.4.4   Control of dislocation density

As seen in the previous section, by varying the thickness of the BaZrO$_3$ buffer layer, it is possible to vary the fraction of the A/B and the C domain variants. In the case of compressive misfit strains, the films prefer the A/B variants, whereas for tensile misfit strains, the C variant is preferred. Through these two conclusions, the change in the preferred variant from completely A/B to completely C, corresponding to the increasing thickness of the buffer layer from 0 for the former to 15nm for the latter, implies that the misfit strain for the PbZrO$_3$ layer changes from a heavily compressive (-5.8%) to a moderately tensile (1.2%) misfit strain with increasing thickness of the BaZrO$_3$ layer. Thus, on increasing the thickness of the buffer layer, since the magnitude of the compressive misfit strain decreases, the density of the misfit dislocations at the PbZrO$_3$ interface arising from this misfit strain is expected to decrease as well.

5.4.4.1   Observation of the dislocation cores

Using High-Resolution TEM imaging technique, the interface of films with varying thicknesses of the buffer layer were studied. The images were treated using a Fourier transform mask (see

Fig. 5.12) in order to obtain the periodicity of the atomic planes perpendicular to the interface. On magnification of the thus obtained images, the cores of the misfit dislocations lying at the interface were counted by marking the points of local disruption of lattice periodicity. This was repeated over multiple images in order to obtain good statistics. In this way, the linear density of the dislocations was determined for varying thicknesses of the buffer layer. Special attention was paid to avoid the inclusion of observed lattice distortion arising from imaging artefacts. This was achieved by counting the number of atomic planes from one side of the local lattice distortion starting from a distortion-free plane, and moving to the other side of the distortion till another distortion free plane is reached. This is carried out both above and below the local lattice distortion, and a dislocation in this region is accounted for only in the case of a disparity in the number of planes above and below the point of distortion (see Fig. 5.13).
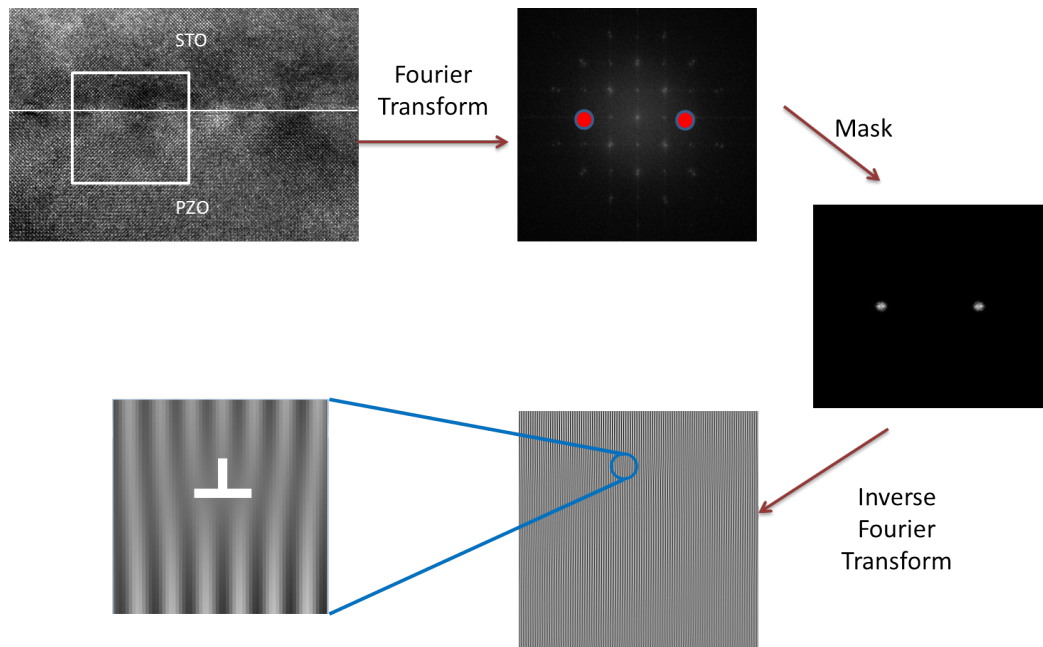
Figure 5.12: Schematic representing the processing of high resolution TEM images in order to obtain the linear dislocation density along the interface. A selected part of the interface with the substrate is chosen and passed through a Fourier transformation to obtain the frequencies of the lattice periodicity corresponding to different lattice planes. Using a mask and filtering only those frequencies corresponding to the planes perpendicular to the interface, and with a unit cell periodicity, an inverse Fourier transformation is applied to this masked image to obtain once again the lattice planes. Magnifying this image yields the location of the dislocation cores at points of disruption of local periodicity.

Using the above mentioned technique, misfit dislocations at the $PbZrO_3$-$BaZrO_3$ interface for films with varying thicknesses of the buffer layer were observed and quantified. Figure 5.14 presents some of the resulting images obtained for $PbZrO_3$ films grown on $BaZrO_3$ buffer layers measuring 1nm, 10nm, and 60nm. Though the interface is sharp between the layers, it is
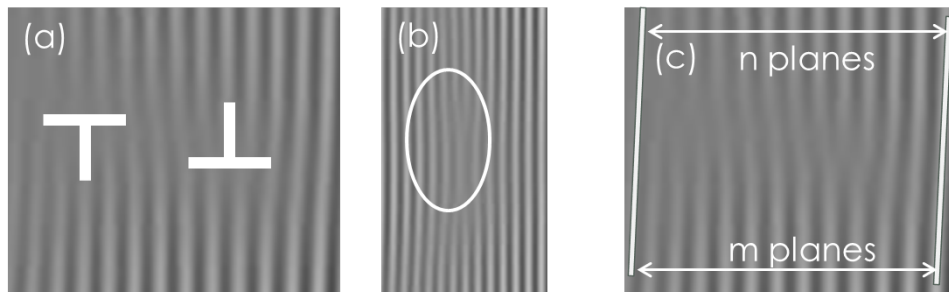
Figure 5.13: Examples of artefacts seen from the Inverse Fourier Transformed images: (a) Two opposite dislocations placed within a few nanometers away from each other, a configuration known to be energetically unfavourable. (b) Local aberration showing the disappearance and reapparance of a single plane. (c) Method of verification for the presence of a dislocation core. The number of atomic planes on either side of the predicted lattice distortion, is quantified above and below the distortion. If the number of planes remains the same (n=m), the distortion observed is an artefact, else, it is a dislocation.

clear from the images that the dislocations are not all found exactly along the interface. In the case of the interface between PbZrO$_3$ and SrTiO$_3$, the dislocations lie within the PbZrO$_3$ film but are located very close to the interface, whereas in the case of PbZrO$_3$ films grown on thicker BaZrO$_3$ films, the dislocations are seen to be located on either side of the interface, and within a few unit cells distance from the interface. Since these dislocations are all instrumental in the strain release at the interface of the PbZrO$_3$ film, all observed dislocations are included in the quantification. As is clear from the images, the density of the dislocations reduces heavily with increasing BaZrO$_3$ layer thickness. The separation between consecutive dislocations increases from around 4nm for a 1nm BaZrO$_3$ film to more than 40 nm for a PbZrO$_3$ film grown on a 60nm thick BaZrO$_3$ film, implying a decrease in the interfacial strain experienced by the PbZrO$_3$ layer. This reinforces the previous argument concerning the decrease in the interfacial strain with increasing thickness of the BaZrO$_3$ buffer layer.

5.4.4.2 Strain release from the misfit dislocations

To estimate the relaxation achieved by the formation of dislocations for varying misfit strains, it is required to understand the crystallographic nature of the dislocation, given by its Burger's vector and the associated glide plane. It was not possible to determine the Burger's vector from the existing HRTEM images due to insufficient resolution. Referring to previous studies done using TEM, it may be safely assumed that the burger's vector is aligned along the [110] direction of the cubic unit cell (dislocations form during the growth of the film in its cubic phase at high temperatures) [78]. The magnitude of the effective burgers vector (b$_{eff}$) is defined using the burgers vector of the dislocation (b) and λ as the angle between the stress plane and the glide plane (45° for an $\frac{a}{2}$<110>dislocation), as seen in eq. 5.7. The effective
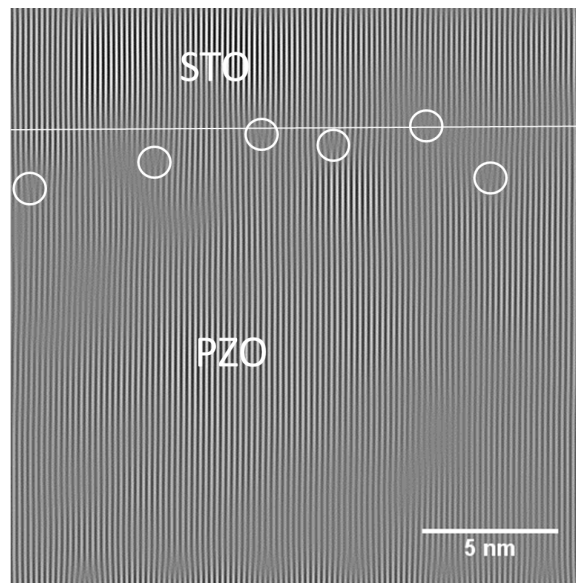
(a)
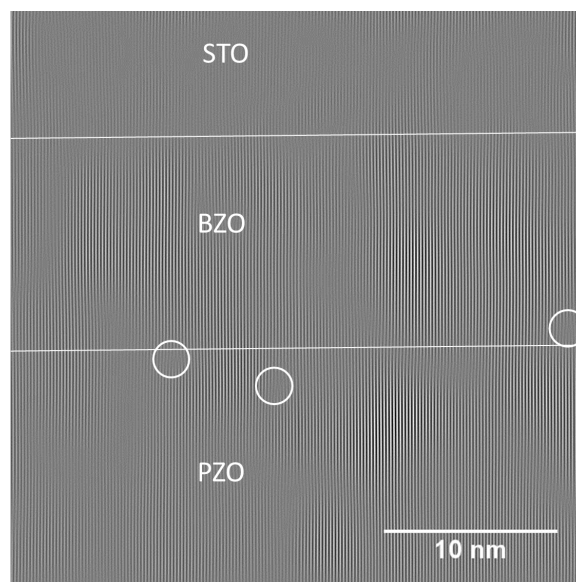
(b)
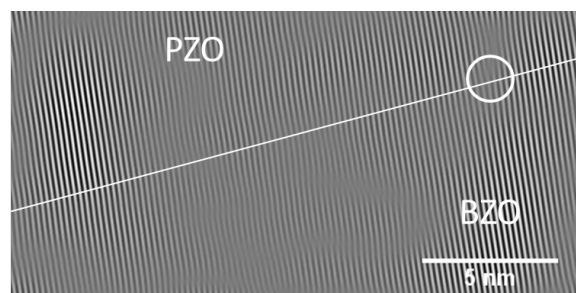
(c)

Figure 5.14: Typical inverse Fourier transform images obtained for films with buffer layer thicknesses of (a)1nm, (b) 15nm, (c) 60nm. The location of the misfit dislocations at the interface of the PbZrO$_3$ film with the BaZrO$_3$ buffer layer has been shown using the white circles.

79

burger's vector magnitude for the expected dislocations is, thus, equal to the lattice parameter of the film in the cubic phase.

$$b_{eff} = b\cos\lambda \tag{5.7}$$
$$b_{eff}^{<110>} = a\sqrt{2}\cos45^o = a \tag{5.8}$$

Using this value of the effective magnitude of the burgers vector, the strain released for a certain density of dislocations is calculated using the Eq. 5.9 (where s is the distance between two consecutive dislocation cores) [78]. The results of this calculation are presented in Table 5.4 and Fig.5.15. The strain released from the interface of PbZrO$_3$ grown on very thin layer of BaZrO$_3$ and from a very thick BaZrO$_3$ buffer layer are seen to be very close to the theoretical misfit values calculated from bulk lattice parameters (5.8% and 1.2% respectively), thus validating the predicted change in the interfacial strain from a change in the thickness of the buffer layer. The differences between the experimental values of the strain released and the theoretically predicted mismatch for the interface could be associated with the partial relaxation of the strain lattice mismatch through the formation of domains, which has not been accounted for in these approximations.

$$\delta_{\text{misfit}} = \frac{b}{2s} \tag{5.9}$$

BaZrO$_3$ thickness (nm)	s (nm)	Linear Dislocation density(/100 nm)	δ_{misfit} (%)
1	3.5	29	5.9
7	9.8	10	2.1
15	14.7	7	1.4
60	42	2	0.5

Table 5.4: Tabulation of linear dislocation density and corresponding misfit strain release with varying thickness of buffer layer for b$_{eff}$= 0.411nm

These results promote the use of BaZrO$_3$ as a buffer layer not just in its relaxed state, but also in its partially relaxed state. For any material, by determining the trend seen in Fig. 5.15, the interfacial strain for the following layer can be controlled through a precise control on the thickness of the BaZrO$_3$. To the best of the author's knowledge, such continous tuning of interfacial strain using a single perovskite material has been undocumented.
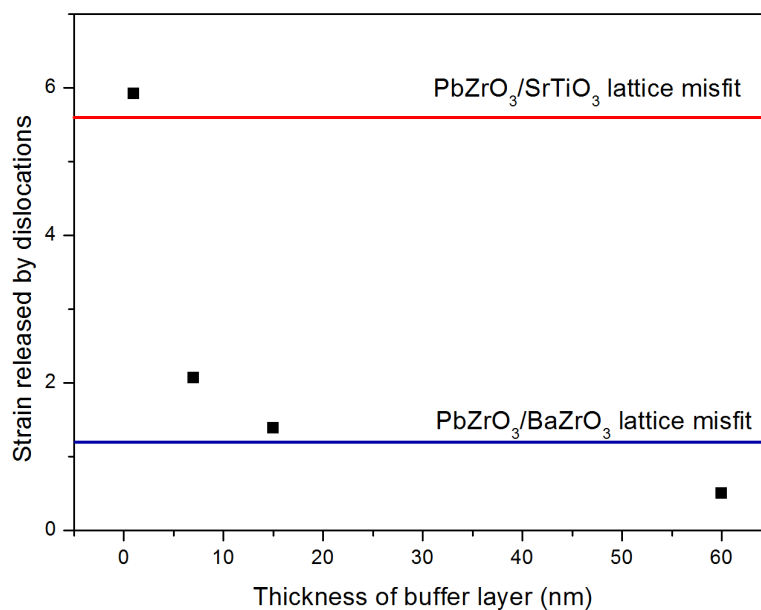
Figure 5.15: The strain released through the formation of dislocations at the PbZrO$_3$/BaZrO$_3$ interface for varying thicknesses of BaZrO$_3$. The values of the relaxation for an extremely thin and an extremely thick buffer layer are comparable to the predicted lattice misfit at the interface as calculated from the bulk lattice parameters.

5.4.4.3 Threading dislocations

As mentioned previously, in cases of high lattice mismatch, the critical thickness for the formation of dislocations in thin films reduces drastically, from 10nm for 1% mismatch strain to less than one unit cell for strains higher than 2 %. Since all of the films discussed above have large lattice mismatch with the substrate, the elastic energy needed for the formation of misfit dislocations is already quite large even at very low film thicknesses resulting in the formation of misfit dislocations early into the growth of the film, as seen previously for other perovskite thin films with high lattice mismatch[75]. In the cross-sectional TEM images obtained for the films deposited on various thicknesses of the BaZrO$_3$ buffer layer, no dependance of the density of threading dislocation on the misfit strain was observed, with the distance between consecutive threading dislocations varying between 20-30nm., as seen in Fig. 5.16.

The origin of such dislocations is often related to two major sources: (a) extension of existing dislocations from the substrates/buffer layers into the film, or (b) formation of dislocation half loops at the film surface which subsequently climb/glide down towards the interface. Given the high density of threading dislocations observed in the current study, and the low density of dislocations present in commercially available substrates, the latter of the two mechanisms is more likely to be a feasible explanation for the origin of the dislocations. It has been previously shown [146, 147] that in cases of growth of thin films from a vapour phase, depending on

(a)

(b)

(c)
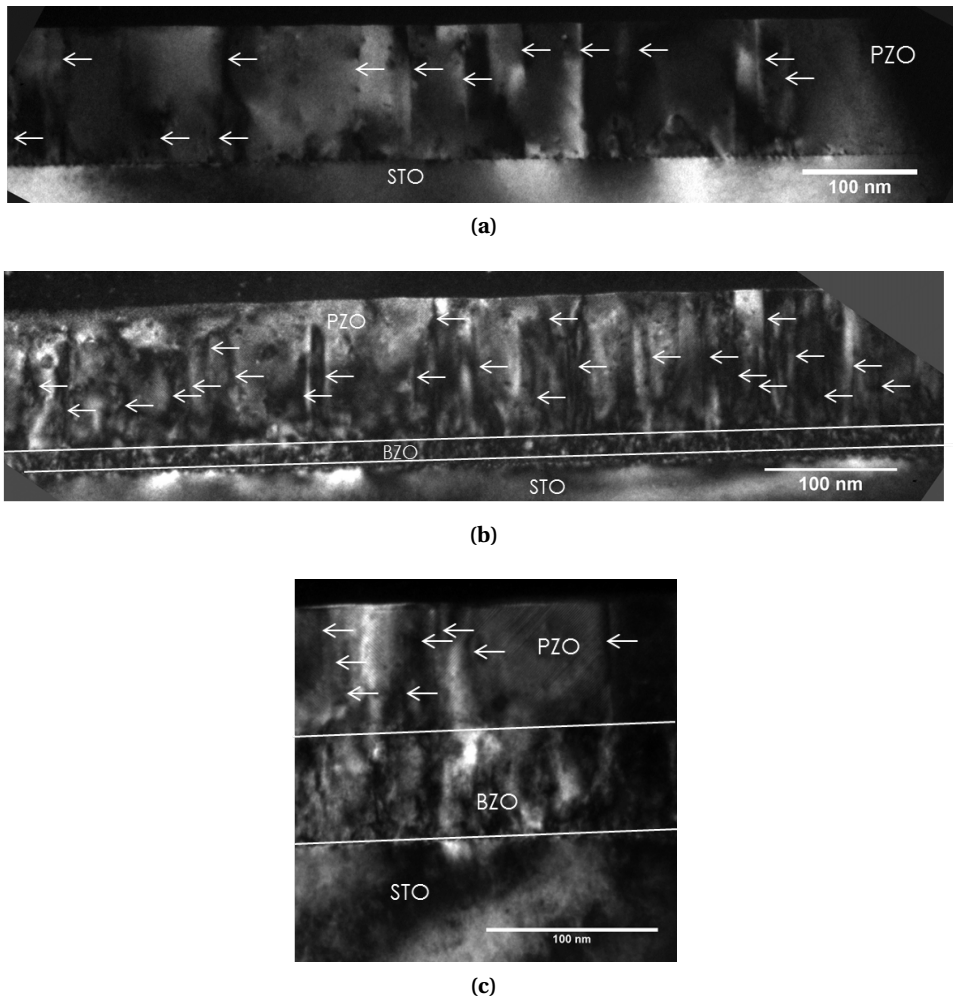
Figure 5.16: Threading dislocations marked in thin films of PbZrO$_3$ grown on (a)1 nm thick BaZrO$_3$ film (b) 10nm. BaZrO$_3$ film, and (c) 60nm BaZrO$_3$ film. There seems to be no systematic change in the threading dislocation density observed with the misfit strain. It is associated with the chaotic growth mode of PbZrO$_3$.

the growth mode, the formation of threading dislocations may or may not be supported. It was shown that in the case of a 2-D growth mode, the presence of multiple clusters for the nucleation can, on coalescing with each other, result in the formation of line defects like dislocations or planar defects like twin boundaries. Even in the case of 3-D island growth mode, the coalesence of epitaxial islands can result in the formation of such defects.

In the current study, as is observed from the topography of the surface through the AFM images, no presence of island growth has been observed, and the films seem to follow the terraced surface structure corresponding to that of the substrate. This suggests that during the growth of the thin films, the growth mode consists of the formation of 2-dimensional clusters which grow to coalesce with each other to form the dislocation half loops, which later glide

and/or climb down towards the interface to form the misfit dislocations, while their threading segments remain along the entire length of the film. Also observed in the TEM images are threading dislocations which arise from the surface of the sample and end abruptly within the film without reaching the lower interface, implying that the coalescence of islands occurs during all stages of the growth and not only during the initial stages.

5.5 Conclusions

Epitaxial thin films of $PbZrO_3$ were grown on $SrTiO_3$ substrates with or without the use of $BaZrO_3$ as a buffer layer to moderate the high misfit strain between the substrate and the $PbZrO_3$ film. The epitaxy in these films was seen to be cube-on-cube and two domain variants were distinguished corresponding to out-of-plane orientations parallel to the {210} and {001} directions of the orthorhombic axis. The former is seen to be favoured in the case of compressive misfit strains whereas the latter is favoured in the case of tensile misfit strains and is heavily stabilised by the presence of $BaZrO_3$ even before the complete relaxation of the latter. This observation is explained using the energetics associated with the elastic strain corresponding to each domain variant. By varying the thickness of the $BaZrO_3$ buffer layer, the misfit strain experienced by the $PbZrO_3$ film is modulated, and thus a control over the misfit dislocation density is achieved as well, while controlling alongside the relative fractions of the domain variants in the thin film. The use of a single perovskite material as a buffer layer to provide for a range of interfacial strains has thus been achieved in this study.

6 Antiferroelectricity in thin films

The epitaxial PbZrO$_3$ films with controlled misfit dislocation density (see Chapter 5) are characterised electrically. Typical hysteretic behaviour expected from antiferroelectric thin films is obtained through the measurement of permittivity and polarisation as a function of external bias, verifying the persistance of antiferroelectric behaviour despite the interfacial strain. The formation of a passive dielectric layer at the film interface from the high density of defects is observed. An estimation of the ferroelectric phase transition temperature is given through the complimentary use of dielectric permittivity, X-Ray Diffraction and Raman Spectroscopy analyses conducted as a function of temperature.

The two-mode model previously used to describe antiferroelectricity in Chapter 4, allows for the easy swapping of the relative positions of the ferroelectric and structural instabilities, potentially causing the onset of the ferroelectric phase transition before the structural phase transition, thus resulting in a ferroelectic material instead of an antiferroelectric. This swapping can be achieved through a minor change in the chemical composition (as seen through even small amounts of doping by Ti [39]) or the application of hydrostatic pressure. Also seen previously are cases of epitaxial strain resulting in the appearance of ferroelectric phases in thin films of PbZrO$_3$ [82]. To this effect, the epitaxial films of PbZrO$_3$ with high interfacial strain are examined for their antiferroelectric behaviour through their dielectric responses and their phase transition.

6.1 Dielectric Characterisation

6.1.1 Sample preparation and experimental details

Thin films of $PbZrO_3$ deposited with different thicknesses of $BaZrO_3$ buffer layer were grown on (0.1%) Nb-doped $SrTiO_3$ substrates as described in Chapter 5. Pt-top electrodes of $100\mu m$ and $200\mu m$ radii were deposited using room-temperature sputtering technique and annealed at 300^oC. Given the conductive nature of the Nb-doped $SrTiO_3$ substrates, they served directly as bottom electrode for the parallel plate capacitor formed by the $PbZrO_3$ and $BaZrO_3$ layers between the Pt-electrode and the substrate. For all dielectric characterisation techniques, the field was applied to the bottom electrode and the ground was connected to the top electrode.

6.1.2 Capacitance vs Field Measurements

Using small-signal measurement techniques, the capacitance of the antiferroelectric thin film was studied as a function of the applied external field. From the capacitance, the permittivity of the film is recalculated using the following equation:

$$C = \epsilon_r \epsilon_o \frac{A}{d} \tag{6.1}$$

where ϵ_r and ϵ_o are permittivities of the film and of free space, A is the area of the electrode and d is the film thickness. The real (ϵ_r^r) and imaginary contributions (ϵ_r^i) to the permittivity are seperated and the imaginary contribution is presented as a loss tangent, calculated as follows:

$$\tan\delta \quad = \quad \frac{\epsilon_r^i}{\epsilon_r^r} \tag{6.2}$$

Shown in Fig. 6.1(a) is the Permittivity-Field (C-E) response from a 100nm thick $PbZrO_3$ film grown on a 5nm $BaZrO_3$ buffer layer. The film is heavily conductive under the application of negative field to the bottom electrode, as seen by the drastic increase in the permittivity (representative of heavy charge building in the film), and from the very large values for the loss tangent. Contrarily, on the application of a positive field to the bottom electrode, the film is seen to be well insulating with minimal losses, showing the typical double peaks associated with the jump of permittivity at the two coercive fields forming one half of the double hysteresis loop. Similar C-E analysis was carried out on a 50nm thick $BaZrO_3$ film. As seen in Fig. 6.1(b), the $BaZrO_3$ film showed as well a heavily conductive behaviour on the application of negative

fields, while remaining a good instulator on the application of positive fields. The source of the loss in both the films, thus, has to be of a similar origin, potentially arising from the high concentration of defects such as threading dislocations from the metastable growth conditions and high epitaxial stress associated with both the films. Thus, it seems that the high losses are not related to the instabilities or the antiferroelectricity of the $PbZrO_3$ layer. To avoid any interference from the charges accumulating in the film during the application of high negative fields henceforth, only pseudo-unipolar analyses, i.e. measurements avoiding very high negative fields, are discussed. Figure 6.1 (c) shows the behaviour of the same $PbZrO_3$ film under pseudo-unipolar conditions, with the two peaks corresponding to the two coercive fields associated with one half of the antiferroelectric double hysteresis loop. The two peak positions are almost invariant with the frequency of the signal applied (between 1kHz and 100kHz), upto within 25kV/cm.

The position of the two peaks in the C-E analysis were measured as a function of temperature, shown in Fig. 6.2. The coercive fields are seen to decrease with increasing temperature and similar behaviour is seen for the width of the hysteresis as well as the center of the hysteretic behaviour, implying proximity to the actual structural phase transition temperature of the film at 460K. Owing to experimental restrictions, higher temperatures could not be used for the precise determination of the structural phase transition, coinciding with the disappearance of the peaks.

Alongside, the peak height is seen to decrease with increasing temperature, shown in Fig. 6.2(c), with the appearance of an extra peak close to -100kV/cm at 450K. This bump possibly arises from the reverse peak of the other loop associated with the negative fields, which in the current case is masked by the heavy losses, i.e. the two hysteresis loops are possibly merging into one another with increasing temperature. It can also be confirmed from these observations that the phase transition in these films occurs above 450K. To recall, in the case of bulk single crystals, the phase transition is seen around 505-510K [8, 27].

6.1.3 Polarisation-Field Hysteresis measurements

Polarisation-field hysteresis measurements (P-V loops) were carried out using commercial AIXACCT equipment, through a large signal technique. Deriving from the C-E analysis results discussed previously, the application of negative fields to the bottom electrode is avoided and all measurements are carried out only for positive fields applied to the bottom electrode. The net polarisation in a $PbZrO_3$ film, calculated from the integration of the current, as a function of increasing bias is shown in Fig.6.3(a) where no distinct hysteretic feature is observed. On

(a)

(b)

(c)
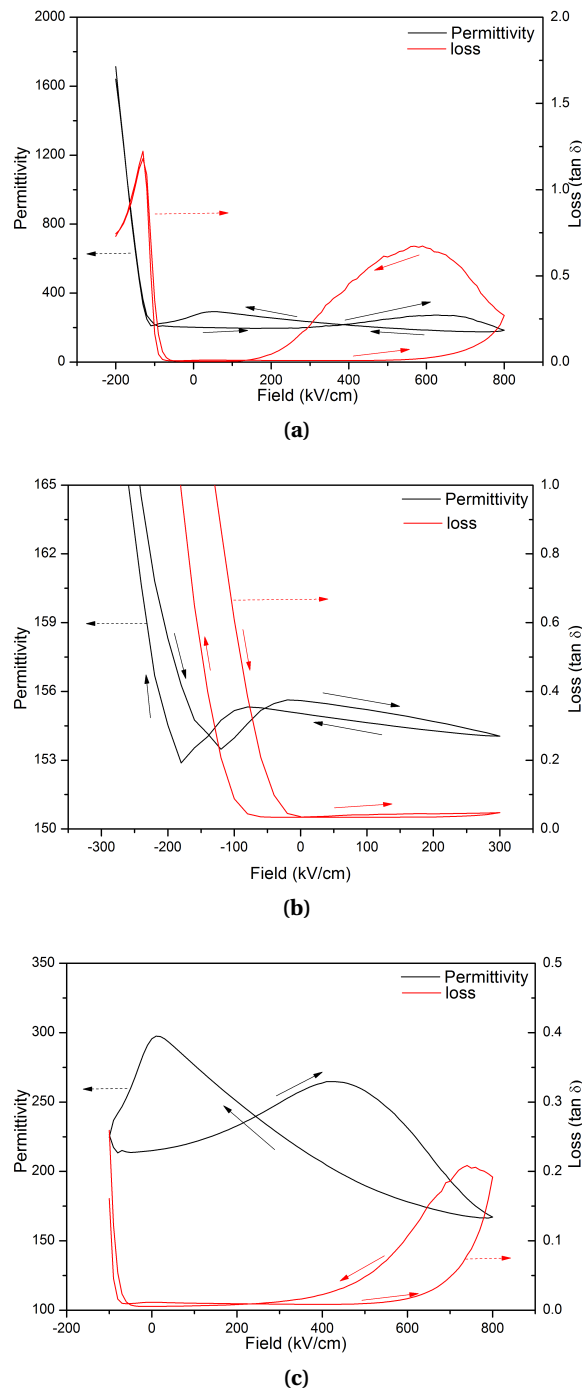
Figure 6.1: Variation in the permittivity of (a) 100nm thick PbZrO$_3$ thin film with 5nm BaZrO$_3$ buffer layer and (b) 50nm thick BaZrO$_3$ thin film with the application of an external field (to the bottom electrode). Both films are seen to be well insulating for positive fields, while at negative fields, they are seen to have heavy losses, suggesting a similar origin for the losses.(c)Pseudo-unipolar measurements on the same PbZrO$_3$ film showing the two peaks corresponding to the two coercive fields associated with one half of the typical antiferroelectric double hysteresis loop. The direction of the measurement is shown by the arrows (the dashed arrows point towards the coresponding y-axis) and henceforth, the higher peak is designated as the forward peak, and the lower peak as the reverse peak.

(a)

(b)

(c)
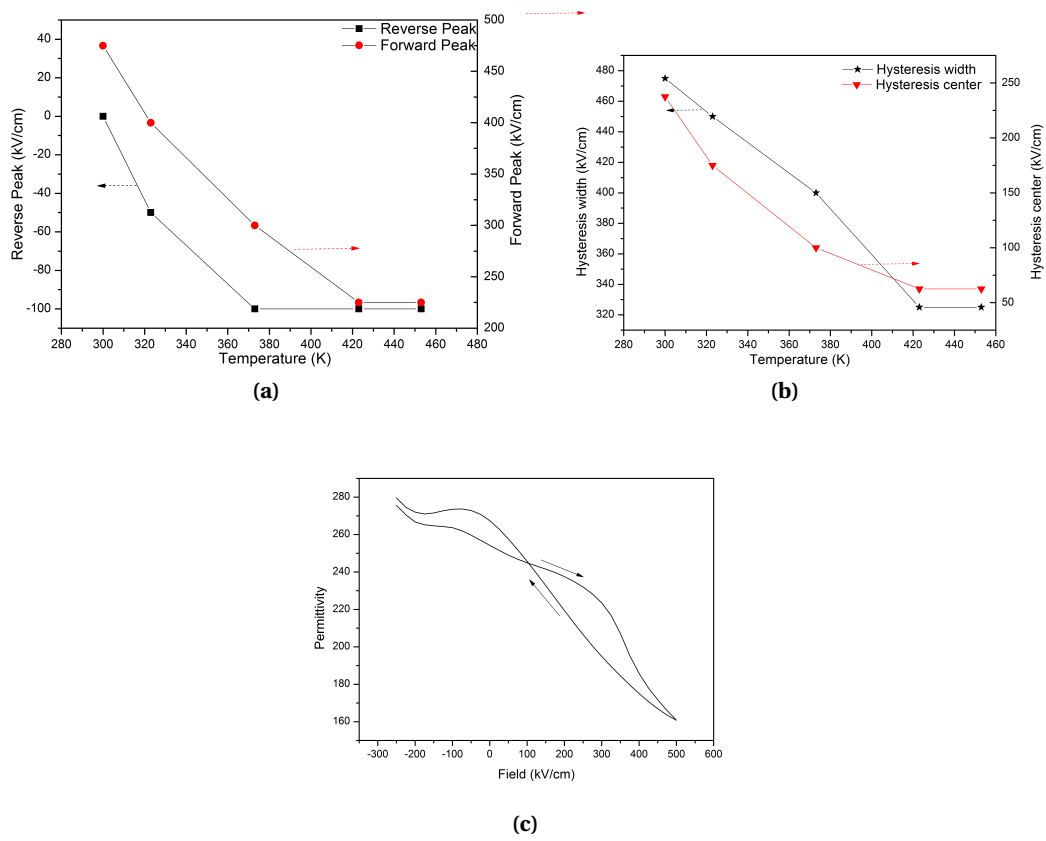
Figure 6.2: Variation of the positions of the (a) forward and the reverse peaks (b) hysteresis width and center of hysteretic behaviour, associated with the positive coercive field, as a function of temperature. With increased measuring temperature, the coercive field decreases at a higher proximity to the structural phase transition temperature.(c) The C-E response from the PbZrO$_3$ film at 450K, showing the appearance of an extra peak at -100kV/cm and potentially implying the merging of the two halves of the double hysteresis loops.

the other hand, the current measured as a function of the bias applied, as shown in Fig. 6.3(b), shows fairly well defined peaks at certain values of the electric field, against an almost constant background current. In leaky films, the background current increases with increasing applied voltage, whereas in these samples, the background current remains constant upto very high fields. The background current hence does not arise out of leakage. Instead, when decreasing applied bias, the background current changes sign while still retaining the same magnitude for all applied voltages. This effect arises out of trapped charges in the thin film, as proven by the change in the sign of the background current for increasing and decreasing applied voltages. The amplitude of the peaks does not exceed the background current, and for this reason, the expected jump in the polarisation in Fig. 6.3(a) remains buried under the effect of the trapped charges. Nevertheless, these peaks are signatures of the coercive fields associated with the positive half of the double hysteresis loop.
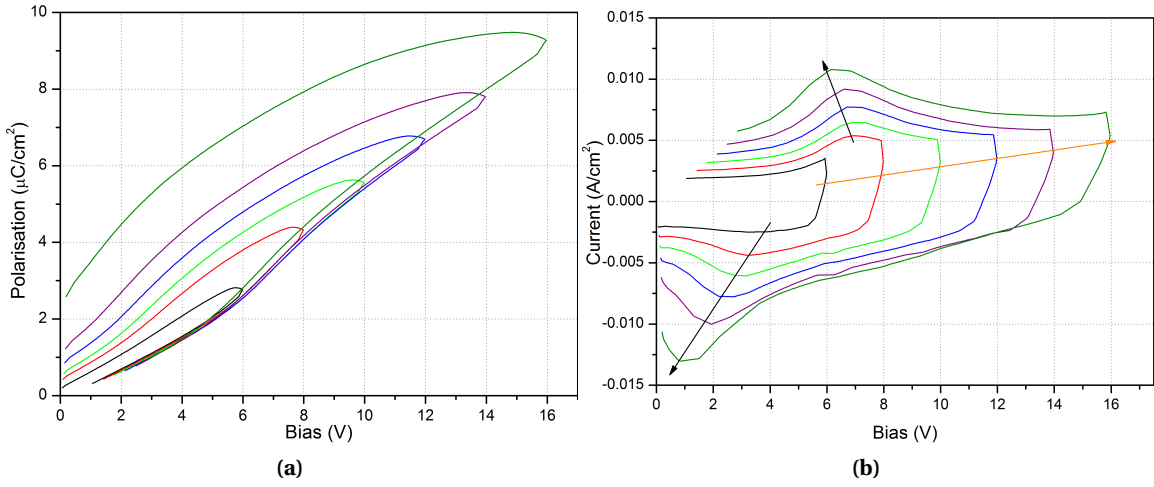
Figure 6.3: P-V measurements for 100nm PbZrO$_3$ film. (a) Calculated polarisation (from integrated current) as a function of the applied bias. No particular hysteretic behaviour is directly observed. (b) Current density as a function of the applied bias. The constant background current is a sign of the trapped charges and the peaks correspond to the coercive field associated with the hysteresis. There is an observed dependance of the peak position on the maximum applied field

Also remarkable in Fig. 6.3(b) is the shift in the position of the peak as a function of the maximum bias applied. This is interpreted as a consequence of charge injection into a passive dielectric layer at the electrode interface. The dielectric layer in the current scenario could correspond to the high misfit dislocation density interface between the film and the substrate. Following Refs. [24, 148], the potential across a system (E) with a film (of thickness h) and a passive dielectric layer (of thickness d) in series is given by

$$dE_d + hE_f = (d+h)E \tag{6.3}$$

where E$_f$ is the electric field experienced by the film and E$_d$ is the field in the passive layer. This can be rearranged to result in the following equation for E$_f$:

$$E_f = E - \frac{d}{h}E_d \tag{6.4}$$

The field drop across the dielectric layer with a dielectric constant κ_d can be estimated using the contribution of charges from the polarisation in the film (P$_f$) and from the charge injected

(σ) through the equation:

$$E_d = \frac{P_f - \sigma}{\epsilon_0 \kappa_d} \tag{6.5}$$

For the field in the film to attain a value equal to the coercive field (E_c), i.e. $E_f = E_c$, the necessary external field is given by

$$E = E_c + \frac{d}{h} E_d \tag{6.6}$$

$$E = E_c + \frac{d P_f}{\epsilon_0 \kappa_d h} - \frac{d \sigma}{\epsilon_0 \kappa_d h} \tag{6.7}$$

By increasing the maximum applied bias for each measurement, the amount of the charge injected into the passive dielectric layer (σ) increases for every subsequent measurement. As a result, from Eq. 6.7, the necessary field applied to the whole system to reach the coercive field across the film decreases. Similarly, by decreasing the maximum applied bias for each measurement, the charges accumulated in the passive dielectric layer are depleted for each subsequential measurement and as a consequence of Eq.6.7, the required necessary field to reach the coercive field for the film increases. Figure 6.4(a) shows the trace of the forward peak position and the peak current as a function of the maximum applied bias. On measuring the P-V loops while increasing the maximum bias applied from 8V to 16V and then decreasing it back to 8V, the peak position and the peak current for the forward (and the reverse peak, not shown here) are seen to decrease and increase respectively, correlating well with the model described above. It is noted that while decreasing the maximum applied bias the applied field necessary for reaching the coercive field does not exactly follow the trend observed during the measurements conducted while increasing the maximum applied bias. This could be because of the incomplete depletion of the charges accumulated in the passive layer during the measurements undertaken while decreasing maximum applied bias. On varying the speed of the large signal measurement, for lower measurement speeds (lower frequencies) more charges accumulate in the passive layer due to longer measuring times, resulting in larger peak currents, as shown in Fig. 6.4(b), which further solidifies the proposed model of a passive dielectric layer at the electrode interface.

The effect of trapped charges is not restricted singularly to this film, but extends also to films containing $BaZrO_3$ buffer layers. Similar traits with comparable magnitudes of peak currents and peak positions were observed for all the films irrespective of the buffer layer thickness. The
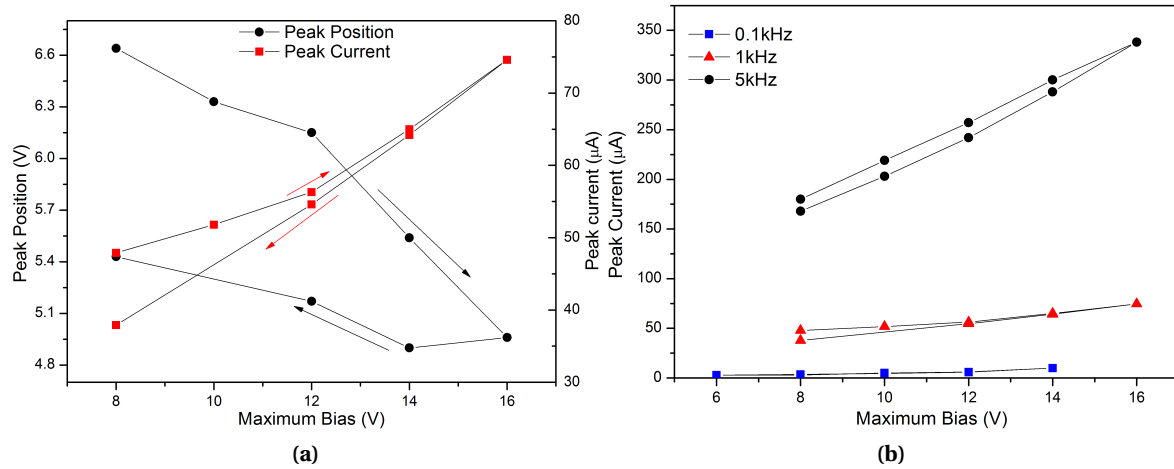
Figure 6.4: (a)The peak position and the peak current for forward switching phenomena plotted as a function of maximum bias applied. The P-V measurements were repeated by increasing the maximum applied bias from 8V to 16V and decreasing it back to 8V (shown by arrows). Measurements were carried out on a 100nm PbZrO$_3$ film with 1kHz measuring rate. On increasing the maximum applied bias for subsequent measurements, due to the accumulation of charges in a passive dielectric layer at the electrode-film interface, the necessary external field for the hysteresis decreases. Accordingly, on decreasing the maximum applied bias for subsequent measurements, the necessary field for the coercive field increases. The latter behaviour does not completely follow the former potentially because of incomplete charge depletion from the film-substrate interface. (b)The peak current in 100nm thick PbZrO$_3$ film for forward switching plotted as a function of maximum bias applied for various measuring rates (0.1-5kHz). For lower measuring rates (i.e. longer measuring times), due to larger charge collection in the passive layer at the film-substrate interface, the measured current increases.

source of the passive layer may thus be traced back to the heavily strained interface between the substrate and the film (either BaZrO$_3$ for systems including the buffer layer, or PbZrO$_3$ in the case of systems without buffer layer).

6.2   Estimation of Phase Transition temperature

In the presence of an externally imposed stress, such as epitaxial stress in thin films, the ferroelectric transition temperatures is often shifted. Temperature-phase diagrams are used to describe the relative stability of the phases at different temperatures under different conditions of epitaxial strain [149]. In the current study, the epitaxial thin films of PbZrO$_3$ have various magnitudes of interfacial strain, which is released very quickly through the formation of defects such as dislocations, leading to complete relaxation of the epitaxial stress. Since the bulk of the film is under relaxed conditions, the phase transition temperature would be expected to be comparable to that previously observed in single crystals and ceramics, namely around 510K [8, 27]. The phase transition is observed through a combination of X-Ray, Raman and permittivity measurements conducted as a function of temperature. The X-Ray and

Figure 6.5: (a)Dielectric Permittivity and (b) corresponding losses measured as a function of temperature for a signal of 1V applied at 1kHz for a 100nm thick $PbZrO_3$ film with a 5nm thick $BaZrO_3$ buffer layer grown on Nb-doped $SrTiO_3$ substrate. The dielectric permittivity peak is seen to saturate starting ~480K and descends above ~510K.

the Raman studies were conducted by Dr. Brahim Dkhil and Dr. Pascale Gemeiner at Ecole Centrale, Paris, and were analysed by the author in collaboration with Prof. Dr. Joe Trodahl, Victoria University of Wellington, New Zealand.

6.2.1 Permittivity vs. temperature measurements

The capacitance was measured as a function of temperature using the setup described in Chapter 3, to estimate the phase transition temperature from the dielectric anomaly. Shown in Fig. 6.5 are the variations in the dielectric permittivity and the corresponding losses as a function of temperature, for both heating and cooling measurements on a 100nm thick $PbZrO_3$ film with a 5nm $BaZrO_3$ buffer layer. One observes minimal hysteresis between the heating and the cooling experiments. The phase transition is seen to be diffused with a flat peak in permittivity lying between 480K and 510K, thus making it difficult to predict the exact temperature for the expected first order phase transition. Similar behaviour was observed for all films irrespective of the thickness of the buffer layer. Such diffused phase transitions have previously been observed for epitaxial $BaTiO_3$ films [150], where the reason for the observed smearing of the transition was associated with the ferroelastic strain developed in the material on crossing the phase transition. The estimation of the Curie Temperature through the application of Curie-Weiss law to the permittivity at temperatures above the phase transition was not possible due to increased losses and electrode contact problems at higher temperatures.

6.2.2 Temperature variant X-Ray Diffraction

For all discussion in this section concerning the domain orientations, the pseudotetragonal axes described in Chapter 5 are used, unless mentioned otherwise. Using the $\theta - 2\theta$ scan as shown previously in Fig. 5.8, the positions of the bragg peaks corresponding to the {002} planes of the A and C domain variants are measured as a function of temperature. Three different films are analysed: 100nm $PbZrO_3$ film with 1nm thick $BaZrO_3$ buffer layer (film A), 50nm thick $PbZrO_3$ film without a buffer layer (film B), and 100nm thick $PbZrO_3$ film grown on 15nm thick buffer layer (film C). Borrowing from Chapter 5 the dependance of the preferred domain orientation on the buffer layer thickness, film A has mixed A and C domains, film B has uniquely A domains, and film C has uniquely C domains.

Figure 6.6 shows the temperature variant XRD analyses for film A. It is observed that at ~465K, the 'C' domains in the film disappear, accompanied by a jump in the lattice constant (seen in Fig. 6.6(b)). One also observes a change in the slope of the lattice constant w.r.t. the temperature after ~505K , corresponding to the temperature of the phase transition previously observed for single crystals and ceramics of $PbZrO_3$. Similar results were observed for the films B and C, with a lattice parameter discontinuity at ~465K and with a change in the slope at ~510K as seen in Fig. 6.6 (c) and (d). Since the phase transition in $PbZrO_3$ is commonly first order, a jump in the the lattice parameter is a more reliable sign of the phase transition, and the phase transition can be said to occur around 460K.

6.2.3 Temperature variant Raman Spectroscopy

As a confirmation to the above obtained estimates for the phase transition temperature, Raman spectroscopy was carried out on the 100nm films of $PbZrO_3$ with 1nm $BaZrO_3$ and 15nm $BaZrO_3$ buffer layers, shown in Fig. 6.7 (a) and (b) respectively. The peak observed at ~125cm^{-1} corresponds to the Σ_{25} mode, related to the antiparallel lead displacements in $PbZrO_3$ [52]. The temperature at which this mode disappears would, thus, suggest the temperature of the structural phase transition. In this case, for both the films, this mode is seen to reduce to within the background signal between 470K and 480K, which corroborates well with the previously obtained estimates from the permittivity measurements as well as the temperature variant X-Ray diffraction measurements.

(a)

(b)

(c)

(d)
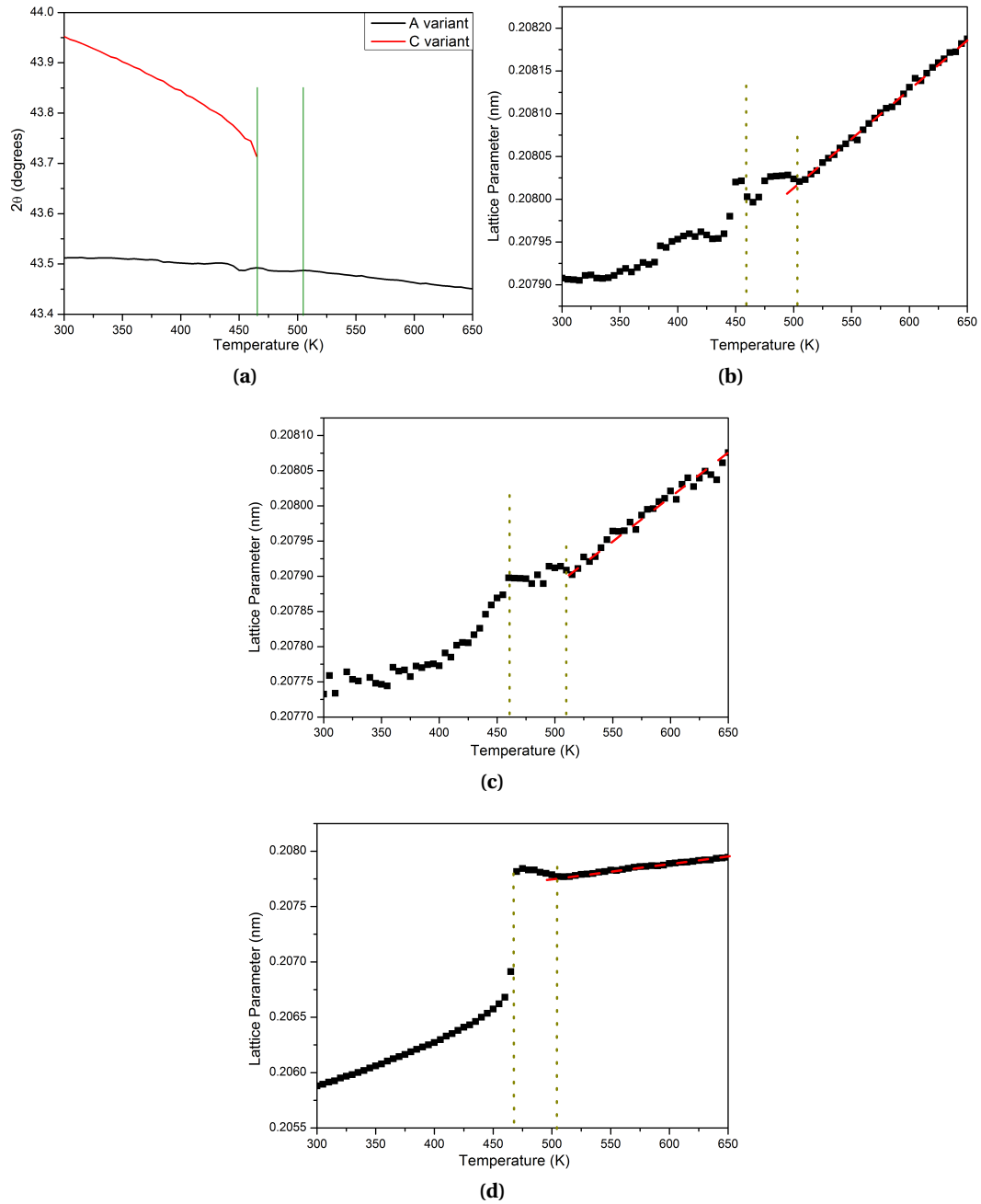
Figure 6.6: Temperature variant X-Ray Diffraction measurements on PbZrO$_3$ thin films. (a) Variation of the peak position for the A and the C domains with temperature for a 100nm thick film with 1nm thick BaZrO$_3$ buffer layer. The C domains disappear around 465K. At around 505K, the slope of the lattice constant with temperature changes. (b) The lattice parameter of the A domain for the same film as in (a), clearly showing a jump at 465K and a change in slope at 505K. (c) The lattice parameter of the A domain in a 50nm PbZrO$_3$ film with no buffer layer, showing a discontinuity around 460K and a change in slope at 510K. (d) The lattice parameter of the C domain in a 100nm PbZrO$_3$ film with 15nm buffer layer, showing a discontinuity in the lattice constant at 470K, and a change in slope at 505K. The observed transition temperature for all films are characterised by a discontinuity in the lattice constant at 465-470K. The change in the out-of-plane lattice constant for the C domains during the transition to the paraelectric phase is larger than the corresponding value for the A domains. Hence, the former shows a larger jump than the latter.

(a)

(b)
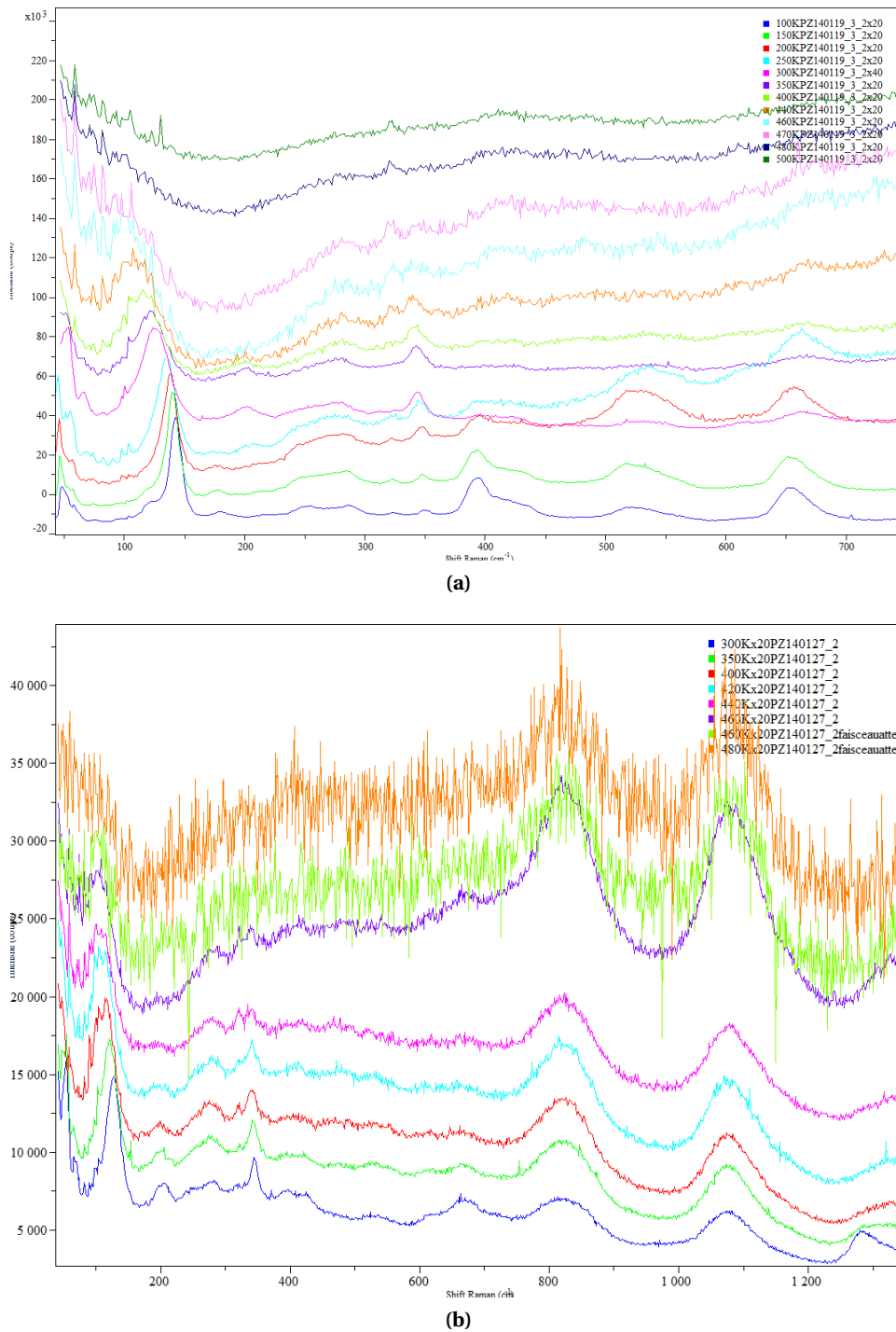
Figure 6.7: The Raman scattering spectra obtained from 100nm PbZrO$_3$ film with (a) 1nm BaZrO$_3$ and (b) 15nm BaZrO$_3$ buffer layer. The line at 120cm^{-1} at 300K corresponds to mode controlling the antiparallel Pb displacements. The temperature at which this mode goes to 0 is adjudged as the structural phase transition temperature, in both cases seen to be ~470K.

6.2.4 Discussion

Comparing the transition temperature observed through different means as shown above, it can be safely concluded that there exists a lowering of the phase transition temperature by at least 30K in all thin films of $PbZrO_3$, irrespective of the interfacial strain. The perceived independance of the transition temperature with the interfacial strain is not surprising since the bulk of the film is in any case completely relaxed. Thin films of $BaTiO_3$ with 1.7% strain have shown a shift of upto 500K in their transition temperature[151], whereas for thin films of $SrTiO_3$, a shift in the transition temperature of upto 250K was observed with 1 % epitaxial strain [152].Though theoretically it is possible to analyse the effect of strain on the phase stability and transition temperature in $PbZrO_3$, the lack of sufficient data for the coefficients in the Landau expansion prevents its completion. Nonetheless, using the previously quoted examples as guidelines, one could imagine that the 30K lowering observed in these $PbZrO_3$ films could correspond to a low (<0.1%) residual strain in the film, a claim that can be fulfilled by residual thermal strain in the film while cooling down from growth temperature.

6.3 Effect of competing instabilities

In Chapter 4 the antiferroelectricity in $PbZrO_3$ was described using a two-mode model consisting of two competing order parameters. The behaviour of a system with competing instabilities in the presence of an electrical field was studied previously [56] using a free energy model consisting of one polar and one non-polar order parameter. Through the analysis of the coefficients in the free energy expansion, the response of the material to external applied fields and the dielectric properties as a function of temperature were studied, resulting in the demonstration of a variety of ferroelectric and antiferroelectric behaviour. Through the observations presented in the chapter for the thin films of $PbZrO_3$, some information can be derived about the coupling between the competing instabilities present in the system.

The double hysteresis loops observed both from the C-E and the P-V measurements are described in this model through a field-induced first order phase transition into a state where the structural order parameter is reduced to zero. This scenario neither requires nor insists on the appearance of a ferroelectric order parameter at this field induced phase transition. This implies that the conventional explanation of the "field-induced ferroelectric phase transition" is not adequate for the description of the double hysteresis loops. In Fig.6.2, it is observed that the values for the critical field for the onset of the phase transition from the C-E measurements diverge with decreasing temperature, i.e. the width of the hysteresis, as well as the center

of the hysteresis increase with decreasing temperature. This corresponds to the 'T' type of behaviour previously described by Balashova and Tagantsev [56]. The 'T' type behaviour insists on a cusp-like dielectric anomaly of the phase transition, and the phase transition observed in the thin films as seen in Fig. 6.5 though diffused, corresponds more closely to a cusp-like behaviour, rather than to a discontinuity or a change in slope. The association of the dielectric responses of the film with a 'T' type behaviour suggests a heavy repulsive coupling between the structural and the ferroelectric order parameters resulting in the suppression of the ferroelectric order parameter on the onset of the structural order parameter, which describes precisely the interactions observed experimentally in Chapter 4.

6.4   Conclusions

The measurement of the polarisation versus the applied field for the thin films showed the presence of charge trapping from a passive dielectric layer, potentially located at the highly strained interface between the film and the substrate. Measurement of the permittivity of $PbZrO_3$ films with external bias yields the typical 2 peak behaviour for unipolar measurements. These peaks are indicators of the coercive fields associated with one half of the double hysteresis, and their position is seen to move closer to lower values with increasing measurement temperature, pointing to the occurence of the phase transition only above 460K. Using a two mode instability model [56], the double hysteresis observed in antiferroelectric thin films can be explained without invoking a field induced 'ferroelectric' phase, but instead by interpreting the hysteresis as a 'field induced lowering' of the structural phase transition. Additionally, the variation of the coercive field with temperature suggests a heavy repulsive coupling between the structural and the ferroelectric order parameters, with the onset of the former suppressing the appearance of the latter, as predicted in Chapter 4. Complementary analyses of the phase transition temperature through permittivity, X-Ray Diffraction and Raman spectroscopy measurements as a function of temperature predicts the onset of the phase transition at ~480K, indicating a lowering of about 30K when compared to single crystals or ceramics. This can be related to the presence of residual thermal strain in the thin film (<0.1%) on cooling from the growth temperature.

7 Antiphase boundaries in thin films of PbZrO$_3$ as ferroelectric structures

The suppression of the primary order parameter associated with the stabilisation of the antiferroelectric phase results in the local appearance of ferroelectric properties. The conditions for the reduction of the primary order parameter in PbZrO$_3$ are presented in this chapter. It is followed by the observations of the domains and the domain boundaries in thin films of PbZrO$_3$ using advanced Transmission Electron Microscopy techniques. The so-called π walls are seen to have an in-built polarity, potentially containing localised ferroelectric behaviour. The interactions of translational and orientational boundaries with defects are observed as well.

7.1 Ferroelectricity as a consequence of competing instabilities

Previously in Section 4.6, a two mode model with competing interactions, with the free energy constructed using Eq. 7.1, was employed to explain the origin of antiferroelectricity in PbZrO$_3$. A large value of the coefficient δ ensures that on the onset of the structural phase transition, the ferroelectric phase transition is subdued, i.e. a finite value of the primary structrual order parameter suppresses the ferroelectric order parameter.

$$F(P,\xi) = \frac{1}{2}\alpha(T - T_0)P^2 + \frac{1}{2}\delta_{P1}(P_1^2 + P_2^2)\rho^2 + \frac{1}{2}\delta_{P3}P_3^2\rho^2 + F_A(\xi) \tag{7.1}$$

Analogically, it can be said that the absence of the structural order parameter would result in a localised ferroelectric behaviour. This can be realised using the simplest type of ferroic domain wall, the Ising-type wall. An Ising wall seperates two domains having the same magnitude of the order parameter but with opposite signs. The order parameter changes from one sign to

another without any rotation by passing through a value 0 in the middle of the boundary as shown in Fig. 7.1.Thus, in the case of PbZrO$_3$,in the middle of the boundary, the suppressing effect of the structural ordering on the ferroelectric instability vanishes, creating favourable conditions for the development of local ferroelectricity at temperatures $T < T_0$ where T$_0$ is the Curie-Weiss temperature of the dielectric anomaly [153]. In Chapter 6, T_O is seen to be reduced only 30K implying that room temperature observations of local ferroelectricity should be possible in these thin films.
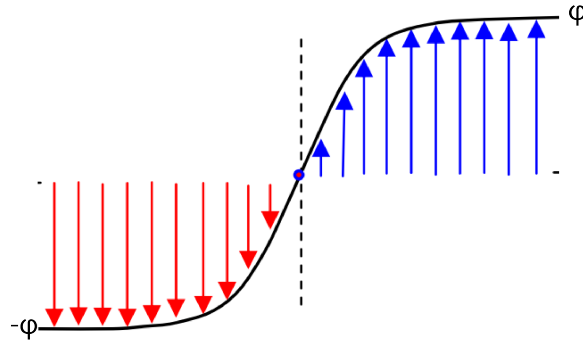
Figure 7.1: Illustration of an Ising wall seperating two domains with the same magnitude of order parameter but with opposite signs (+φ and -φ). The order parameter passes through 0 at the center of the wall, and shows localised ferroelectric behaviour as observed in single crystals of PbZrO$_3$ [153].

The possibility of local ferroelectricity in domain boundaries can be discussed referring to the Σ point-related component of the order parameter, with lead displacemetns having the form

$$\vec{r}_{Pb} \propto \begin{pmatrix} -1 \\ 1 \\ 0 \end{pmatrix} \cos\left[\frac{\pi}{2a}(x_c + y_c) + \varphi \right] \tag{7.2}$$

where x$_c$=n$_1$a$_c$ and y$_c$= n$_2$a$_c$ (n$_1$ and n$_2$ are integers) are the coordinates in the cubic lattice frame and φ is the phase of the modulation. Through this modulation, two types of domain states are formed: orientational and translational [24]. The orientational states (ferroelastic twins) differ by the orientation of the atomic displacements. The translational domain states that correspond to a given orientational state can be turned from one to another by shifting the lattice by a$_c$, 2a$_c$ or 3a$_c$, corresponding to a fraction of a lattice translation vector of the low temperature phase. In view of the quadrupling of the unit cell, there are four translational domain states for each orientational state. In terms of Eq. 7.2, the displacements in these states correspond to $\varphi = \pi/4, 3\pi/4, 5\pi/4, 7\pi/4$. These states can be visualised in the plane of the complex order parameter, $\xi = \rho e^{i\varphi}$ corresponding to the points marked with four circles (Fig. 7.2), where φ is the phase of the order parameter and ρ is its modulus, proportional to
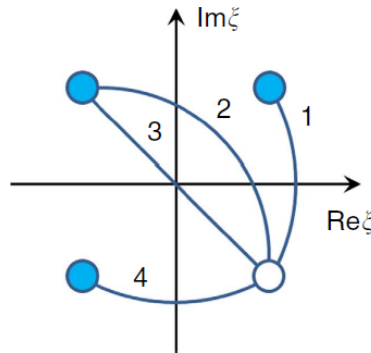
Figure 7.2: Mapping of the translational domain states and boundaries inside a single orientational domain of PbZrO$_3$ on the plane of the complex order parameter. Circles correspond to the translational domain states corresponding to the 4 values of φ while the lines correspond to the boundaries. Boundaries linking a single domain state (marked by the empty circle) are shown with numbered lines. The phase shifts $\Delta\varphi$ of the modulation of the lead displacements in the walls are: line 1- the $\pi/2$ wall, $\Delta\varphi=\pi/2$; lines 2 and 3- the π walls(anti-phase boundaries, APB), $\Delta\varphi=\pi$; line 4- the $3\pi/2$ wall, $\Delta\varphi=3\pi/2$. In the π wall (line 3), the order parameter passes through zero and represents an Ising wall as in Fig. 7.1. Line 2, though corresponding to a phase shift of π, is accompanied by an out of plane rotation of the order parameter (Bloch wall), and is thus different from line 2.

the magnitude of the lead displacements.

Three types of translational boundaries, corresponding to the phase shifts of $\pi/2$, π and $3\pi/2$ can seperate the four translational states. The possible mappings of these translational boundaries are schematically shown in Fig. 7.2 with solid lines. Considering the white dot as the value of φ corresponding to the reference domain, the boundary between this domain and any of the domains represented by blue dots can be traced, and the angular variation between these dots defines the phase shift across the wall. Line 3 is of particular interest as it corresponds to a π wall, i.e., having a phase shift of π, hence called an antiphase boundary (APB). In the middle of such π walls, the order parameter passes through zero (as in an Ising wall), and hence where the suppressing effect of the order parameter on the ferroelectric instability is reduced. The π walls are, hence, of special interest for their local ferroelectric behaviour.

7.2 Lattice dependance of translational boundaries

In Chapter 4, it was seen in Fig. 4.5, that the dispersion of the in-plane polarised TA mode is heavily anisotropic, with the energy being anomalously low along the [110] direction (of the reciprocal cubic lattice), while no such anomalous dispersion was observed for the out-of-plane polarised TA mode. Any deviation from this direction results in a rapid increase of the energy of the mode towards more 'normal' values. The low dispersion of the in-plane polarised

TA mode along the [110] direction implies a low correlation between the atomic planes parallel the [1-10] direction in real space. Incidentally, this corresponds to the direction of the lead displacements (along the orthorhombic a-axis) as described by the Σ point instability in the high temperature phase. Thus, planes containing a disruption in the symmetry of the lead displacements, i.e. translational boundaries, are most favourably oriented parallel to the [1-10] direction. As a result, antiphase boundaries in PbZrO₃ are preferably oriented parallel to the [1-10] cubic direction (orthorhombic a-axis) too. Any other orientation for the antiphase boundaries, though not excluded, is energetically less favourable.

In phenomenological theory, the contribution of a domain wall to the free energy of the system is given by the term $\frac{1}{2}g(\nabla\rho)^2$ wherein the coefficient g is referred to as the 'correlation energy' [154]. Including this term in the free energy expression for the single crystal, on minimising the free energy of the system with the domain wall, the profile of the order parameter across the domain wall can be obtained. This profile has a spatial scale (or correlation length) corresponding to

$$t_{th} = \sqrt{-2g/\alpha} \tag{7.3}$$

where α is the inverse susceptibility. The previously described low correlation in the atomic displacements parallel to the [1-10] plane suggests a low value for the coefficient g along the special direction, which translates into a low correlation length from Eq. 7.3. Thus, not only are the translational boundaries oriented parallel to the [1-10] direction, they are also expected to be extremely thin (with a sharp profile) for these orientations. Any other orientation (corresponding to a strong dispersion of the corresponding TA wave, with stronger correlation) would be associated with a larger value of the coefficient g, and would thus present a thicker, more diffused profile.

7.3 Experimental and analytical details

7.3.1 Sample Preparation and Observation Techniques

For the thin film cross section observations, the lamellar TEM specimens were prepared using focused ion beam system. To remove the contamination and the damaged layers, plasma cleaning and NanoMill Model 1040 system operated at 500 V were used to clean and mill the lamella samples. The lamellar samples were heated above the phase transition and then cooled at 9 K/min to recover the orthorhombic phase. The TEM investigation was performed on an FEI Titan 80-300 microscope with a Cs corrector for the objective lens. The available

point resolution was better than 0.08 nm at an operating voltage of 300kV. The experimental image was filtered to minimize the effect of contrast noise. Structure modelling and image simulation were carried out using the CrystalKit-MacTempas software package. These samples were prepared at the Ernst Ruska Center for Microscopy and Spectroscopy with Electrons, Research Center Jülich by D. Meertens. The observions and the image analysis were carried out by Dr. Xian-kui Wei.

For the observation of thin films through the planar TEM technique, the sample was prepared by conventional thinning techniques. A section of the film with the substrate was mechanically polished and subsequently thinned using ion beam milling on the Gatan PIPS ion mill to obtain electron transparent samples. The observations were carried out in the JEOL 2200 FS microscope. The sample was prepared by Dr. Cosmin Sandu and the observations were conducted by Dr. Duncan Alexander and Dr. Cosmin Sandu.

7.3.2   Image processing for obtaining atomic positions

The filtered experimental image was quantified in the following manner. First, a least-square fit was performed with a 2D Gaussian profile to each of the individual intensity maxima of image, that corresponds to the positions of atomic columns. On the basis of this, a transverse averaging of the shifts of each column species with respect to its cubic structure was plotted as a function of the atomic coordinate. For picometer precision measurements, the residual objective-lens and tilting of the zone axis away from the incident electron beam were examined in the simulation to remove the deviation of the positions of contrast maxima in the image from the real atomic positions. This was achieved through an iterative comparison of the calculated images with the experimental image from a perfect domain region, by adjusting the image parameters in the experimental image until the best fit between the calculated and the experimental images was obtained. The imaging parameters used for the calculated image with the best fit were determined as the parameters for the observation. Finally, a structural model containing the APB was constructed for the simulated images based on the experimental image (and the observation conditions). An additional iterative comparison between the calculated and the experimental images was carried out till a best fit was obtained. The thus obtained structural model provides the real atomic positions at the APB area which is then used to calculate the local polarisation.
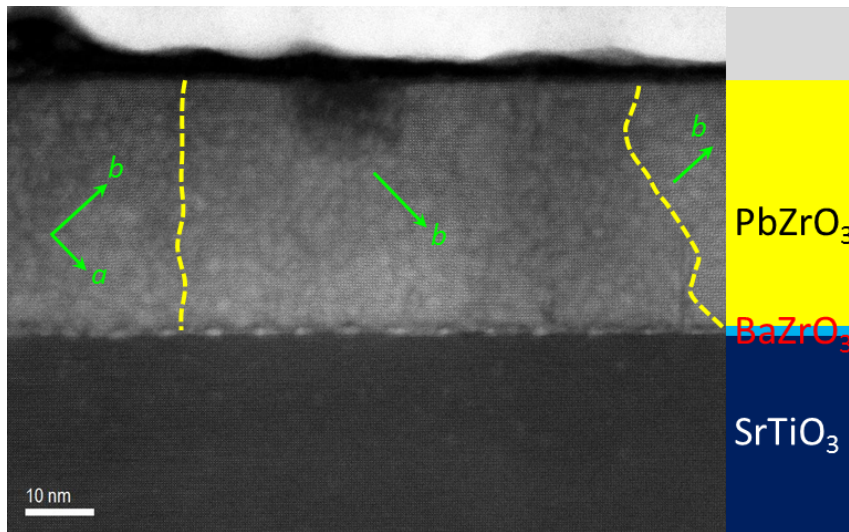
Figure 7.3: Cross section image of the thin film showing the PbZrO$_3$, BaZrO$_3$ and the SrTiO$_3$ layers. Through the direction of the lead displacements, 2 kinds of ferroelastic domains are seen on the edges and in the center respectively, seperated by 90° domain walls (dashed yellow lines).

7.4 Observation of translational boundaries in thin films of PbZrO$_3$

7.4.1 Nature of π walls

A cross section specimen of a 35nm thick PbZrO$_3$ film with 1nm BaZrO$_3$ buffer layer (grown on a SrTiO$_3$ substrate) was prepared for observing the translational boundaries in PbZrO$_3$. Figure 7.3 shows a low magnification image of the cross section with the PbZrO$_3$, BaZrO$_3$ and the SrTiO$_3$ layers seen distinctly. Through the direction of displacement of the lead atoms, the orthorhombic axes in the domains are differentiated. In Chapter 5, three different domain states are presented for cube-on-cube epitaxial PbZrO$_3$ films using a pseudotetragonal lattice. In this pseudotetragonal lattice, the [110] and the [1-10] directions are assumed to be equivalent (see Fig. 5.7), but in reality, these directions are not equivalent since they are differentiated by the direction of displacement of the Pb atoms parallel to only one of the two directions [1-10] or [110]. Thus, each of the domain variants previously described could correspond to two orientational domains defined by the 2 perpendicular directions for the displacement of the Pb atoms. Two such domains are presented in Fig. 7.3, where for the same kind of domain variant (variant A/B defined in Section 5.4.3.1), the two orientational domains corresponding to two different directions of the Pb displacements (perpendicular to b) are observed. They are hence ferroelastic domains and are seperated by ferroelastic domain walls (dashed yellow lines).

High resolution imaging within each domain permits the observation of translational bound-

aries (including the APBs) through the local disruption in the displacements of the Pb atoms. Figure 7.4 shows a single orientational domain (identical to those observed on the edges of Fig.7.3) containing 2 different translational domains (domains I, III and domains II,IV) and the translational boundaries between them (shaded in blue). The green lines represent the orthorhombic unit cell (the yellow dots represent the Pb atoms) in each domain with the shorter edge as the a-axis and the longer edge as the b-axis. The orientation of the translational boundaries is parallel to the orthorhombic a-axis, as was predicted in section 7.2 through the energetical considerations associated with the decoupling of atomic displacements.
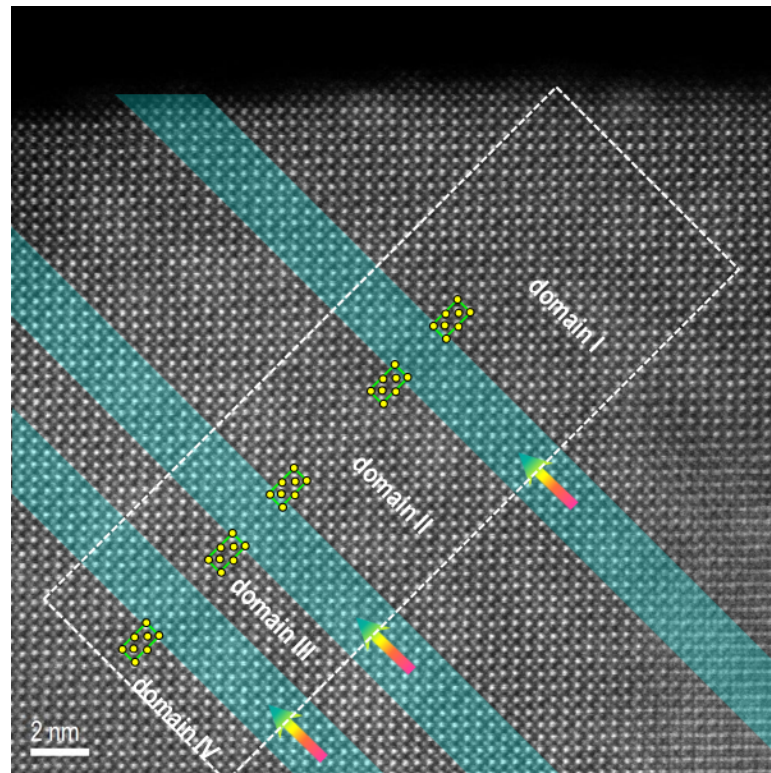
Figure 7.4: A high resolution image of a single orientational domain in the PbZrO$_3$ film showing two alternating translational domain states (domain I= domain III and domain II=domain IV) and their translational domain boundaries (shaded blue). The orthorhombic cell is shown using the solid green line with the lead atoms in yellow. The domain boundaries are seen to be parallel to the orthorhombic a-axis as expected from section 7.2.

Fig. 7.5 (a) shows a magnified section of fig. 7.4, showing clearly the translational domains and their respective domain boundaries. On repeating the orthorhombic unit cell into the domain boundary for both translational domains on either side of the translational domain boundary, the two domains are seen to overlap by a half unit cell, signifying a phase shift of π across the domain wall. These translational boundaries are, thus, antiphase domain boundaries. Figure 7.5 (b) shows two translational domains and an APB under similar observations on a single crystal [153], wherein the half cell overlap in the domain boundary between the two

domains is observed as well. The thickness of the observed π walls in both the thin film and the single crystal are comparable, and additionally, the orientation of the π walls in both the cases is seen to be along the same direction: the orthorhombic a-axis. The properties of the APBs in the thin film are hence expected to be similar to the properties of the APBs previously observed in the single crystal.
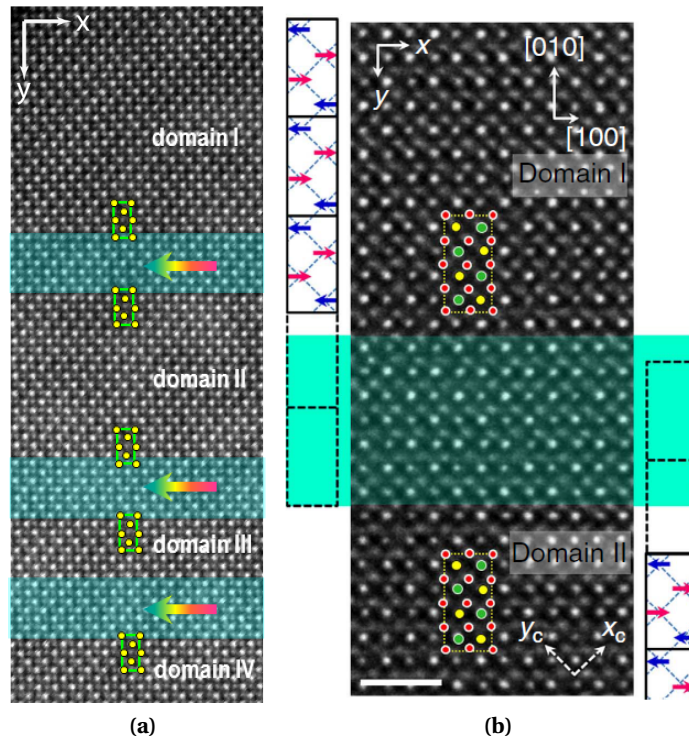
Figure 7.5: (a)A magnified image of the translational domains seen in Fig. 7.4 showing the translational boundaries and the orthorhombic unit cell (solid green line) with the Pb atoms (yellow dots). By repeating the orthorhombic cell across the domain boundary from both adjoining translational domains, it is seen that they overlap by half a unit cell, thus making them π walls (or antiphase boundaries, APBs). (b) A similar study done on a single translational domain boundary in a PbZrO$_3$ single crystal [153], showing the half-unit cell overlap between the two translational domains across the domain boundary.

From the picometer resolution of the images, using the deviation of the atoms from their equilibrium positions, the local polarisation can be estimated. A plot of the displacement of the Pb atoms parallel to the wall and relative to their positions in the cubic phase is shown in Fig. 7.6(a), across the entire segment shown in Fig. 7.5 (a). This plot shows a local breaking of symmetry in the Pb displacements across all the three APBs in the image (marked by red circles). Previously observed π walls in single crystals of PbZrO$_3$ (see Fig. 7.6(b), the blue squares) show the displacements of the lead atoms parallel to the APB (shaded blue) relative to the cubic phase and a similar change in the in-plane displacement of the Pb across the APB in the thin film is observed here as well. This local disruption observed in the π wall of the single
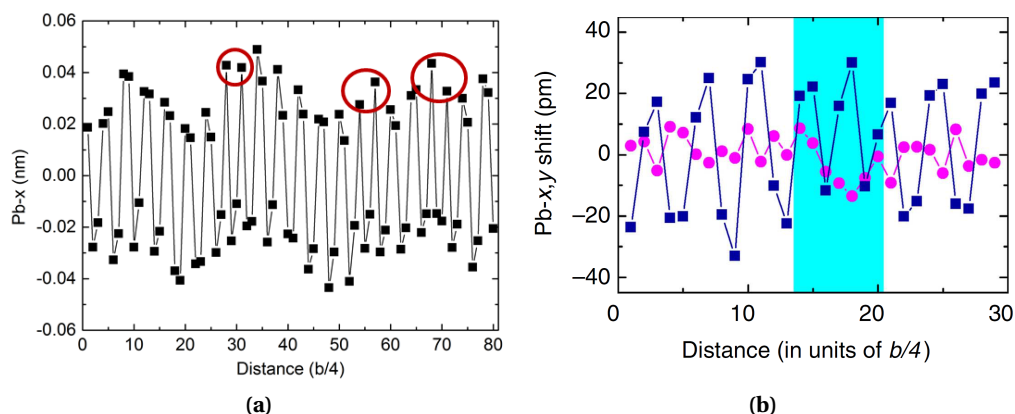
Figure 7.6: (a) The displacements of the Pb atoms from their cubic positions as a function of their coordinate (along the b-axis) across the 4 translational domains and the APBs seen in fig. 7.5(a). (b) Displacements of Pb atoms away from their positions in the cubic phase parallel to (blue squares) and perpendicular to the APB plane (pink circles) in a single crystal sample [153]. The Pb atoms in the APB observed in the thin film sample are seen to have a similar displacement profile as those in the single crystal and hence, the APBs in the thin film are potentially ferroelectric.

crystal was associated with a maximum in-plane polarisation of 14 μC/cm^2 and the APBs observed in the thin films are expected to contain comparable magnitudes of polarisation. Currently, further analysis is being undertaken to quantify this polarisation across the APB in the thin film.

7.4.2 Density of translational boundaries in thin films

Planar TEM observations were carried out for the observation of the spatial distribution of, and the interactions between translational boundaries. The sample was prepared from a thin film of PbZrO₃ (approximately 70nm thick) grown on a SrTiO₃ substrate with a 1nm BaZrO₃ buffer layer. In Fig. 7.7 is shown a low magnification bright field image from the electron transparent part of the sample. The left half of the image shows interference patterns (Moire fringes) arising from the superposition of the lattices of the film and the substrate below. The right half of the image, on the other hand, corresponds to a free standing film (without the substrate) and hence, does not show these fringes. Due to the high interfacial stress from the substrate during the growth of the film, a high density of misfit and threading dislocations are expected in the films, the latter being seen in this image as spots. Also seen are the ferroelastic domains described in the previous section, which provide for an orientational contrast in the lower right half of the film. The ferroelastic domain boundary is fairly sharp and is often seen to change orientation on encountering threading dislocations.

The Selected Area Diffraction (SAD) image of the free standing film is shown in Fig. 7.8 (a),
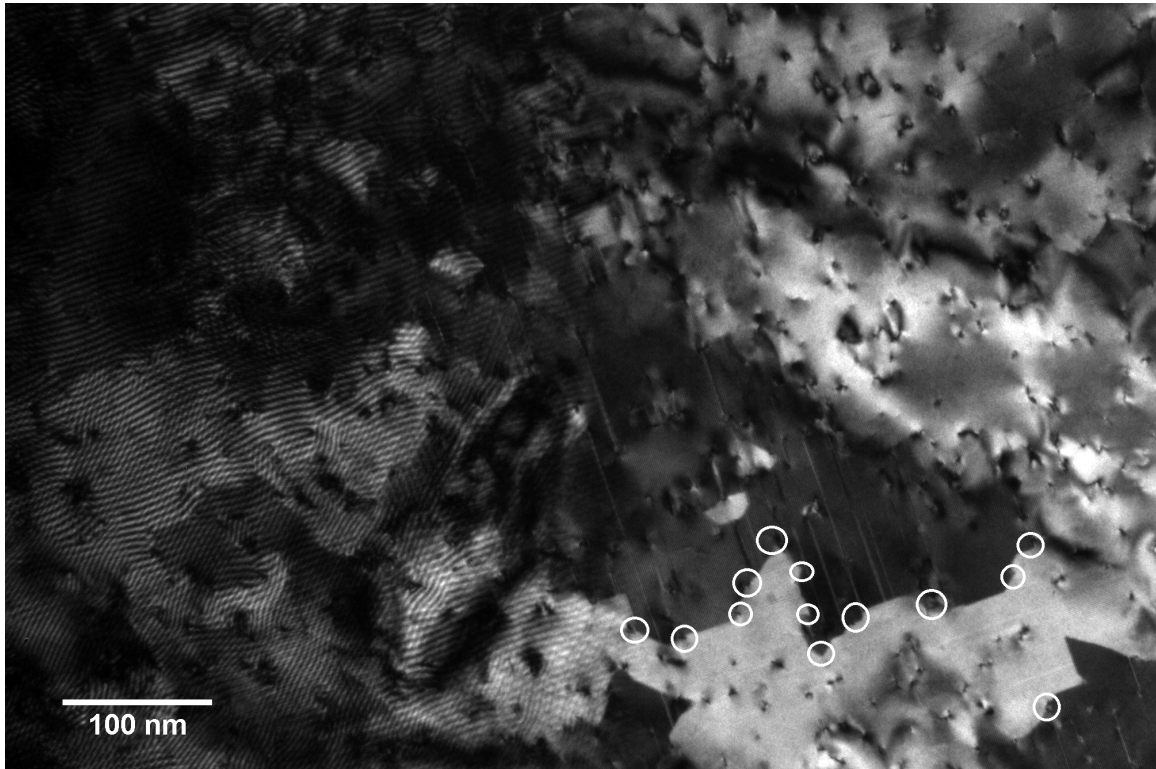
Figure 7.7: Bright field planar TEM image of the PbZrO$_3$ film on SrTiO$_3$ substrate with 1nm. BaZrO$_3$ buffer layer. On the left half of the image are seen the Moire fringes arising out of superposition of the lattices from the substrate and the film. On the right half of the image, the film is free standing and these interference fringes are absent. The contrast seen on the lower right end of the image arises from the ferroelastic domains in the sample. The spots (some circled in white) correspond to threading dislocations and are seen to deviate the ferroelastic boundaries.

representing the superposition of the superlattice peaks from two orthogonal orientational domains. Using a diffraction aperture of the smallest size, a single spot from the diffraction pattern can be isolated, and a dark field image can be obtained. Two isolated spots from the two different superlattices (spots A and B in Fig. 7.8(a)) were seperately chosen for the dark field imaging. In this way, the dark field image contains only the contribution of one of the two domains, as seen in Figs. 7.8 (b) and (c). The spots chosen correspond to the {210} family of planes for the different domains. Since translational boundaries are formed from a local disruption of the translational symmetry, these structures would not satisfy the same diffraction criteria as the domain. Thus, during the acquisition of a dark field image, while the domain satisfies the diffraction criteria and appears bright, the translational boundaries do not, and appear dark. As a result, is seen in the dark field images in Fig 7.8, dark parallel streaks against a bright domain, corresponding to the translational boundaries present in a single orientational domain. Also is interesting to note the relative orientation of the translational boundaries in the two ferroelastic domains perpendicular to each other, as is expected for 90°

domains.

The translational boundaries are often seen to interact with each other resulting in annihilation, shown in Fig. 7.9(a). Such interactions have been previously observed for the π walls in single crystal samples of PbZrO$_3$, as can be seen in Fig. 7.9 (b), where in the APBs annihilate each other or split into two $\pi/2$ walls. The exact nature of the interacting translational boundaries in the thin film remains yet undetermined, and is being currently analysed. Meanwhile, at the point of interaction, the contrast from the boundaries is no longer sharp. This is because of the deviation of the wall from its ideal orientation (parallel to the orthorhombic 'a' axis), associated with a much larger energy gradient for the decoupling of lead atoms, resulting in the widening of the wall and thus, a diffusion of the contrast.

In Chapter 2, the relation between a dislocation and an antiphase boundary has been shown. The termination of translational boundaries at dislocation segments is observed in the images obtained from the thin film. The spotted contrast observed in the sample, as explained previously, corresponds to the threading dislocations in the sample. It is seen clearly in Fig. 7.10 that the translational boundaries terminate preferentially at these defects. The same can be seen in Fig. 7.9(a). Observation of the interaction of dislocations with APBs with dislocations has been shown for the case of Gd$_2$(MoO$_4$)$_2$ [155, 156], where the termination of the APBs at edge dislocations has been claimed as well. Moreover, the spatial frequency of these boundaries (around 5nm) is very close to the frequency of the misfit dislocations observed in a PbZrO$_3$ film with a 1nm thick buffer layer of BaZrO$_3$ (around 4nm, from table 5.4). As a result, it can be claimed that the control of the misfit dislocation density in the thin films results in the control of the density of the translational boundaries in the films.

7.5 Anomalies in domain boundaries of PbZrO$_3$

Ferroelastic domain walls are often required to satisfy mechanical compatibility conditions with associated ferroelastic domains, which imposes heavy restrictions on the orientations of such domain walls [24]. This is not restricted solely to systems without an antiferrodistortive transition, for even in systems with competing interactions such as with Gd$_2$(MoO$_4$)$_3$ [155, 156], ferroelastic boundaries were observed to be extremely restrained to certain crystallographic orientations. On the other hand, the antiphase boundaries in Gd$_2$(MoO$_4$)$_3$ were seen to exhibit little anisotropy in their surface tension, found forming arbitrary shapes and often ending in themselves while forming loops. In the current case, though, one observes the exact opposite behaviour between the ferroelastic domains and the translational boundaries.
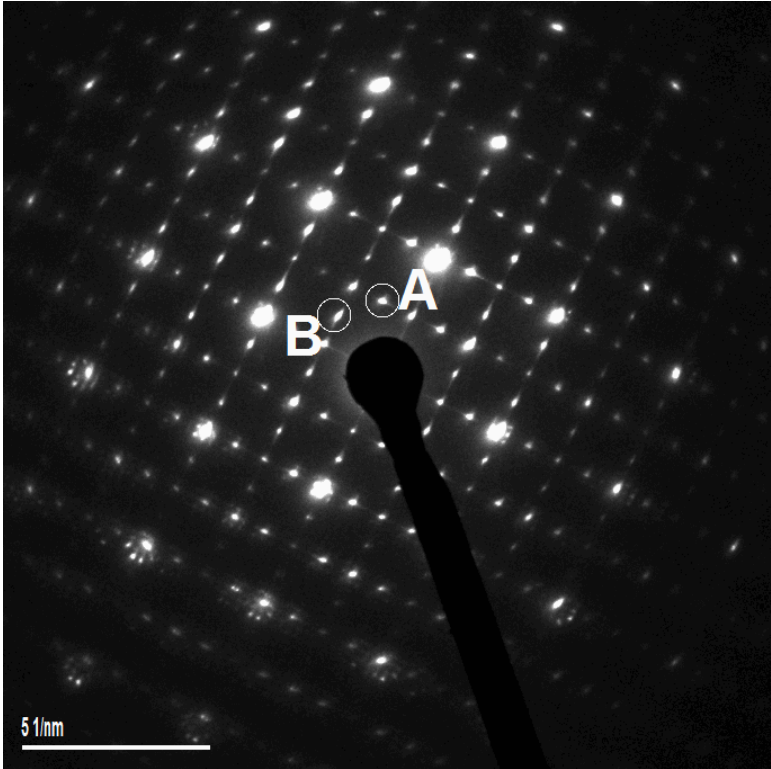
(a)
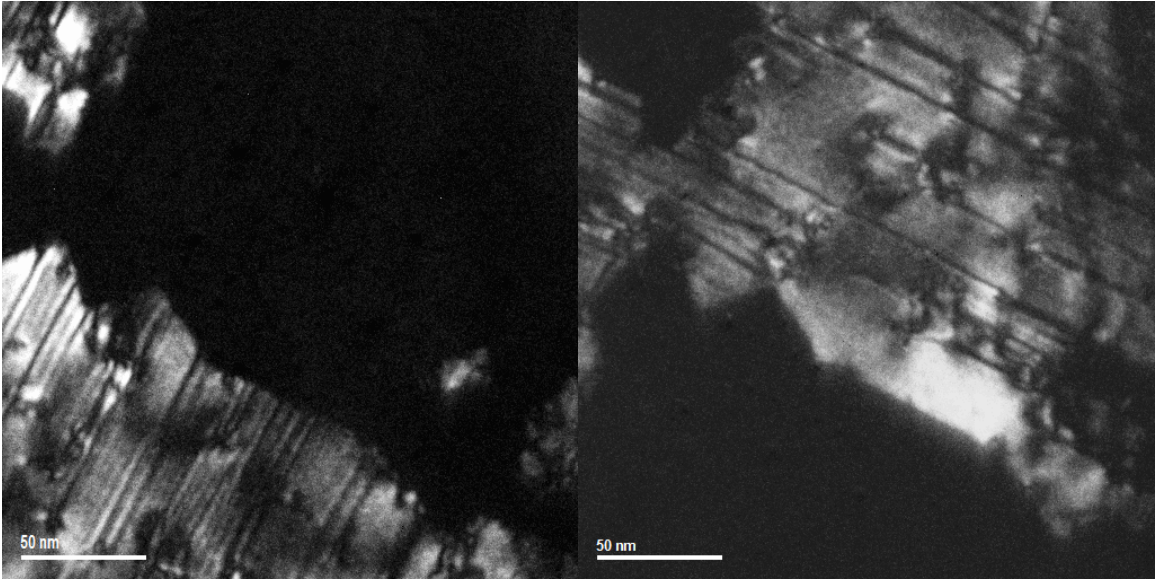
(b)   **(c)**

Figure 7.8: (a) Selected Area Diffraction pattern from the region of observation showing the superposition of superlattices from orthogonal domains in the sample. The spot A corresponds to the (-210) oriented domains while the B spot corresponds to the (1-20) oriented domain. Dark field image from the spots (b) A and (c) B of the SAD pattern showing the parallelly aligned APBs in a dark contrast on a bright orientational domain. As a result of the orthogonal nature of the two domains, the APBs are seen to be perpendicular with respect to each other.

(a)	**(b)**

Figure 7.9: (a) Dark field image of a single orientational domain showing formation of loops (circled in red) resulting from interaction of different translational boundaries. (b) Interaction of different translational boundaries in a single crystal of PbZrO$_3$ showing the annihilation (circles 1 and 2) and the splitting (circle 3) of a translational boundaries [153](Scale bar- 200nm).
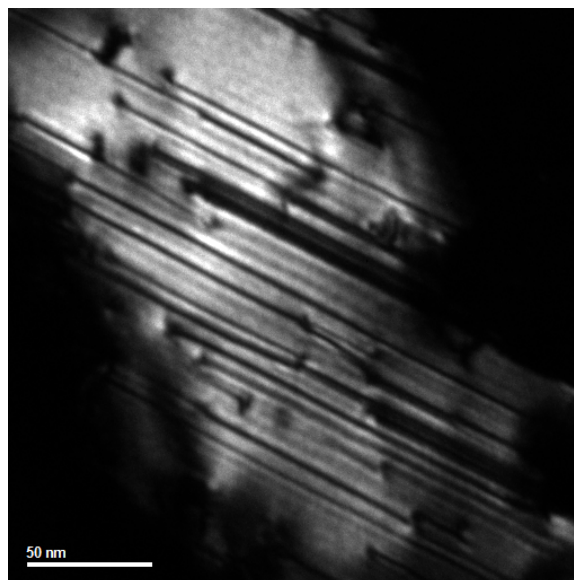
Figure 7.10: Dark field image from a single orientational domain showing the termination of translational boundaries at threading dislocations. The same can also be seen in 7.9(b).

While the former are hardly seen to be restricted to certain crystallographic directions (see Figs. 7.8, 7.7), the latter are seen to be extremely straight and restricted to one single crystallographic direction in each ferroelastic domain. This counterintuitive observation for the ferroelastic walls arises from the unusually minimal ferroelastic strain associated with the two orientational domain states observed in Fig. 7.3, resulting in very minimal anisotropy of the surface tension of the ferroelastic wall, causing them to be oriented arbitrarily. On the other hand, the translational boundaries since they are associated with a decoupling of the displacement of the Pb atoms, have extremely anisotropic surface tension (as explained in Section 7.2), with the minimal surface energy for orientations parallel to the orthorhombic a-axis, resulting in their extremely straight orientations along this direction. Thus, as a result of the unusual interplay of the lattice dynamics and the antiferrodistortive phase transition, the domain boundaries (both orientational and translational) in PbZrO$_3$ present anomalous orientational behaviour.

7.6 Conclusions

With the use of advanced TEM techniques, the orientational and translational domains and domain boundaries in PbZrO$_3$ were observed. The orientational boundaries are ferroelastic 90° domain walls and are often deviated by the threading dislocations present in the films (formed during the growth of the thin film). The translational boundaries are identical to the ones previously observed in the single crystal specimens and their spatial distribution is closely related to the density of the misfit dislocations expected for the film. They are also seen to end at threading dislocations. The antiphase boundaries observed in the thin film show a local disruption in the displacement of the lead atoms similar to those previously noticed in the single crystal, thus suggesting a local ferroelectricity along the antiphase boundaries. Alongside, the ferroelastic domain walls and the translational boundaries in PbZrO$_3$ show anomalous orientational behaviour when compared to the behaviour of such walls in other systems with competing order parameters such as Gd$_2$(MoO$_4$)$_3$. This is explained through the unique lattice dynamics and antiferrodistive phase transition in PbZrO$_3$.

8 Mechanical behaviour of antiphase domain walls

From the prediction of the ferroelectric nature of antiphase domain boundaries (APBs) in SrTiO$_3$ [59], the existance of such ferroelectric walls in PbZrO$_3$ has been observed in thin films of PbZrO$_3$, as seen in chapter 7. In order to be able to envisage the exploitation of these structures, the understanding of their mechanical behaviour is crucial. This chapter is directed towards the estimation of the mechanical responses that one could expect from the APBs in the presence of an external electric field.

8.1   Introduction

As a result of competing structural and ferroelectric instabilities in SrTiO$_3$ [59] the appearance of the ferroelectric order parameter was predicted in the absence of the otherwise dominant structural order parameter, which occurs along the so-called 'anti-phase domain boundaries' (APBs) in the material. Similar analysis of competing order parameters in antiferroelectric PbZrO$_3$ has shown the existance of ferroelectric behaviour along boundaries wherein the primary structural order parameter is subdued, as was observed in thin films of PbZrO$_3$, shown in Chapter 7. In order to be able to exploit such structures, an understanding of their behaviour in the presence of an electrical field is essential. The current chapter deals with the displacement of such walls in the presence of an external electrical field. As will be explained later, these walls interact solely with inhomogeneous electrical fields. To this effect, the field gradient arising out of an AFM tip is used to displace an APB lying in the vicinity of the tip. Estimates of the magnitude of displacement are obtained by solving equations representing the equilibrium of the various forces acting on the wall, and the conditions required for an observable displacement of the wall are outlined.

8.2   Interaction of the domain wall with an external field

Consider a section of a ferroelectric APB centered initially at a certain distance y_i from the AFM tip (refer Fig. 8.1), having a polarisation profile described by the function $P(y-y_i)$. On applying a certain voltage on the tip, a field $E(y)$ is generated in the material, and the corresponding contribution to the thermodynamic potential density and integrated potential for the current configuration are given by Eqs. 8.1 and 8.2 respectively.

$$\rho(y) \quad = \quad 2P(y-y_i).E(y) \tag{8.1}$$

$$\rho \quad = \quad 2\int P(y-y_i).E(y)dy \tag{8.2}$$

The derivative of the potential ρ w.r.t. the wall position (∂y_i) yields the force F_{el} acting during
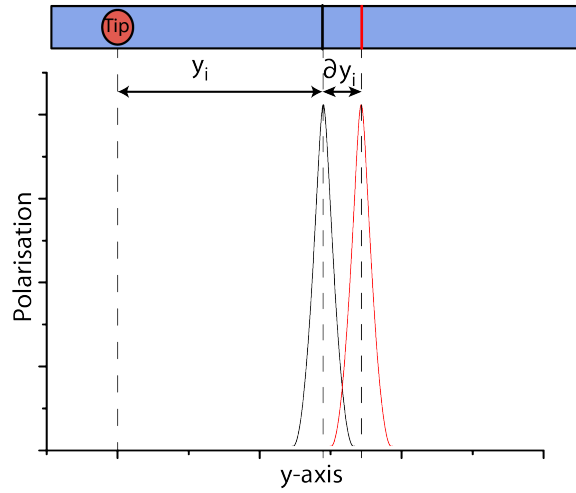
Figure 8.1: Illustration of the interaction between a section of an APD and the electric field from an AFM tip. The polarisation profile (along the y-axis) initially centered at a distance y_i (black curve) from the AFM tip is displaced by an infinitesimal ∂y_i to a new position (red curve) in the presence of an inhomogeneous external field.

an elementary displacement of the wall by a value ∂y_i (shown in Eq. 8.3) which is rearranged using integration by parts to obtain Eq. 8.5.

$$F_{el} \quad = \quad 2\frac{\partial}{\partial y_i}\int P(y-y_i).E(y)dy \tag{8.3}$$

$$= \quad -2\int \frac{\partial P(y-y_i)}{\partial y}.E(y)dy \tag{8.4}$$

$$= \quad 2\int P(y-y_i).\frac{\partial E(y)}{\partial y}dy \tag{8.5}$$

From Eq. 8.2, it is evident that in the case of a homogeneous electric field (E(y)= constant), the integral $\int P(y - y_i).E(y)dy$ is reduced to $E.\int P(y - y_i)dy$, rendering the poential of the system invariant with varying y_i. This implies that energetically there is no driving force for the displacement of the wall. This statement is reconfirmed in Eq. 8.5 where a homogeneous electric field ($\frac{\partial E(y)}{\partial y} = 0$) would imply a zero net force on the wall, causing no interaction with the electric field, and thus yielding no displacement.

8.3   Problem Statement

A thin film of predefined thickness (h) with a bottom electrode and containing a flat APB lying perpendicular to its surface is considered, and the AFM tip is placed at a certain distance (y_i) away from the APB. The polarisation in the wall is oriented normal to the surface of the film, pointing out of the surface. On applying a certain applied voltage to the AFM tip, the component of the electric field gradient normal to the film surface (parallel to the polarisation) interacts with the polarisation profile in the wall, giving rise to a force that causes the wall to move. A schematic representation of the problem under consideration is shown in Fig. 8.2. The governing relation for the description of the equilibrium is obtained using variational principles. The profile of the displaced wall is obtained through the application of this relation, using known parameters associated with the APBs in an $SrTiO_3$-like material, with estimation of the unknown values from values for 180° walls in $BaTiO_3$ as an order-of-magnitude estimate. Also, given the lack of information for the conditions for the switching of the polarisation within the APBs, the orientation of the polarisation is assumed to be retained for all values of the applied field. The extent of the displacement is analysed as a function of the film thickness and external parameters such as the applied voltage. The application of a field parallel to the orientation of the polarisation would result in an attractive interaction, but the extent of this attraction (through the symmetry of the field across the AFM tip) is limited to the distance between the flat wall and the tip. On the other hand, the repulsive interaction is not bound by any such parameter. Thus, as a first approximation study, only the repulsive interaction is studied. Further, estimates on the retraction of the wall on the removal of the applied voltage are obtained.
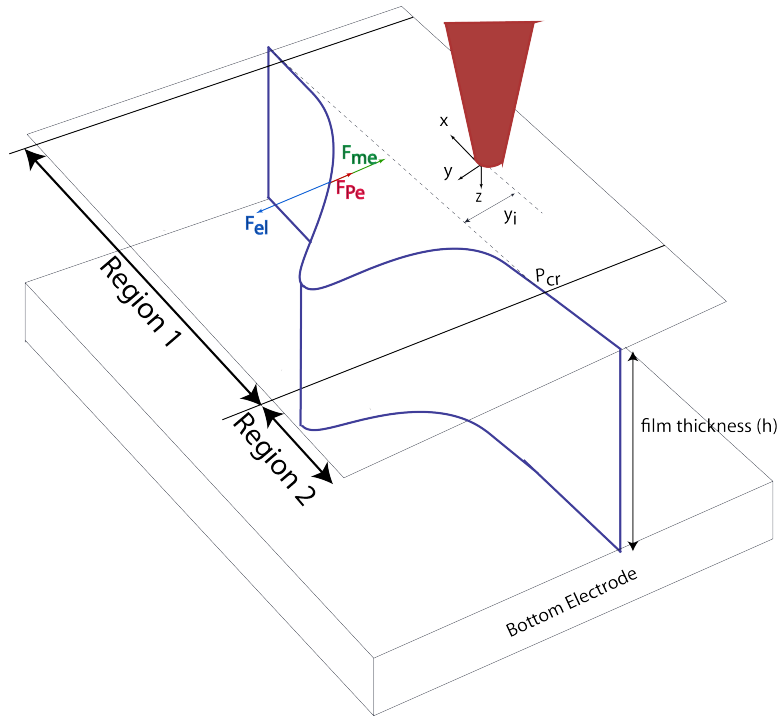
Figure 8.2: Schematic of the problem statement under consideration and its geometry. A flat wall placed initially at a distance y_i from an AFM tip is displaced from a repulsive interaction with the electric field gradient emanating from the latter. The final profile is divided into two regions: Region 1 where the wall is displaced, and Region 2 where the wall remains flat. The point of transition between the two regions is denoted by P_{cr}. The forces acting on the displaced section of the wall are shown schematically.

8.4 Establishing conditions for equilibrium

8.4.1 Governing equations from variational principles

The equilibrium profile for the displaced wall is obtained through the application of variational principles to the thermodynamic potential of the system. The potential of the system is evaluated through the sum of the two active contributions: the electrical contribution (E_{el}) arising from the interaction of the polarisation profile with the electric field gradient, and the wall surface contribution (E_{me}) stemming out of the surface tension associated with a curved wall. The wall is considered to be isotropic in nature, i.e. the surface tension and the wall thickness are assumed to be constant for all orientations of the wall.

In this first approximation study, only weak bending response from the wall is considered, i.e. the deflection angle (between the normal to the wall and y-axis) are approximated to be small enough to neglect the deviation of the normal to the wall from the spatial coordinate y at all points. Thus, for a formerly flat wall at a distance y_i (from the tip), with the center of the displaced profile given by ξ(x,z) away from y_i, the polarisation profile can be represented as

$P(\text{y-}(\xi(\text{x,z})+\text{y}_i))$. Using the suface tension, σ and the spatially varying electric field from an AFM tip $E(x,y,z)$, the potential ψ of the system is calculated by integrating the contributions of the above mentioned contributions over the elemental surface of the wall dS (Eq. 8.6).

$$\psi \quad = \quad E_{me} + E_{el} = \int (\sigma dS) + \int E(x,y,z) \cdot P(y - (\xi(x,z) + y_i)).dy.dS \tag{8.6}$$

Given the sharp variation of polarisation across the wall [59], the variation of the field across the wall is neglected and the coordinate y is replaced by ξ, yielding 8.7.

$$\psi \quad = \quad \int (\sigma dS) + \int P(y - (\xi(x,z) + y_i)).dy \int E(x,\xi,z) dS \tag{8.7}$$

The term $\int P(y - (\xi(x,z) + y_i)) dy$ represents the integrated polarisation in the wall and is evaluated seperately (see Eq. 8.8). It is consequently replaced by the product P_s.w, corresponding an equivalent polarisation P_s spread over a wall width w (Eq. 8.10) . Finally, in accordance with the coordinate axes as shown in Fig. 8.2, the elemental surface area dS is expressed as a function of the coordinates dx and dz, which is simplified to obtain Eq.8.10.

$$P_s \cdot w \quad = \quad \int\limits_{-\infty}^{\infty} P(y - (\xi(x,z) + y_i)).dy \tag{8.8}$$

$$\psi \quad = \quad \int [\sigma + (P_s \cdot w) \cdot E(x,\xi,z)] \cdot \sqrt{1 + \left(\frac{\partial \xi}{\partial x}\right)^2 + \left(\frac{\partial \xi}{\partial z}\right)^2} \, dxdz \tag{8.9}$$

$$\quad = \quad \int [\sigma + (P_s \cdot w) \cdot E(x,\xi,z)] \cdot \left(1 + \frac{1}{2}\left(\frac{\partial \xi}{\partial x}\right)^2 + \frac{1}{2}\left(\frac{\partial \xi}{\partial z}\right)^2\right) dxdz \tag{8.10}$$

Equation 8.10 now defines the functional (L) that is minimalised using variational principles to estimate the equilibrium profile of the deformed wall. To this effect, the Euler-Lagrange equation (Eq. 8.11) is applied to the potential described in Eq.8.10. From the non-linear solution thus obtained, using the weak bending approximation, only linear terms with E or ξ are retained to obtain Eq.8.12. This equation represents the equilibrium between the electrical force(F_{el}, l.h.s. of Eq. 8.12) arising from the interaction of the polarisation profile with the electrical field gradient, and the mechanical force(F_{me}, r.h.s. of Eq. 8.12) arising from the

surface tension of the curved wall.

$$\frac{\partial L}{\partial \xi} - \left[\frac{\frac{\partial L}{(\partial \xi / \partial x)}}{\partial x} + \frac{\frac{\partial L}{(\partial \xi / \partial z)}}{\partial z} \right] = 0 \tag{8.11}$$

$$P_s \cdot w \frac{\partial E}{\partial \xi} = \sigma \left[\frac{\partial^2 \xi}{\partial z^2} + \frac{\partial^2 \xi}{\partial x^2} \right] \tag{8.12}$$

8.4.2   Inclusion of dissipative force

In Section 8.4.1, the equilibrium between the non-dissipative forces acting on the wall has been considered. In reality, a certain dissipative force is exerted by the wall against the deformation, associated with the pinning of a movable boundary. To account for this effect, the concept of dry friction is applied. This pinning force (henceforth F_{pe}) always acts against the displacement (see Fig. 8.2). Dry friction is generally expressed as an inequality, and in the current study the maximum magnitude of this pinning force is defined as $F_{pe} < F_{pe}^{max}$. At points far away from the AFM tip, where F_{el} is much lesser than F_{pe}^{max}, the driving force for the deformation is not large enough to overcome the pinning force, and hence, the wall does not deform (region 2 in Fig. 8.2). In this case, F_{pe} attains a magnitude equal to F_{el}, as given by Eq. 8.13.

$$P_s \cdot w \cdot \frac{\partial E}{\partial \xi} = F_{pe} \tag{8.13}$$

Conversely, in region 1 in Fig. 8.2, the wall is displaced and the mechanical force F_{me} obtains a finite magnitude owing to a curvature associated with the displaced wall. The wall is allowed to displace till the F_{me} associated with the final profile is in equilibrium with F_{el} and the maximum resistive force (F_{pe}^{max}). Thus, the final state of the wall satisfies Eq. 8.14.

$$P_s \cdot w \cdot \frac{\partial E}{\partial \xi} = \sigma [\frac{\partial^2 \xi}{\partial z^2} + \frac{\partial^2 \xi}{\partial x^2}] + F_{pe}^{max} \tag{8.14}$$

8.4.3   Boundary conditions

Starting from Eqs. 8.13 and 8.14 as the governing equations, one can obtain the equilibrium profile of the displaced wall by imposing the appropriate boundary conditions using the

coordinate system in Fig. 8.2. The profile of the displaced wall is required to be symmetrical on either side of the AFM tip. Simultaneously, to avoid singularities in F_{me} arising from a discontinuity in the radius of curvature, a continous variation in the slope of the wall across the entire profile has to be ensured. With these criteria, the boundary conditions for the current configuration are defined by Eqs. 8.15-8.17.

$$
\frac{\partial \xi}{\partial x}|_{x=0} \quad = \quad 0 \tag{8.15}
$$

$$
\xi|_{P_{cr}} \quad = \quad 0 \tag{8.16}
$$

$$
\frac{\partial \xi}{\partial x}|_{P_{cr}} \quad = \quad \frac{\partial \xi}{\partial z}|_{P_{cr}} = 0 \tag{8.17}
$$

where P_{cr} is the point of transition from region I to region II (refer Fig. 8.2)

8.4.4   Relevant parameters

The magnitude of the normal component of the spatially varying electric field in a single crystal is given by Eq. 8.18 [157] where V is the voltage applied to the AFM tip, ϵ_a and ϵ_c are the relative permittivities in directions in and out-of-the x-y plane respectively, R is the radius of the AFM tip and C_v is the interfacial capacitance between the AFM tip and the surface.

$$
E_n \quad = \quad \frac{C_v.V}{4.\pi.\epsilon_0.\frac{\epsilon_c}{\epsilon_a}.(\sqrt{\epsilon_c.\epsilon_a}+1)} . \frac{\frac{z}{\frac{\epsilon_c}{\epsilon_a}}+R}{(x^2+y^2+(\frac{z}{\frac{\epsilon_c}{\epsilon_a}}+R)^2)^{3/2}} \tag{8.18}
$$

The relation for the field in thin films with a bottom electrode in the current scenario is obtained from a modification of Eq. 8.18 using the method of image charges. For this derivation, the interface of the film with the bottom electrode is taken as a virtual mirror. Through this mirror, virtual images of the film as well as the AFM tip are formed, and the charge on the AFM tip from an applied voltage (given by C_v.V in Eq.8.18) forms as well a virtual image charge of the same magnitude at the image of the AFM tip. Thus, for a film of thickness h, the normal component of the field at a point at a depth z (<h) within the sample, can be said to experience a field from the AFM tip corresponding to the Eq. 8.18 and also a virtual field from the image charge present at a point (2h-z) away (in the image). The difference between these two fields

Parameter	Numerical Value(s)	Reference
P_s	$4.2 \, \mu C/cm^2$	[59]
σ	$10 \, mJ/m^2$	[160]
F_{Pe}^{max}	$0.05 \, mJ/m^3$	[161]
w	$10 \, nm$	[59]
R	$10 \, nm$	-
V	$10\text{-}50 \, V$	-
ϵ_a	5500	[162]
ϵ_c	8000	[162]

Table 8.1: Table of parameters used for the calculation of displaced profiles of APBs in an SrTiO$_3$ like system. While most parameters like the wall thickness (w), polarisation (P$_s$) and dielectric constants (ϵ_a and ϵ_c) are readily available for APBs in SrTiO$_3$, some values such as surface tension (σ) and Peierl's barrier (F$_{Pe}^{max}$) are approximated from those corresponding to 180° walls in BaTiO$_3$. R and V represent the radius and the applied voltage for the AFM tip respectively.

is used to describe the field described at the point in consideration, denoted by Eq. 8.19.

$$E_{\text{normal}} = \frac{C_v.V}{4.\pi.\epsilon_0.\frac{\epsilon_c}{\epsilon_a}.(\sqrt{\epsilon_c.\epsilon_a}+1)} \left[\frac{\frac{z}{\frac{\epsilon_c}{\epsilon_a}}+R}{(x^2+y^2+(\frac{z}{\frac{\epsilon_c}{\epsilon_a}}+R)^2)^{3/2}} - \frac{\frac{2h-z}{\frac{\epsilon_c}{\epsilon_a}}+R}{(x^2+y^2+(\frac{2h-z}{\frac{\epsilon_c}{\epsilon_a}}+R)^2)^{3/2}} \right] \quad (8.19)$$

The interfacial capacitance between the AFM tip of radius R and the dielectric surface is calculated using the sphere-plane model given by Eq. 8.20 [158, 159].

$$C_v = 4.\pi.\epsilon_0.R.\frac{(\sqrt{\epsilon_c.\epsilon_a}+1)}{(\sqrt{\epsilon_c.\epsilon_a}-1)}.\ln(\frac{\sqrt{\epsilon_c.\epsilon_a}+1}{2}) \quad (8.20)$$

All calculations were carried out on COMSOL Multiphysics Version 4.3a.

8.5 Profiles of displaced wall for SrTiO$_3$-like system

Using the relations 8.13 and 8.14 for the equilibrium conditions of the displaced wall and the boundary conditions mentioned previously, the profiles for the displaced walls can be obtained for various thicknesses of thin films and at different applied voltages. A SrTiO$_3$-like system is considered for the implimentation and the values corresponding to the maximum polarisation (P$_s$), wall thickness (w) and dielectric constants (ϵ_a and ϵ_c) are obtained from existing data on SrTiO$_3$. Meanwhile the values for the surface tension (σ) and the Peierl's barrier (F$_{pe}^{max}$) are approximated from the values corresponding to 180° walls in BaTiO $_3$. All parameters used for the calculations are summarised in Table 8.1.
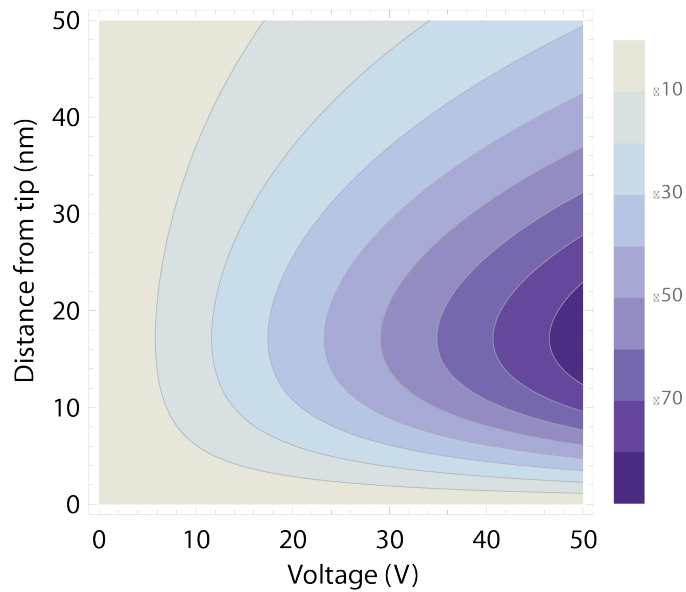
Figure 8.3: The field gradient at the surface of the thin film plotted as a function of applied voltage (in V) and distance from the tip (in nm). The curves are calculated for an AFM tip of 10nm radius, for a 15nm thick film. The legend corresponds to units of 10^4MV/cm^2. The highest field gradient (implying the highest force) for any voltage is seen to be between 10 and 15 nm away from the AFM tip.

8.5.1   Dependance on applied voltage

With increasing applied voltage on the AFM tip, the magnitude of the corresponding field gradient increases. Figure 8.3 shows the contours of the field gradient on the surface of the thin film as a function of the distance from the AFM tip and the applied voltage. The maximum gradient for any applied voltage is found between 10 and 15nm away from the tip. Thus, for all results discussed henceforth, the initial position of the flat wall is fixed 10nm away from the tip. Since the electrical force acting on the wall scales linearly with the field gradient (Eq. 8.5), higher field gradients imply higher electrical forces. For a given film thickness, the displacement of the domain wall thus increases with increasing applied voltage, as seen in Fig. 8.4.

8.5.2   Dependance on Film thickness

Also observed in Fig. 8.4 is that with increasing film thickness, the maximum displacement from the wall decreases. The profile of the displaced wall for films with thicknesses of 30nm and 100nm with an applied voltage of 50V on the AFM tip is compared in Fig. 8.5. The obvious difference between the two cases lies in the reduction of the displacement along the z-axis. While for the thinner film the profile is fairly homogeneous with the depth (i.e. the profile at
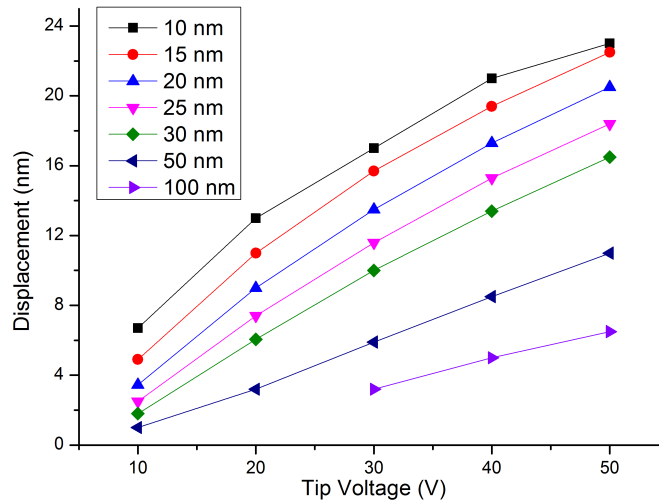
Figure 8.4: The maximum displacement of the APB (at the surface of the thin film) plotted as a function of the applied voltage on the AFM tip for various film thicknesses. The curves are obtained for calculations with an AFM tip of 10nm radius, placed 10nm away from the wall initially. The increase in the displacement of the wall with increasing applied tip voltage is a direct result of the increased field gradient (see Fig. 8.3). Also it is noted that with thicker films, the maximum displacement decreases.

the surface matches closely the profile at the lower interface, see Fig.8.5(c)), for the thicker film, the wall is seen to be almost flat at the lower interface (see Fig.8.5(d)).

To quantify the variation of the displacement at the two interfaces with the film thickness, Fig.8.6 shows the ratio of the displacement at the lower interface to the displacement at the surface as a function of the film thickness, plotted for various applied voltages. A value close to 1 for this ratio shows lower dependance of the displaced profile with the depth in the film, i.e., the closer the ratio is to 1, the closer is the situation to a 2-dimensional problem (independant of z). With increasing film thickness beyond 30nm, the drastic drop in the ratio shows the increasing dependance of the deformation profile with z (corresponding closer to a 3-dimensional problem).

The decreasing displacement of the wall at the lower interface with increasing film thickness (increasing z) is a result of the rapid drop in the field gradient (and hence, F_{el}) with increasing z ($\frac{\partial E}{\partial y} \propto \frac{1}{z^4}$). The reduction in the field gradient along the depth in the film is negligible for those films whose thickness is comparable to the radius of the AFM tip ($h \leq R$). On the other hand, for cases where $h \gg R$ the reduction in the field gradient along z is quite large and by virtue of this drop of field gradient with the depth, there is not enough force to displace the wall at the lower interface and the displacement decreases with increasing z. In thicker

(a)

(b)

(c)

(d)
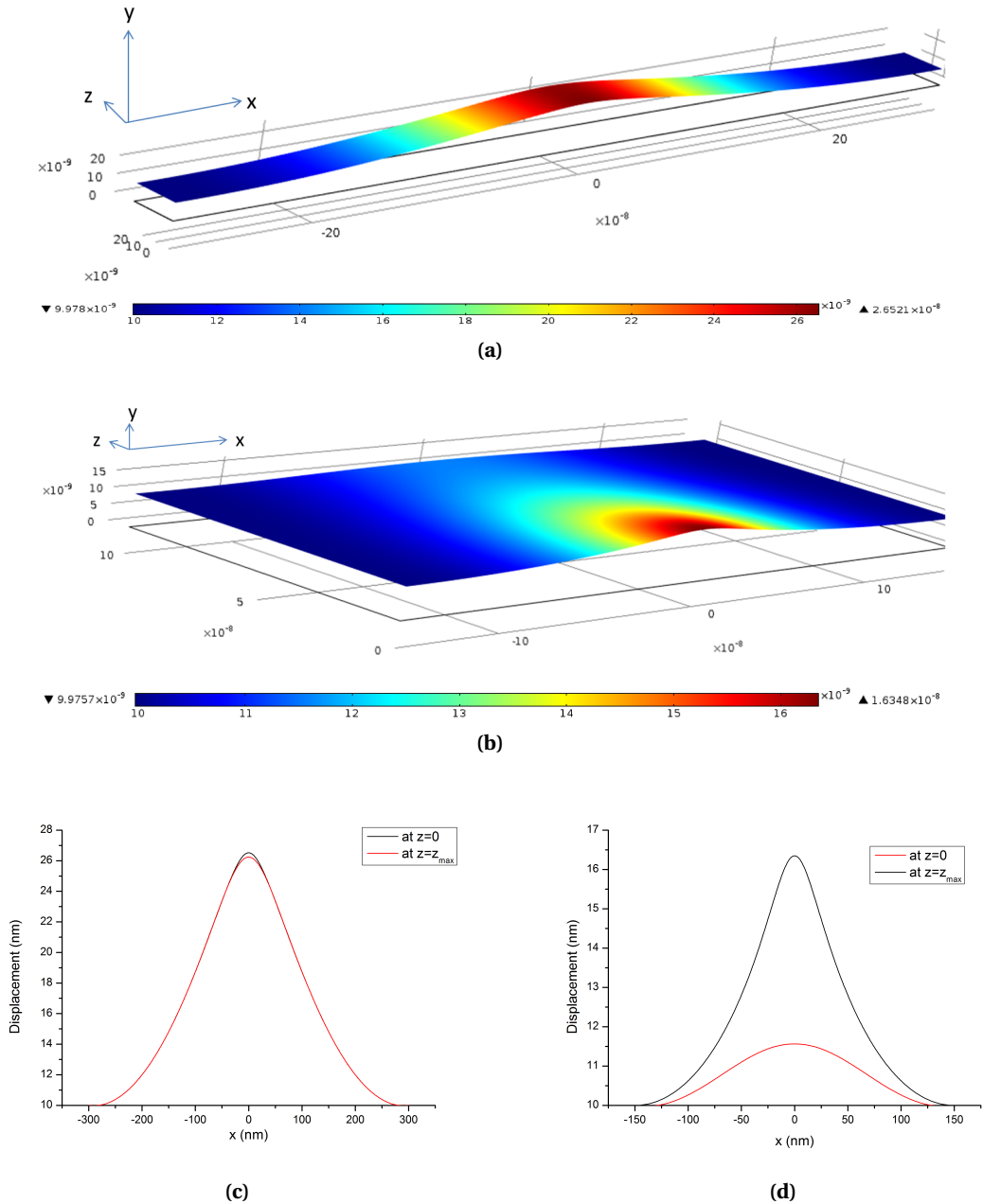
Figure 8.5: 3-D profiles for displaced APB in (a) 30nm thick and (b) 100nm thick film, for an APB located initially 10nm away from the tip (radius of tip= 10nm) , with an applied voltage of 50V on the tip. The uniformity in the displacement along the z-axis for the 30nm thin film is obvious, as is the rapid decrease in the displacement along z for the displaced profile from the 100nm thick film. 2-D cross-sections of the 3-D profile from (c) 30nm thick film (d) 100nm thick film showing the displacement at the surface (black curve) and at the lower interface (red curve) for the two cases. The change in the profile at the two interfaces as well as the decrease in the maximum displacement with increasing film thickness is seen more clearly, and is caused by the increased dependance of the displaced profile on the depth ('z').
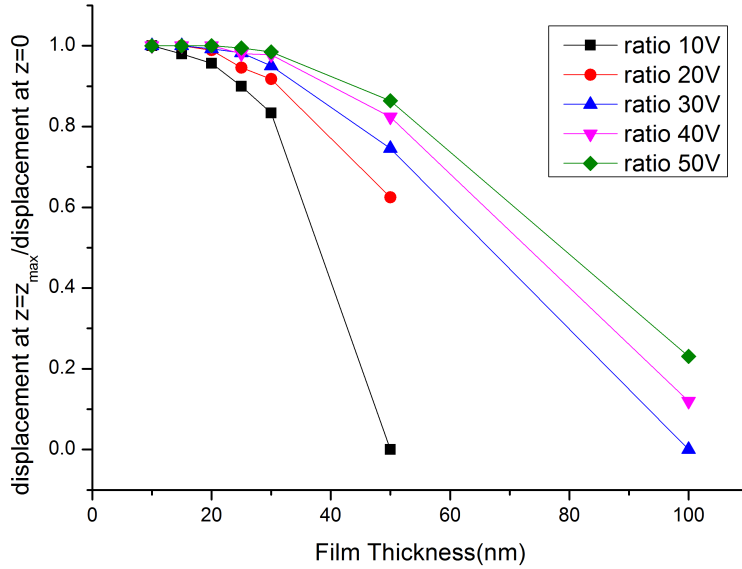
Figure 8.6: The ratio of the maximum displacement at the surface to the maximum displacement at the lower interface of the film as a function of the film thickness for different applied voltages. All calculations were carried out with an AFM tip of radius 10nm placed 10nm away from the initial flat wall. With increasing film thickness, the displacement at the lower end of the film is lesser than at the surface, owing to a rapid drop in field gradient with increasing z, thus making the profile more dependant on z (3-dimensional problem). With lower film thicknesses, the ratio is closer to 1 and the problem is considered to be almost 2-dimensional (independant of z).

films, the existance of this dependance of the displacement along the z-axis, through its finite curvature increases the contribution of the term $\frac{\partial^2 y}{\partial z^2}$ in Eq. 8.14 and consequentially decreases the magnitude of the term $\frac{\partial^2 y}{\partial x^2}$. Since the term $\frac{\partial^2 y}{\partial x^2}$ is related to the displacement and the term $\frac{\partial^2 y}{\partial z^2}$ is related to the bending of the wall, the dominance of the latter over the former acts as a certain 'clamping' against the deformation at the surface. In other words, for thinner films the term $\frac{\partial^2 y}{\partial x^2}$ dominates the mechanical force term yielding higher displacements, whereas, for thicker films the term $\frac{\partial^2 y}{\partial z^2}$ dominates the mechanical force term, yielding lower displacements along y and higher bending along z.

As a case of extremely thick films, displacements of APBs in single crystals is simulated. The spatial variation of the normal component of the electric field in the single crystal is given by Eq. 8.18. Using the same conditions as for thin films (10nm tip radius, 50V applied on the tip placed 10nm away from the APB), the profile of the displaced wall is calculated, and the 2-D sections along the surface (z=0) and along the depth (x=0) of the film are shown in Fig. 8.7. The profiles along the surface and along the depth are seen to be very close to each other, implying almost equal contributions of the terms $(\frac{\partial^2 y}{\partial z^2})$ and $(\frac{\partial^2 y}{\partial x^2})$ towards F_{me}. This falls in line with the

previous observation of increasing contribution of $(\frac{\partial^2 y}{\partial z^2})$ with increasing thickness, resulting in lower displacement at the lower interface, and illustrates an extreme case of bending of the wall in thicker films. The maximum displacement obtained for the APB in a single crystal (0.8nm) is seen to be negligible even in comparison with that obtained from a 100nm thick film under similar conditions (5nm).
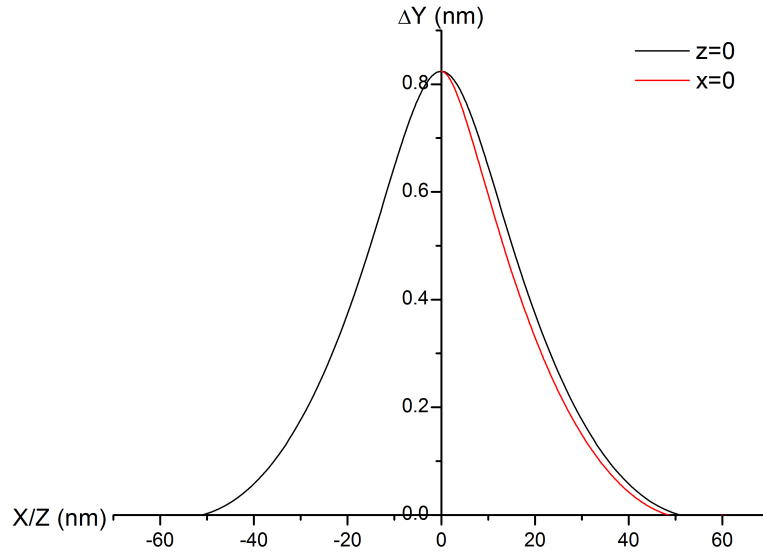
Figure 8.7: 2-D sections of the profile of the wall in a single crystal displaced by an AFM tip of radius 10nm placed 10nm away from the wall and with an applied voltage of 50V . The profile of the wall on the surface (black line, z=0) is seen to be very close to the profile along the depth of the crystal (red line, x=0), showing almost equal contributions from the two directions to F$_{me}$. Through this increased dependance on the surface tension along the z-direction, the maximum displacement of the wall is heavily reduced.

8.5.3 Retained deformation on removal of field

On the removal of the voltage applied to the AFM tip, the driving force for the displacement of the wall is removed and consequently, a change in the profile of the wall is expected since the equilibrium in such a case is defined differently from Eq. 8.14. In the absence of the electrical field, F$_{el}$ is reduced to zero and the new profile is defined by an equilibrium between F$_{me}$ and F$_{pe}$. To explain the methodology for calculating the retraction of the wall, a 2-D profile is considered to begin with. Considering a 2-D section of the deformed wall at the surface of the film, the displaced section of the wall (with the voltage applied on the AFM tip) can be divided into three regions (refer Fig. 8.8). In all the three regions, the F$_{el}$ (green arrow in
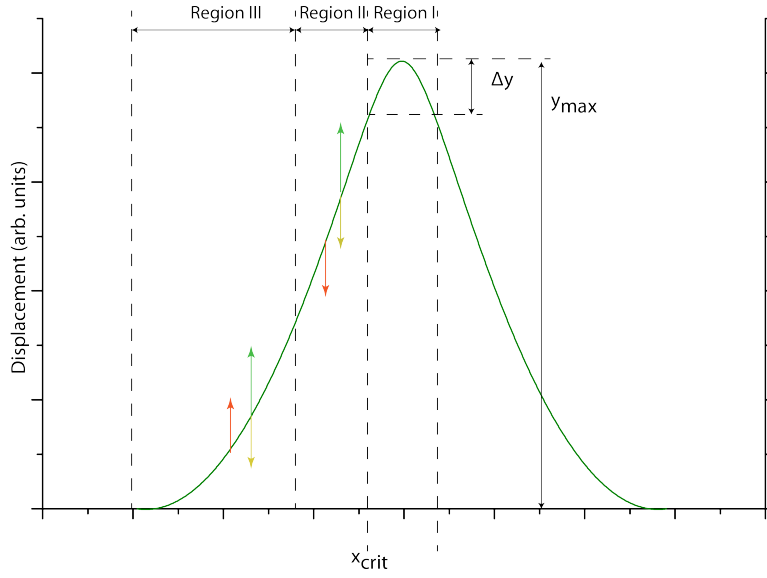
Figure 8.8: Illustration of the 2-D cross section at the film surface of the displaced wall for a certain applied voltage on the AFM tip. The orientations of F_{me}, F_{el} and F_{pe}^{max} are shown by red, green and yellow arrows (The directions are the same in regions I and II). In regions II and III (where $|F_{me}| < F_{pe}^{max}$), on the removal of the applied voltage, the magnitude of F_{pe} reduces from F_{pe}^{max} to equilibriate it with F_{me} and the profile remains unchanged. In region I ($|F_{me}| > F_{pe}^{max}$), on the removal of the applied voltage, to reduce F_{me} to equal F_{pe}^{max}, the wall collapses to yield a circular surface according to Eq.8.22. The point x_{crit} demarkates regions I and II and its position varies with the z-coordinate in the 3-D profile. As an approximation of the maximum retraction, the x_{crit} with the lowest displacement is determined and this displacement is estimated as the final displacement of the wall.

Fig. 8.8) is always oriented in the direction of the displacement, while F_{pe} (yellow arrow in Fig. 8.8) is oriented against the displacement. The direction of F_{me} (red arrow in Fig. 8.8) is judged from the curvature of the wall, and is oriented against F_{pe} in region III and parallel to F_{pe} in regions I and II. The point where F_{me} changes direction demarkates the regions II and III, and at this point, the curvature (given by $\frac{\partial^2 \xi}{\partial x^2}$) equals 0. Between regions I and II where the direction of F_{me} remains constant, while in region II the magnitude of F_{me} is less than F_{pe}^{max}, in region I F_{me} exceeds F_{pe}^{max}. The point of transition from region I to region II (x_{crit} in Fig. 8.8) corresponds to the point where F_{me} equals F_{pe}^{max}.

In region III, in the presence of the applied voltage the sum of F_{el} and F_{me} equals F_{pe}^{max}, implying $F_{me} < F_{pe}^{max}$. Thus on the removal of the voltage, from the inequality associated with dry friction, the value of F_{pe} in this region reduces from F_{pe}^{max} to reach an equilibrium with the pre-existant F_{me}, and no change in the profile is expected.

In regions I and II, on the removal of the electric field, to establish an equilibrium with F_{me}, F_{pe} is reoriented against F_{me}. In region II (where $|F_{me}| < F_{pe}^{max}$ just as in region III), on the removal of the electric field F_{pe} is reduced to equilibriate itself with F_{me} and the profile remains

unchanged. The equilibrium in regions II and III is hence defined by Eq. 8.21.

$$F_{pe}^{max} > F_{pe} = \sigma \left[\frac{\partial^2 \xi}{\partial x^2} \right] \tag{8.21}$$

In region I, where F$_{me}$ exceeds F$_{pe}^{max}$, the wall is expected to collapse till an equilibrium is reached between F$_{me}$ and F$_{pe}^{max}$ given by the Eq. 8.22, which represents a circle with a radius of curvature 'R$_{crit}$'. The ideal solution calls for a seamless integration of this circle onto the existing profile at the point x$_{crit}$.

$$F_{pe}^{max} = \sigma \left[\frac{\partial^2 \xi}{\partial x^2} \right] \tag{8.22}$$

$$\frac{\partial^2 \xi}{\partial x^2} = \frac{1}{R_{crit}} = \frac{F_{pe}^{max}}{\sigma} \tag{8.23}$$

When considering the arguments given above for the collapsed wall in the case of the 3-D profile, the position of the point x$_{crit}$ would vary for varying values of the z-coordinate, and the circular section would have to be integrated at all x$_{crit}$. As an approximation of the highest retraction, the value of x$_{crit}$ corresponding to the lowest displacement across all values of z is determined, and the wall is assumed to collapse (by Δy, see Fig. 8.8) to retain this displacement on the removal of the voltage. The collapse percentage is calculated as the ratio of the retracted distance to the maximum displacement obtained with the field on (Eq. 8.24).

$$\text{collapse percentage} = \frac{\Delta y}{y_{max}} * 100 \tag{8.24}$$

The collapse percentage is calculated at the surface of the thin film for different film thicknesses (see Fig. 8.9). Thinner films show more retention of the displaced profile in the absence of the applied voltage than thicker films do. With increasing film thickness, through an increase in the ($\frac{\partial^2 y}{\partial z^2}$) term in Eq. 8.22, a heavier 'clamping' of the wall from the lower interface is experienced (as explained previously in Section 8.5), resulting in higher retraction of the wall. For the profiles obtained in the case of single crystals (not shown here), the retained displacement on the removal of the applied voltage for this profile would correspond to 0.35nm, implying negligible retention of the displacement.
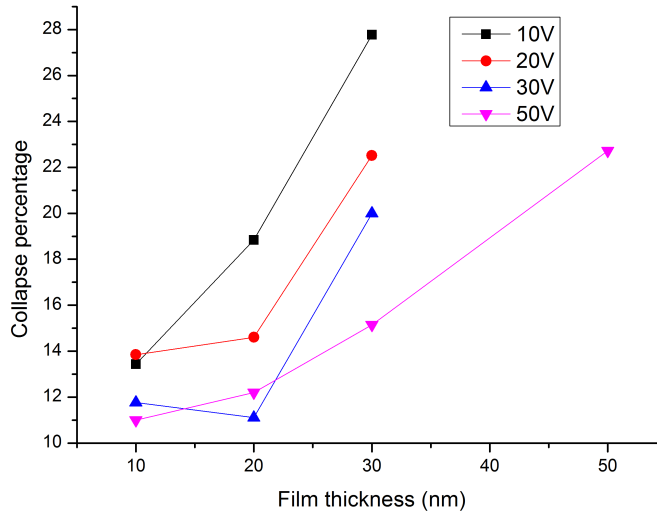
Figure 8.9: The magnitude of retraction of the wall (calculated for a 10nm radius AFM tip placed 10nm away from the initially flat wall) on the removal of the applied voltage represented as a percentage of the maximum displacement of the wall (with the voltage 'on') for various film thicknesses and applied voltages. Under similar conditions, thicker films retain less of the displacement on removal of the field than thinner films.

8.6 Estimation of displacement profiles for PbZrO$_3$

The model was also applied to the ferroelectric APBs in PbZrO$_3$ using the parameters from Table 8.2 under the assumption of isotropic dielectric constant (from measurements on thin films of PbZrO$_3$, see Chapter 6), and with the Peierl's barrier approximated from the values corresponding to 180° walls in BaTiO$_3$, as was done previously. Using the modified parameters it was possible to determine the profiles of the displaced walls in PbZrO$_3$ and plots equivalent to Figs. 8.4 and 8.9 in Section 8.5 were obtained.

Parameter	Numerical Value(s)	Reference
P$_s$	14 μC/cm^2	[153]
σ	190 mJ/m^2	[153]
F$_{Pe}^{max}$	0.05 mJ/m^3	[161]
w	3 nm	[153]
R	10 nm	-
V	10-50 V	-
ϵ_a	200	Chapter 6
ϵ_c	200	Chapter 6

Table 8.2: Table of parameters used for the modelling of displaced APBs in PbZrO$_3$. While most parameters like the wall thickness (w), surface tension (σ), polarisation (P$_s$) and dielectric constants (ϵ_a and ϵ_c) are readily available for APBs in PbZrO$_3$, some values such as Peierl's barrier (F$_{Pe}^{max}$) are approximated from those corresponding to 180° walls in BaTiO$_3$. R and V represent the radius and the applied voltage for the AFM tip respectively.

(a)

(b)

Figure 8.10: Responses from APBs in PbZrO$_3$ calculated for an AFM tip of 10nm radius placed initially 10nm away from the APB. (a) Variation of the maximum displacement as a function of the voltage for various film thicknesses (b) Variation of the collapse percentage as a function of the film thickness for various applied voltages. Both plots showing similar trends as those from APBs in SrTiO$_3$ like material. The higher magnitude of the displacement is related to the lower dielectric constant for PbZrO$_3$ when compared to SrTiO$_3$

The trends seen in the variation of the displacement profiles as well as the collapse percentage with parameters such as voltages and film thickness are similar to those obtained previously for the APBs in an $SrTiO_3$ like material. In the case of $PbZrO_3$, larger displacements are observed when compared to the walls in $SrTiO_3$ like material, and a nearly uniform displacement profile along the entire thicknes is seen in films that are upto 100nm thick (as compared to 50nm from Section 8.5). Despite the higher surface tension for APBs in $PbZrO_3$ (hindering large displacements) when compared to the APBs in $SrTiO_3$ like material, the reason for this increased observed displacement and higher thickness tolerance for the displacement of APBs in $PbZrO_3$ can be traced back to the formulation of the electric field in the thin films, given by Eq.8.19. While the product P_s.w is nearly the same for both $SrTiO_3$ and $PbZrO_3$ cases, the effective dielectric constant ($\sqrt{\epsilon_c.\epsilon_a}$) in the former is almost 30 times higher than the latter, implying lower field magnitude (E $\propto \frac{1}{\sqrt{\epsilon_c.\epsilon_a}}$), resulting in lower displacements. The low dielectric constant of $PbZrO_3$ thus results in a higher field, leading to higher displacements.

8.7   Conclusions

In a configuration containing an AFM tip (with an applied voltage) lying in the vicinity of an APB, the equilibrium between the various forces acting on the wall was determined using variational principles, and through it, the profile of the displaced wall was simulated for an $SrTiO_3$ like material. The displacement of APBs scales almost linearly with voltage (see Fig. 8.4), with thinner films having larger displacements. The profile of the displaced wall is seen to be almost independent of the depth in the case of very thin films (thickness comparable to AFM tip radius, see Fig. 8.6), whereas thicker films showed lower wall displacements(at the surface, and at the lower interface), with single crystals showing almost no displacement at all. Moreover, on the removal of the applied voltage, films with thickness higher than the radius of AFM tip suffer from very large retraction of the displacement (see Fig. 8.9), whereas films with thickness lower than the AFM tip radius, allow for minimal retraction. Single crystals and thick films are, thus, unsuitable for the observation of the mechanical responses from APBs. Meanwhile, in thin films of thickness lower than the AFM tip radius, the displacement achieved is large enough even on the removal of the applied voltage to be observed using Scanning Probe Microscopy techniques. On comparing the responses from APBs in $SrTiO_3$ and $PbZrO_3$ like materials, the latter shows larger displacements (see Fig. 8.10), related to its inherently low dielectric constant.

9 Summary and Outlook

In the search of ferroelectricity in an otherwise antiferroelectric material, the current study contributes to the understanding of the occurence of antiferroelectricity in $PbZrO_3$ from the analysis of the lattice dynamics accompanying the phase transition. Through this comprehension, the possibility of localised ferroelectric behaviour in structural boundaries emerges. To this end, thin films of $PbZrO_3$ were grown and analysed for the control and observation of such localised anomalous behaviour.

The origin of antiferroelectricity in $PbZrO_3$ is explained through a complex interplay between various order parameters participating in the phase transition. By the application of a combination of various scattering techniques such as Inelastic X-Ray, Thermal Diffused and Brillouin scattering, the interaction between these order parameters was analysed. The existance of a repulsive coupling between the transverse acoustic and transverse optic modes in the high temperature phase was observed and explained using flexoelectric coupling. This coupling prevents the manifestation of the ferroelectric phase transition due to the appearance of the structural order parameter. Though the system is very close to an incommensurate instability, it is avoided through the so called 'Umklapp' invariant resulting in the first order phase transition directly into the lock-in phase. The oxygen octahedral rotations accompanying the antiferroelectric phase transition are explained using an attractive biquadratic coupling between the order parameter associated therein and the structural order parameter associated with the antiferroelectric phase, leading to a 'trigger phase transition'. Both the above mentioned interactions can be explained using Landau free energy expansion consisting of a two-mode model. The two mode model explains as well the dielectric anomaly appearing across the phase transition.

Epitaxial thin films of $PbZrO_3$ are grown using Pulsed Laser Deposition on $SrTiO_3$ substrates.

The epitaxial strain is moderated using buffer layers of $BaZrO_3$. By varying the thickness of the buffer layer, the misfit strain experienced by the $PbZrO_3$ film is controlled, and through this, a control on the domain fractions and on the misfit dislocation density is achieved. While compressive strains are shown to stabilise domains oriented along the $(120)_o$ orthorhombic axis, tensile strains are shown to stabilise the $(001)_o$ oriented domains. The variation from one preferential orientation to another is seen to be continous (while passing through a mixture) with a variation in the strain. The use of one single material as a buffer layer providing for a tunable interfacial strain has been demonstrated. Through the control of the interfacial strain a control on the misfit dislocation density in the thin films has been documented.

The grown thin films of $PbZrO_3$ showed typical double hysteresis loops for polarisation-field analyses, as is commonly oberved in antiferroelectric materials. The films also show typical 4-peak behaviour for Capacitance-Field analysis with the peak positions diverging with decreasing temperature. This is associated with a very heavy coupling of ferroelectric and structural order parameters, explained using the same two-mode instability model, and as observed previously from the lattice dynamics as well. These results confirm the antiferroelectric nature of the film. The films undergo a phase transition at ~480K, observed through complimentary use of X-Ray Diffraction, Permittivity and Raman Spectroscopy techniques as a function of temperature. The lowering of the phase transition is possibly related to the residual thermal strain in the film.

Detailed observations carried out on the thin films showed the presence of local polarity along the structural boundaries known as Anti-Phase Boundaries (APBs). These APBs are extremely thin (~3nm) and are oriented parallel to the direction of the lead displacements in the antiferroelectric phase. Both these observations are explained using the lattice dynamics associated with the antiferroelectric phase. Contrarily, the ferroelastic domain walls observed in the thin films are seen to not be restricted to any certain crystallographic direction, as a result of the minimal elastic strain between such ferroelastic domains. While the ferroelastic domain walls are seen to deviate on encountering threading dislocations, the APBs are seen to terminate either at threading dislocations or annihilate as a result of interaction with other APBs.

Following the observation of local ferroelectric properties in the APBs in $PbZrO_3$, their mechanical responses to an external electric field were modelled. Through a voltage applied to an AFM tip placed close to an initially flat wall, a field gradient was produced within a film containing an APB. The displacement of the wall was calculated as a function of the applied voltage and the wall thickness. Increasing applied voltage is shown to result in increased displacement.

For thicker films (thickness larger than AFM tip radius) and single crystals, the calculated displacements were far lower than for thinner films under similar conditions. Furthermore, even the minute displacement is mostly retracted on the removal of the applied voltage in the case of the thicker films and single crystals; while for the thin films, the retraction is shown to be minimal. These observations are explained using the effect of the surface tension along the depth of the film. The above calculations were conducted for an $SrTiO_3$ like material as well as a $PbZrO_3$ like material, and the latter showed larger displacements than the former. The calculated displacements in thin films are sufficiently large for experimental observation using Scanning Probe Microscopy techniques.

In summary, by employing $PbZrO_3$ as a prototypical antiferroelectric material, the current study adds to the understanding of antiferroelectric materials in general by elaborating on the origin of antiferroelectricity in $PbZrO_3$. With the factors leading to the antiferroelectric transition in $PbZrO_3$, the typical properties of antiferroelectrics are explained, while also providing for possible scenarios for the observation of anomalous behaviour such as localised ferroelectricity. Through the growth, characterisation and observation of epitaxial $PbZrO_3$ thin films, the occurence of such local anomalous behaviour is confirmed and their properties simulated.

9.1 Outlook

The observation of such local ferroelectric behaviour may hold potential towards applications in fields such as memory storage. By using the domain wall and not the domain for the elementary bit, the size of the latter can be reduced immensely, thus aiding in increasing the memory storage density, as well its miniaturisation. The implementation of these structures in such applications demands further analysis and observations, a few of which are enlisted below.

For the exploitation of the ferroelectric nature of APBs, the switching properties of the ferroelectric behaviour in APBs would require special attention, for their behaviour might be potentially different from ferroelectric materials owing to the size effects associated with their low thickness. Alongside, the stability of the polarisation with temperature, and in the presence of internal and external depolarising fields is to be estimated, to understand the limiting conditions for the employment of these structures in ferroelectric applications. An understanding of the interactions between APBs is crucial to obtain the conditions of stability for their co-existance, without resulting in annihilation. Borrowing from the results of Chapter

8, observations of the APBs through Scanning Probe Microscopy techniques and their inter-actions with electric fields would allow for the innovation of techniques for the handling of APBs.

Meanwhile, since the discovery of $PbZrO_3$ as the first documented case of antiferroelectricity, hundreds of other materials are currently classified as antiferroelectrics. It would also be of interest to draw parallels to the origin of antiferroelectricity in materials such as $AgNbO_3$ and $NaNbO_3$ which, similarly to $PbZrO_3$, are known to have an unstable ferroelectric mode [163]. The possibility of ferroelectric behaviour in APBs in such materials would be helpful in following the current trend towards lead-free materials in ferroelectric applications. All in all, the present study adds another example to the existing knowledge of various anomalous behaviour observed in domain walls, and contributes directly to the functionalisation of domain walls, aiding them in replacing domains as individual functional entities.

Bibliography

[1] Hiroshi Ishiwara. Ferroelectric random access memories. *Journal of nanoscience and nanotechnology*, 12(10):7619–7627, 2012.

[2] Marc-Alexandre Dubois and Paul Muralt. Properties of aluminum nitride thin films for piezoelectric transducers and microwave filter applications. *Applied Physics Letters*, 74(20):3032–3034, 1999.

[3] Nicolas Ledermann, Jacek Baborowski, Andreas Seifert, Bert Willing, Stephane Hiboux, Paul Muralt, Nava Setter, and Martin Forster. Piezoelectric cantilever microphone for photoacoustic gas detector. *Integrated Ferroelectrics*, 35(1-4):177–184, 2001.

[4] Jacek Baborowski, Nicolas Ledermann, Paul Muralt, and Daniel Schmitt. Simulation and characterization of piezoelectric micromachined ultrasonic transducers (PMUT's) based on PZT/SOI membranes. *Integrated Ferroelectrics*, 54(1):557–564, 2003.

[5] Spartak S Gevorgian and Erik Ludvig Kollberg. Do we really need ferroelectrics in paraelectric phase only in electrically controlled microwave devices? *Microwave Theory and Techniques, IEEE Transactions on*, 49(11):2117–2124, 2001.

[6] N Setter, D Damjanovic, L Eng, G Fox, Spartak Gevorgian, S Hong, A Kingon, H Kohlstedt, NY Park, GB Stephenson, et al. Ferroelectric thin films: Review of materials, properties, and applications. *Journal of Applied Physics*, 100(5):051606, 2006.

[7] C. Kittel. Theory of antiferroelectric crystals. *Physical Review*, 82(5):729, 1951.

[8] Etsuro Sawaguchi, Gen Shirane, and Yutaka Takagi. Phase transition in lead zirconate. *Journal of the Physical Society of Japan*, 6(5):333–339, 1951.

[9] CNW Darlington. The primary order parameter in antiferroelectric $NaNbO_3$. *Solid State Communications*, 29(3):307–311, 1979.

Bibliography

[10] JW Goodby and E Chin. A chiral induced ferroelectric liquid crystal phase transition with a vanishingly small enthalpy. *Liquid Crystals*, 3(9):1245–1254, 1988.

[11] John W Goodby, Jay S Patel, and Evylen Chin. Ferroelectric, ferrielectric and antiferro-electric properties in the (r)-and (s)-1-methylalkyl 4'-(4'-n-alkoxybenzoyloxy) biphenyl-4-carboxylate liquid crystals. *J. mater. Chem.*, 2(2):197–207, 1992.

[12] ADL Chandani, Ewa Gorecka, Yukio Ouchi, Hideo Takezoe, and Atsuo Fukuda. Anti-ferroelectric chiral smectic phases responsible for the trislable switching in MHPOBC. *Japanese journal of applied physics*, 28(7A):L1265, 1989.

[13] J Lasave, S Koval, NS Dalal, and RL Migoni. Origin of antiferroelectricity in $NH_4H_2PO_4$ from first principles. *Physical review letters*, 98(26):267601, 2007.

[14] Christoph G Salzmann, Paolo G Radaelli, Erwin Mayer, and John L Finney. Ice XV: A new thermodynamically stable phase of ice. *Physical review letters*, 103(10):105701, 2009.

[15] Masahiro Johno, Keizou Itoh, Ji Lee, Yukio Ouchi, Hideo Takezoe, Atsuo Fukuda, and To-moya Kitazume. Temporal and spatial behavior of the field-induced transition between antiferroelectric and ferroelectric phases in chiral smectics. *Japanese Journal of Applied Physics*, 29(1A):L107, 1990.

[16] Hideo Takezoe, Ewa Gorecka, and Mojca Čepič. Antiferroelectric liquid crystals: Inter-play of simplicity and complexity. *Reviews of Modern Physics*, 82(1):897, 2010.

[17] B Noheda. Structure and high-piezoelectricity in lead oxide solid solutions. *Current Opinion in Solid State and Materials Science*, 6(1):27–34, 2002.

[18] Yasuyoshi Saito, Hisaaki Takao, Toshihiko Tani, Tatsuhiko Nonoyama, Kazumasa Taka-tori, Takahiko Homma, Toshiatsu Nagaya, and Masaya Nakamura. Lead-free piezoce-ramics. *Nature*, 432(7013):84–87, 2004.

[19] AS Mischenko, Qi Zhang, JF Scott, RW Whatmore, and ND Mathur. Giant electrocaloric effect in thin-film $PbZr_{0.95}Ti_{0.05}O_3$. *Science*, 311(5765):1270–1271, 2006.

[20] Shan-Tao Zhang, Alain B Kounga, Wook Jo, Christine Jamin, Klaus Seifert, Torsten Granzow, Jürgen Rödel, and Dragan Damjanovic. High-strain lead-free antiferroelectric electrostrictors. *Advanced Materials*, 21(46):4716–4720, 2009.

[21] Baomin Xu, L Eric Cross, and Jonathan J Bernstein. Ferroelectric and antiferroelectric films for microelectromechanical systems applications. *Thin Solid Films*, 377:712–718, 2000.

[22] CD Campbell, Jacobus Daniel Van Wyk, and Rengang Chen. Experimental and theoretical characterization of an antiferroelectric ceramic capacitor for power electronics. *Components and Packaging Technologies, IEEE Transactions on*, 25(2):211–216, 2002.

[23] Joseph P Dougherty. Cardiac defibrillator with high energy storage antiferroelectric capacitor, August 13 1996. US Patent 5,545,184.

[24] Alexander Kirillovich Tagantsev, L Eric Cross, and Jan Fousek. *Domains in ferroic crystals and thin films*. Springer, 2010.

[25] J.F. Scott and C.A. Paz de Araujo. Ferroelectric memories. *Science*, 246(4936):1400, 1989.

[26] JF Scott. Applications of modern ferroelectrics. *science*, 315(5814):954–959, 2007.

[27] G. Shirane, E. Sawaguchi, and Y. Takagi. Dielectric properties of lead zirconate. *Physical Review*, 84(3):476, 1951.

[28] H. Maniwa E. Sawaguchi and S. Hoshino. Antiferroelectric structure of lead zirconate. *Physical Review*, 83:1078, 1951.

[29] F Jona, G Shirane, F Mazzi, and R Pepinsky. X-ray and neutron diffraction study of antiferroelectric lead zirconate, $PbZrO_3$. *Physical Review*, 105(3):849, 1957.

[30] H. Fujishita and S. Hoshino. A study of structural phase transitions in antiferroelectric $PbZrO_3$ by neutron diffraction. *Journal of the Physical Society of Japan*, 53(1):226–234, 1984.

[31] W. Cochran and A. Zia. Structure and dynamics of perovskite-type crystals. *Physica Status Solidi (b)*, 25(1):273–283, 1968.

[32] RW Whatmore and AM Glazer. Structural phase transitions in lead zirconate. *Journal of Physics C: Solid State Physics*, 12:1505, 1979.

[33] AE Pasto and RA Condrate Sr. Raman spectrum of $PbZrO_3$. *Journal of the American Ceramic Society*, 56(8):436–438, 1973.

[34] G. Kugel, I. Jankowska-Sumara, S. Roleder, and J. Dec. High temperature raman light scattering in $PbZrO_3$ single crystals. *JOURNAL-KOREAN PHYSICAL SOCIETY*, 32:581–583, 1998.

[35] J. Handerek. Electric conductivity and dielectric absorption phenomena in Lead Zirconate ceramics. *Physica Status Solidi (b)*, 21(1):323–329, 1967.

Bibliography

[36] D. Viehland. Transmission electron microscopy study of high-Zr-content Lead Zirconate Titanate. *Physical Review B*, 52(2):778, 1995.

[37] Zhengkui Xu, Xunhu Dai, Dwight Viehland, David A Payne, Zhuang Li, and Yendao Jiang. Ferroelectric domains and incommensuration in the intermediate phase region of lead zirconate. *Journal of the American Ceramic Society*, 78(8):2220–2224, 1995.

[38] K. Roleder and J. Dee. The defect-induced ferroelectric phase in thin $PbZrO_3$ single crystals. *Journal of Physics: Condensed Matter*, 1:1503, 1989.

[39] Bernard Jaffe. Antiferroelectric ceramics with field-enforced transitions: a new nonlinear circuit element. *Proceedings of the IRE*, 49(8):1264–1267, 1961.

[40] Etsuro Sawaguchi. Ferroelectricity versus antiferroelectricity in the solid solutions of $PbZrO_3$ and $PbTiO_3$. *Journal of the Physical Society of Japan*, 8(5):615–629, 1953.

[41] AP DeBretteville Jr. Threshold field and free energy for the antiferroelectric-ferroelectric phase transition in lead zirconate. *Physical Review*, 94(5):1125, 1954.

[42] NG Leont'ev, RV Kolesova, OE Fesenko, and VG Smotrakov. X-ray structural investigation of electric-field-induced orthorhombic phase of lead zirconate. *Sov. Phys. Crystallogr*, 29:240–241, 1984.

[43] Lucian Pintilie, Ksenia Boldyreva, Marin Alexe, and Dietrich Hesse. Coexistence of ferro-electricity and antiferroelectricity in epitaxial $PbZrO_3$ films with different orientations. *Journal of Applied Physics*, 103(2):024101–024101, 2008.

[44] K Yamakawa, S Trolier-McKinstry, and JP Dougherty. Preparation of lead zirconate titanate thin films by reactive magnetron co-sputtering. *Materials letters*, 28(4):317–322, 1996.

[45] Robert Blinc and Boštjan Žekš. *Soft modes in ferroelectrics and antiferroelectrics*. North-Holland Publishing Company Amsterdam, 1974.

[46] M.E. Lines and A.M. Glass. *Principles and applications of ferroelectrics and related materials*. Oxford University Press, USA, 2001.

[47] C Haas. Phase transitions in ferroelectric and antiferroelectric crystals. *Physical Review*, 140(3A):A863, 1965.

[48] T. Ostapchuk, J. Petzelt, V. Zelezny, S. Kamba, V. Bovtun, V. Porokhonskyy, A. Pashkin, P. Kuzel, MD Glinchuk, IP Bykov, et al. Polar phonons and central mode in antiferroelectric $PbZrO_3$ ceramics. *Journal of Physics: Condensed Matter*, 13:2677, 2001.

[49] J Baedi, SM Hosseini, A Kompany, and E Attaran Kakhki. Structural, electronic and optical properties of lead zirconate. *physica status solidi (b)*, 245(11):2572–2580, 2008.

[50] T. Ostapchuk, J. Petzelt, V. Zelezny, S. Kamba, B. Malic, M. Kosec, L. Cakare, K. Roleder, and J. Dec. Infrared spectroscopy of lead zirconate single crystal, ceramics and films. *Ferroelectrics*, 239(1):979–986, 2000.

[51] T Egami, S Teslic, W Dmowski, PK Davies, IW Chen, and H Chen. Microscopic origin of relaxor ferroelectricity in PMN and PLZT. *Journal-Korean Physical Society*, 32:S935–S938, 1998.

[52] U.V. Waghmare and K.M. Rabe. Lattice instabilities, anharmonicity & phase transitions in $PbZrO_3$ from first principles. In *APS Meeting Abstracts*, volume 1, page 2402, 1996.

[53] Ph Ghosez, E Cockayne, UV Waghmare, and KM Rabe. Lattice dynamics of $BaTiO_3$, $PbTiO_3$, and $PbZrO_3$: a comparative first-principles study. *Physical Review B: Condensed Matter and Materials Physics*, 60(2):836–843, 1999.

[54] Stanislav Kamba, Elena Buixaderas, Tetyana Ostapchuk, and Jan Petzelt. Ferroelectric soft modes and dynamic central modes near some phase transitions. *Ferroelectrics*, 268(1):163–168, 2002.

[55] W. Zhong and D. Vanderbilt. Competing structural instabilities in cubic perovskites. *Physical review letters*, 74(13):2587–2590, 1995.

[56] E. V. Balashova and A. K. Tagantsev. Polarization response of crystals with structural and ferroelectric instabilities. *Phys. Rev. B*, 48:9979–9986, Oct 1993.

[57] EV Balashova, VV Lemanov, AK Tagantsev, AB Sherman, and S.H. Shomuradov. Betaine arsenate as a system with two instabilities. *Physical Review B*, 51(14):8747, 1995.

[58] A. Yamanaka, M. Kataoka, Y. Inaba, K. Inoue, B. Hehlen, and E. Courtens. Evidence for competing orderings in strontium titanate from hyper-Raman scattering spectroscopy. *EPL (Europhysics Letters)*, 50:688, 2000.

[59] A.K. Tagantsev, E. Courtens, and L. Arzel. Prediction of a low-temperature ferroelectric instability in antiphase domain boundaries of strontium titanate. *Physical Review B*, 64(22):224107, 2001.

[60] Hiromoto Uwe and Tunetaro Sakudo. Stress-induced ferroelectricity and soft phonon modes in $SrTiO_3$. *Physical Review B*, 13(1):271, 1976.

Bibliography

[61] Wenwu Cao and Gerhard R Barsch. Landau-ginzburg model of interphase boundaries in improper ferroelastic perovskites of D4h18 symmetry. *Physical Review B*, 41(7):4334, 1990.

[62] Jill Guyonnet. *Electrical Conduction at 180° Ferroelectric Domain Walls*. Springer Theses. Springer International Publishing, 2014.

[63] Sandra Van Aert, Stuart Turner, Remi Delville, Dominique Schryvers, Gustaaf Van Tendeloo, and Ekhard KH Salje. Direct observation of ferrielectricity at ferroelastic domain boundaries in CaTiO$_3$ by electron microscopy. *Advanced Materials*, 24(4):523–527, 2012.

[64] Liliana Goncalves-Ferreira, Simon AT Redfern, Emilio Artacho, and Ekhard KH Salje. Ferrielectric twin walls in CaTiO$_3$. *Physical review letters*, 101(9):097602, 2008.

[65] F. Jona, G. Shirane, and R. Pepinsky. Optical study of PbZrO$_3$ and NaNbO$_3$ single crystals. *Physical Review*, 97(6):1584, 1955.

[66] L Goulpeau. 2 phase transitions in lead zirconate, 1967.

[67] M. Tanaka, R. Saito, and K. Tsuzuki. Electron microscopic studies on domain structure of PbZrO$_3$. *Japanese Journal of Applied Physics*, 21:291, 1982.

[68] Sang Ho Oh and Chan Gyung Park. Misfit strain relaxation by dislocations in SrRuO$_3$/SrTiO$_3$ (001) heteroepitaxy. *Journal of applied physics*, 95(9):4691–4704, 2004.

[69] Sang Ho Oh, Ju Hyung Suh, and Chan Gyung Park. Defects in strained epitaxial SrRuO$_3$ films on SrTiO$_3$ substrates. *Materials transactions*, 48(10):2556, 2007.

[70] JA Venables, GI Price, and JW Matthews. Epitaxial growth-part a. *B, Chapt*, 4:387, 1975.

[71] JE Greene. *Physics of film growth from the vapor phase*. Springer, 1993.

[72] Douglas B Chrisey and Graham K Hubler. *Pulsed laser deposition of thin films*, volume 1. 2003.

[73] David Anthony King and DP Woodruff. *Growth and properties of ultrathin epitaxial layers*. Elsevier, 1997.

[74] J.W. Matthews and A.E. Blakeslee. Defects in epitaxial multilayers: I. misfit dislocations. *Journal of Crystal Growth*, 27(0):118 – 125, 1974.

[75] PA Langjahr, FF Lange, T Wagner, and M Rühle. Lattice mismatch accommodation in perovskite films on perovskite substrates. *Acta materialia*, 46(3):773–785, 1998.

[76] Tomoaki Yamada, Konstantin F. Astafiev, Vladimir O. Sherman, Alexander K. Tagantsev, Dong Su, Paul Muralt, and Nava Setter. Structural and dielectric properties of strain-controlled epitaxial $SrTiO_3$ thin films by two-step growth technique. *Journal of Applied Physics*, 98(5):054105, 2005.

[77] Toshimasa Suzuki, Yuji Nishi, and Masayuki Fujimoto. Defect structure in homoepitaxial non-stoichiometric strontium titanate thin films. *Philosophical Magazine A*, 80(3):621–637, 2000.

[78] JS Speck, A Seifert, W Pompe, and R Ramesh. Domain configurations due to multiple misfit relaxation mechanisms in epitaxial ferroelectric thin films. ii. experimental verification and implications. *Journal of applied physics*, 76(1):477–483, 1994.

[79] YY Liu, ZX Zhu, J-F Li, and JY Li. Misfit strain modulated phase structures of epitaxial $Pb(Zr_{1-x}Ti_x)O_3$ thin films: The effect of substrate and film thickness. *Mechanics of Materials*, 42(8):816–826, 2010.

[80] V Nagarajan, IG Jenkins, SP Alpay, H Li, S Aggarwal, L Salamanca-Riba, AL Roytburd, and R Ramesh. Thickness dependence of structural and electrical properties in epitaxial lead zirconate titanate films. *Journal of applied physics*, 86(1):595–602, 1999.

[81] RJ Zeches, MD Rossell, JX Zhang, AJ Hatt, Q He, C-H Yang, A Kumar, CH Wang, A Melville, C Adamo, et al. A strain-driven morphotropic phase boundary in $BiFeO_3$. *science*, 326(5955):977–980, 2009.

[82] Ayan Roy Chaudhuri, Miryam Arredondo, Angelika Hähnel, Alessio Morelli, Michael Becker, Marin Alexe, and Ionela Vrejoiu. Epitaxial strain stabilization of a ferroelectric phase in $PbZrO_3$ thin films. *Phys. Rev. B*, 84:054112, Aug 2011.

[83] Y Wang, C Ganpule, BT Liu, H Li, K Mori, B Hill, M Wuttig, R Ramesh, J Finder, Z Yu, et al. Epitaxial ferroelectric $Pb(Zr,Ti)O_3$ thin films on si using $SrTiO_3$ template layers. *Applied physics letters*, 80(1):97–99, 2002.

[84] SB Mi, CL Jia, MI Faley, U Poppe, and K Urban. High-resolution electron microscopy of microstructure of $SrTiO_3/BaZrO_3$ bilayer thin films on MgO substrates. *Journal of crystal growth*, 300(2):478–482, 2007.

[85] Jun Ki Chung, Won Jeong Kim, Sung Gap Lee, and Cheol Jin Kim. Growth and characterization of bazro3 buffer layer for textured ybco thin films growth on mgo (00l) substrate. *Key Engineering Materials*, 336:715–718, 2007.

[86] Masashi Mukaida, Yuya Yamazaki, Yuki Shingai, Sayoko Makino, Masanobu Kusunoki, Atsushi Saito, and Shigetoshi Ohshima. Surface resistance of YBa$_2$Cu$_3$O$_{7-\delta}$ thin films on MgO lattice-matched BaZrO$_3$ buffer layers. *Superconductor Science and Technology*, 17(3):337, 2004.

[87] Y Kitano, T Matsui, N Fujimura, K Morii, and T Ito. Thin film crystal growth of BaZrO$_3$ at low oxygen partial pressure. *Journal of crystal growth*, 243(1):164–169, 2002.

[88] GR Bai, HLM Chang, DJ Lam, and Y Gao. Preparation and structure of PbZrO$_3$ epitaxial films by metalorganic chemical vapor deposition. *Applied physics letters*, 62(15):1754–1756, 1993.

[89] VR Palkar, S. Chattopadhyay, SC Purandare, SG Lokhre, R. Pinto, and MS Multani. Oriented single phase PbZrO$_3$ thin films on Si (100) substrate using aqueous sol with rapid thermal annealing. *Materials Letters*, 33(1-2):1–5, 1997.

[90] Xin-Gui Tang, Jie Wang, Xiao-Xing Wang, and Helen Lai-Wah Chan. Electrical properties of highly (111)-oriented lead zirconate thin films. *Solid state communications*, 130(6):373–377, 2004.

[91] Zhenfang Tang and Xingui Tang. Structural, dielectric and optical properties of highly oriented lead zirconate thin films prepared by sol–gel process. *Materials chemistry and physics*, 80(1):294–298, 2003.

[92] K Yamakawa, K Wa Gachigi, S Trolier-McKinstry, and JP Dougherty. Structural and electrical properties of antiferroelectric lead zirconate thin films prepared by reactive magnetron co-sputtering. *Journal of materials science*, 32(19):5169–5176, 1997.

[93] IW Kim, JH Jeong, K Yamakawa, SB Bae, HK Kim, and KS Kim. Characteristics of antiferroelectric PbZrO$_3$ thin films. *J. Korean Phys. Soc.*, 33:180–184, 1998.

[94] TD Kang, Hosun Lee, G Xing, N Izumskaya, V Avrutin, B Xiao, and H Morkoc. Dielectric functions and critical points of PbTiO$_3$, PbZrO$_3$, and PbZr$_{0.57}$Ti$_{0.43}$O$_3$ grown on SrTiO$_3$ substrate. *Applied physics letters*, 91(2):022918–022918, 2007.

[95] P. Ayyub, S. Chattopadhyay, R. Pinto, and MS Multani. Ferroelectric behavior in thin films of antiferroelectric materials. *Physical Review B*, 57(10):5559–5562, 1998.

[96] SSN Bharadwaja and SB Krupanidhi. Dielectric and dc electrical studies of antiferroelectric lead zirconate thin films. *Materials Science and Engineering B*, 78(1):1–10, 2000.

[97] SSN Bharadwaja and SB Krupanidhi. Study of ac electrical properties in multigrain antiferroelectric lead zirconate thin films. *Thin solid films*, 391(1):126–132, 2001.

[98] K. Boldyreva, D. Bao, G. Le Rhun, L. Pintilie, M. Alexe, and D. Hesse. Microstructure and electrical properties of (120)-oriented and of (001)-oriented epitaxial antiferroelectric PbZrO$_3$ thin films on (100) SrTiO$_3$ substrates covered with different oxide bottom electrodes. *Journal of Applied Physics*, 102:044111, 2007.

[99] Soma Chattopadhyay, Pushan Ayyub, VR Palkar, MS Multani, SP Pai, SC Purandare, and R Pinto. Dielectric properties of oriented thin films of PbZrO$_3$ on Si produced by pulsed laser ablation. *Journal of applied physics*, 83(12):7808–7812, 1998.

[100] Isaku Kanno, Shigenori Hayashi, Masatoshi Kitagawa, Ryouichi Takayama, and Takashi Hirao. Antiferroelectric PbZrO$_3$ thin films prepared by multi-ion-beam sputtering. *Applied physics letters*, 66(2):145–147, 1995.

[101] WY Pan, CQ Dam, QM Zhang, and LE Cross. Large displacement transducers based on electric field forced phase transitions in the tetragonal (Pb$_{0.97}$La$_{0.02}$)(Ti, Zr, Sn) O$_3$ family of ceramics. *Journal of applied physics*, 66(12):6014–6023, 1989.

[102] Sebastian E Reyes-Lillo and Karin M Rabe. Antiferroelectricity and ferroelectricity in epitaxially strained PbZrO$_3$ from first principles. *Physical Review B*, 88(18):180102, 2013.

[103] I. Vrejoiu, G. Le Rhun, ND Zakharov, D. Hesse, L. Pintilie, and M. Alexe. Threading dislocations in epitaxial ferroelectric PbZr$_{0.2}$Ti$_{0.8}$O$_3$ films and their effect on polarization backswitching. *Philosophical Magazine*, 86(28):4477–4486, 2006.

[104] Peng Gao, Christopher T Nelson, Jacob R Jokisaari, Seung-Hyub Baek, Chung Wung Bark, Yi Zhang, Enge Wang, Darrell G Schlom, Chang-Beom Eom, and Xiaoqing Pan. Revealing the role of defects in ferroelectric switching with atomic resolution. *Nature communications*, 2:591, 2011.

[105] SP Alpay, IB Misirlioglu, V Nagarajan, and R Ramesh. Can interface dislocations degrade ferroelectric properties? *Applied physics letters*, 85(11):2044–2046, 2004.

[106] Peter Maksymovych, Nina Balke, Stephen Jesse, Mark Huijben, Ramamoorthy Ramesh, Arthur P Baddorf, and Sergei V Kalinin. Defect-induced asymmetry of local hysteresis loops on BiFeO$_3$ surfaces. *Journal of materials science*, 44(19):5095–5101, 2009.

[107] M Kawai, D Kan, S Isojima, H Kurata, S Isoda, Y Shimakawa, S Kimura, and O Sakata. Critical thickness control by deposition rate for epitaxial BaTiO$_3$ thin films grown on SrTiO$_3$ (001). *Journal of Applied Physics*, 102(11):114311, 2007.

[108] Y Lin and CL Chen. Interface effects on highly epitaxial ferroelectric thin films. *Journal of materials science*, 44(19):5274–5287, 2009.

[109] ZR Zytkiewicz. Laterally overgrown structures as substrates for lattice mismatched epitaxy. *Thin Solid Films*, 412(1):64–75, 2002.

[110] MA Moram, MJ Kappers, ZH Barber, and CJ Humphreys. Growth of low dislocation density GaN using transition metal nitride masking layers. *Journal of crystal growth*, 298:268–271, 2007.

[111] Howard M Smith and AF Turner. Vacuum deposited thin films using a ruby laser. *Applied Optics*, 4(1):147–148, 1965.

[112] JT Cheung and T Magee. Recent progress on LADA growth of HgCdTe and CdTe epitaxial layers. *Journal of Vacuum Science & Technology A*, 1(3):1604–1607, 1983.

[113] James G Lunney. Pulsed laser deposition of metal and metal multilayer films. *Applied surface science*, 86(1):79–85, 1995.

[114] S Witanachchi, HS Kwok, XW Wang, and DT Shaw. Deposition of superconducting Y-Ba-Cu-O films at 400C without post-annealing. *Applied physics letters*, 53(3):234–236, 1988.

[115] JS Horwitz, KS Grabowski, DB Chrisey, and RE Leuchtner. Insitu deposition of epitaxial $PbZr_xTi_{1-x}O_3$ thin films by pulsed laser deposition. *Applied physics letters*, 59(13):1565–1567, 1991.

[116] AJ Paul, DW Bonnell, JW Hastie, PK Schenck, RD Shull, and JJ Ritter. In situ characterization of the pulsed laser deposition of magnetic thin films. In *MRS Proceedings*, volume 235, page 867. Cambridge Univ Press, 1991.

[117] Douglas H Lowndes, DB Geohegan, AA Puretzky, DP Norton, and CM Rouleau. Synthesis of novel thin-film materials by pulsed laser deposition. *Science*, 273(5277):898–903, 1996.

[118] RF Xiao, HB Liao, N Cue, XW Sun, and HS Kwok. Growth of c-axis oriented gallium nitride thin films on an amorphous substrate by the liquid-target pulsed laser deposition technique. *Journal of applied physics*, 80(7):4226–4228, 1996.

[119] F. Sette, G. Ruocco, M. Krisch, U. Bergmann, C. Masciovecchio, V. Mazzacurati, G. Signorelli, and R. Verbeni. Collective dynamics in water by high energy resolution inelastic x-ray scattering. *Phys. Rev. Lett.*, 75:850–853, Jul 1995.

[120] Alfred QR Baron. Phonons in crystals using inelastic x-ray scattering. *arXiv preprint arXiv:0910.5764*, 2009.

[121] R. Xu and T.C. Chiang. Determination of phonon dispersion relations by x-ray thermal diffuse scattering. *Zeitschrift für Kristallographie*, 220(12/2005):1009–1016, 2005.

[122] G Turrell, DJ Gardiner, and PR Graves. Practical Raman Spectroscopy. *Gardiner, DJ*, 1989.

[123] MS Hegde. Epitaxial oxide thin films by pulsed laser deposition: Retrospect and prospect. *Journal of Chemical Sciences*, 113(5-6):445–458, 2001.

[124] David B Williams and C Barry Carter. *The Transmission Electron Microscope*. Springer, 1996.

[125] CL Jia, M Lentzen, and K Urban. Atomic-resolution imaging of oxygen in perovskite ceramics. *Science*, 299(5608):870–873, 2003.

[126] Knut Urban, Bernd Kabius, Max Haider, and Harald Rose. A way to higher resolution: spherical-aberration correction in a 200 kV transmission electron microscope. *Journal of Electron Microscopy*, 48(6):821–826, 1999.

[127] Chun-Lin Jia, Shao-Bo Mi, Knut Urban, Ionela Vrejoiu, Marin Alexe, and Dietrich Hesse. Atomic-scale study of electric dipoles near charged and uncharged domain walls in ferroelectric films. *Nature materials*, 7(1):57–61, 2007.

[128] Jose Manoel Balthazar, Angelo Marcelo Tusset, Atila Madureira Bueno, and Bento Rodrigues de Pontes Junior. *Chapter "On an Overview of Nonlinear and Chaotic Behavior and Their Controls of an Atomic Force Microscopy (AFM) Vibrating Problem" in "Nonlinearity, Bifurcation and Chaos- Theory and Applications"*. InTech, 2012.

[129] Rainer Waser, Ulrich Böttger, and Stephan Tiedke. *Polar oxides*. Wiley Online Library, 2005.

[130] J. Holakovsky. A new type of the ferroelectric phase transition. *Physica Status Solidi (b)*, 56(2):615–619, 1973.

[131] Walther Rehwald. The study of structural phase transitions by means of ultrasonic experiments. *Advances in Physics*, 22(6):721–755, 1973.

[132] E Buixaderas, S Kamba, and J Petzelt. Lattice dynamics and central-mode phenomena in the dielectric response of ferroelectrics and related materials. *Ferroelectrics*, 308(1):131–192, 2004.

[133] T Riste, EJ Samuelsen, KT Otnes, and J Feder. Critical behaviour of $SrTiO_3$ near the 105K phase transition. *Solid state communications*, 9(17):1455–1458, 1971.

[134] A.D. Bruce and R.A. Cowley. *Structural phase transitions*. Taylor & Francis monographs on physics. Taylor and Francis, 1981.

[135] JD Axe, J. Harada, and G. Shirane. Anomalous acoustic dispersion in centrosymmetric crystals with soft optic phonons. *Physical Review B*, 1(3):1227, 1970.

[136] E Farhi, AK Tagantsev, R Currat, B Hehlen, E Courtens, and LA Boatner. Low energy phonon spectrum and its parameterization in pure $KTaO_3$ below 80K. *The European Physical Journal B-Condensed Matter and Complex Systems*, 15(4):615–623, 2000.

[137] G. Shirane, JD Axe, J. Harada, and JP Remeika. Soft ferroelectric modes in lead titanate. *Physical Review B*, 2(1):155, 1970.

[138] V. G. Vaks. *Introduction to the Microscopic Theory of Ferroelectrics*. Nauka, Moscow, 1973.

[139] R. A. Cowley. Lattice dynamics and phase transitions of strontium titanate. *Phys. Rev.*, 134:A981–A997, May 1964.

[140] PV Yudin, R Ahluwalia, and AK Tagantsev. Upper bounds for flexoelectric coefficients in ferroelectrics. *Applied Physics Letters*, 104(8):082913, 2014.

[141] DL Corker, AM Glazer, J Dec, K Roleder, and RW Whatmore. A re-investigation of the crystal structure of the perovskite $PbZrO_3$ by x-ray and neutron diffraction. *Acta Crystallographica Section B: Structural Science*, 53(1):135–142, 1997.

[142] Igor A. Kornev and L. Bellaiche. Nature of the ferroelectric phase transition in multiferroic $BiFeO_3$ from first principles. *Phys. Rev. B*, 79:100105, Mar 2009.

[143] Masashi Kawasaki, Kazuhiro Takahashi, Tatsuro Maeda, Ryuta Tsuchiya, Makoto Shinohara, Osamu Ishiyama, Takuzo Yonezawa, Mamoru Yoshimoto, and Hideomi Koinuma. Atomic control of the $SrTiO_3$ crystal surface. *Science*, 266(5190):1540–1542, 1994.

[144] A Okazaki and M Kawaminami. Lattice constant of strontium titanate at low temperatures. *Materials Research Bulletin*, 8(5):545–550, 1973.

[145] Yusheng Zhao and Donald J Weidner. Thermal expansion of $SrZrO_3$ and $BaZrO_3$ perovskites. *Physics and chemistry of minerals*, 18(5):294–301, 1991.

[146] SV Ghaisas and A Madhukar. Kinetic aspects of growth front surface morphology and defect formation during molecular-beam epitaxy growth of strained thin films. *Journal of Vacuum Science & Technology B*, 7(2):264–268, 1989.

[147] Jasprit Singh, KK Bajaj, and S Dudley. Formation of misfit and threading dislocations in molecular-beam epitaxy grown strained layer epitaxy: Role of growth modes. *Journal of Vacuum Science & Technology B*, 5(4):1167–1170, 1987.

[148] AK Tagantsev, M Landivar, E Colla, and N Setter. Identification of passive layer in ferroelectric thin films from their switching parameters. *Journal of applied physics*, 78(4):2623–2630, 1995.

[149] NA Pertsev, AG Zembilgotov, and AK Tagantsev. Equilibrium states and phase transitions in epitaxial ferroelectric thin films. *Ferroelectrics*, 223(1):79–90, 1999.

[150] Soma Chattopadhyay, AR Teren, Jin-Ha Hwang, TO Mason, and BW Wessels. Diffuse phase transition in epitaxial $BaTiO_3$ thin films. *Journal of materials research*, 17(03):669–674, 2002.

[151] Kyoung Jin Choi, M Biegalski, YL Li, A Sharan, J Schubert, R Uecker, P Reiche, YB Chen, XQ Pan, V Gopalan, et al. Enhancement of ferroelectricity in strained $BaTiO_3$ thin films. *Science*, 306(5698):1005–1009, 2004.

[152] JH Haeni, P Irvin, W Chang, R Uecker, P Reiche, YL Li, S Choudhury, W Tian, ME Hawley, B Craigo, et al. Room-temperature ferroelectricity in strained $SrTiO_3$. *Nature*, 430(7001):758–761, 2004.

[153] Xian-Kui Wei, Alexander K Tagantsev, Alexander Kvasov, Krystian Roleder, Chun-Lin Jia, and Nava Setter. Ferroelectric translational antiphase boundaries in nonpolar materials. *Nature communications*, 5, 2014.

[154] GA Smolenskii, VA Isupov, NN Krainik, RE Pasinkov, and AI Sokolov. Ferroelectrics and Related Materials Gordon and Breach, New York, 1984. 2 LE Cross. *Ferroelectrics*, 76:241, 1987.

[155] Bagdasarov KhS. Polkhovskaya TM. Meleshina VA., Indenbom VL. Domain boundaries, antiphase boundaries, and dislocations in gadolinium molybdate single crystals. *Kristallografiya*, 18(6):1218–26, 1973.

[156] JR Barkley and W Jeitschko. Antiphase boundaries and their interactions with domain walls in ferroelastic-ferroelectric $Gd_2(MoO_4)_3$. *Journal of Applied Physics*, 44(3):938–944, 1973.

[157] M Molotskii. Generation of ferroelectric domains in atomic force microscope. *Journal of applied physics*, 93(10):6234–6237, 2003.

[158] William Ralph Smythe and William R Smythe. *Static and dynamic electricity*, volume 3. McGraw-Hill New York, 1950.

[159] Nikolaj Nikolaevich Lebedev, IP Skalskaya, and Ya S Uflyand. Problems in mathematical physics. 1966.

[160] VA Zhirnov. On the theory of the domain walls of ferroelectrics zh. eksp. teor. fiz. 35 1175–80 zhirnov va 1958 sov. phys. *JETP*, 8:822–7, 1958.

[161] EV Burtsev and SP Chervonobrodov. Some problems of 180-switching in ferroelectrics. *Ferroelectrics*, 45(1):97–106, 1982.

[162] KA Müller and H Burkard. SrTiO$_3$: An intrinsic quantum paraelectric below 4K. *Physical Review B*, 19(7):3593, 1979.

[163] Karin M Rabe. Antiferroelectricity in oxides: a reexamination. *Functional Metal Oxides: New Science and Novel Applications*, pages 221–244, 2013.

दीर्घो बुद्धिमतो बाहू ।

The hands of the one with brains are long indeed.

—mahābhārata, vidūra uvāca, 8

Kaushik Vaideeswaran

Avenue Mon Repos 4
1005 Lausanne
Switzerland
✆ *+41 (0)78 626 4166*
✉ *kaushik.vaideeswaran@epfl.ch*
in *kvaideeswaran*
Date of Birth: 22 December, 1988

- Ph.D. in Materials Science from EPFL, Lausanne
- In-depth knowledge of growth and characterisation of electronic materials, especially thin films
- Fluent working knowledge of English, French and German.

Education

2010–2014 (Expected)	**Doctor of Philosophy**, *École Polytechnique Fédérale de Lausanne*, Lausanne. Ph.D. in Materials Science. Direct enrollment after Bachelors on basis of previous academic qualifications
2006–2010	**Bachelor of Technology**, *Indian Institute of Technology-Madras*, Chennai, *8.58/10*. B.Tech in Metallurgical and Materials engineering

Projects

2010-2014 **Thesis Project**, *École Polytechnique Fédérale de Lausanne*.

In Search of Ferroelectricity in Antiferroelectric Lead Zirconate

- Anomalous local ferroelectric behaviour in heteroepitaxial thin films of antiferroelectric $PbZrO_3$ observed and controlled
- Such localised ferroelectricity reduces the size of elementary bit size, potentially leading to a multifold increase in memory storage.
- Author and co-author of 2 accepted and 2 ongoing articles

2009-2010 **R&D Project Assistant**, *Indian Institute of Technology-Madras*.

Oxide Dispersion Strengthening of Ferritic steels for high temperature applications

- Nanocrystalline alloys strengthened using $Ti-Y_2O_3$ prepared through mechanical alloying, aimed at application in high temperature boilers.
- Compacted nanocrystalline alloys seen to have higher compressive strength than previously used alloys.

Work Experience

May 2009 –July 2009 **Consultant**, *John F Welch Technology Center,***General Electrics**, Bengaluru.
Evaluation of corrosion resistance of dovetail coatings

- Development of new experimental techniques with limited infrastructural backing for analysing efficiency of anodic coatings for turbine blades.
- Best coating material tested predicted to provide doubled lifetime for turbine blades in corrosive environments

May 2008 –July 2008 **Intern**, *Helmholtz Zentrum Berlin für Materialien und Energie*, Berlin.
Preparation and characterization of support grids for study of catalyst particles using Electron Tomography

- Contribution towards innovation of tomographic technique for observation of catalyst particles
- Development of new preparation process for support grids with restricted experimental facility and with time constraints
- Newly developed supports grids twice as strong and transparent as those previously used, allowing for easier observation.

Positions of Responsibility

2008-2009 **R&D Project Coordinator**, *Indian Institute of Technology-Madras*, (In collaboration with Nanyang Technological University, Singapore and National University of Singapore).

Efficient technique for eco-friendly disposal of electronic waste

- Innovation of novel technique for disposal of electronic waste with minimal pollution as part of **Mondialogo Engineering Award**
- Model entered into the finals of the competition

Technical Skills

Relevant Experimental Skills

- Pulsed Laser Deposition
- X-Ray Diffraction
- Electron Microscopy
- Nanofabrication using Focussed Ion Beam
- Scanning Probe Microscopy

Computer skills

Computational	Mathematica, COMSOL, Matlab
Text Editing	LaTeX, Microsoft Office
Image Editing	Adobe Illustrator

Publications

RG Burkovsky, AK Tagantsev, K Vaideeswaran, N Setter, et al. Lattice dynamics and antiferroelectricity in $PbZrO_3$. *Physical Review B*, 90, 2014.

AK Tagantsev, K Vaideeswaran, SB Vakhrushev, AV Filimonov, et al. The origin of antiferroelectricity in $PbZrO_3$. *Nature communications*, 4, 2013.

Languages

English	**Fluent (Level C2)**
French	**Fluent (Level C1)**
German	**Advanced (Level B2)**
Spanish	**Intermediate (Level B1, Fluent in oral communication)**
Tamil	**Fluent (Mother Tongue)**

Interests

Music	7 years vocal training in classical Indian music, and 2 years in western non-classical music with the 'Ensemble Vocal du Conservatoire de Lausanne'
Sport	Running
Other	Photography